LUNAR GEOLOGY SURVEY WITH REMOTE SENSING AND APOLLO SAMPLES

A DISSERTATION SUBMITTED TO THE GRADUATE DIVISION OF THE UNIVERSITY OF HAWAIʻI IN PARTIAL FULFILLMENT OF THE REQUIREMENTS FOR THE DEGREE OF

DOCTOR OF PHILOSOPHY

IN

Earth & Planetary Sciences

July 2020

By
Lingzhi Sun

Dissertation Committee:

Paul G. Lucey, Chairperson
Robert Wright
Hope Ishii
Sarah Fagents
Peter Gorham

To endless curiosity and fearless exploring spirit of human being.

Acknowledgements

I earned my Maters of science degree in the fall of 2016, and the diploma says my major is "Theoretical Physics". My real major was lunar remote sensing. I started my lunar science exploration since undergrad with Dr. Zongcheng Ling, and it has been a wonderful journey. After my masters, I planned to pursue a Ph.D degree. I listed several professors that I wanted to work with, and of course, Paul Lucey was on the top of my list. I still remember that three years ago, Paul emailed me and said: Why not come to work with me? I was thrilled with joy, and it felt like the wildest dream came true.

I want to thank my advisor, Dr. Paul Lucey, the best advisor in the world, for never hesitating in sharing his brilliant scientific ideas and knowledge with us students; for teaching me skills on communicating with scientists and giving scientific talks; for warmly involving me as a family member on every Thanksgiving and Christmas. I've always wanted to make planetary science my lifetime career, and when I become a professor someday, I wish that I can be someone like Paul!

I also want to thank Dr. G. Jeff Taylor, for teaching the excellent course on lunar and martian petrology, and his astonishing knowledge about lunar samples. The best thing is that Jeff and Paul share the same office area, and they both carry this marvelous sense of humor and are ready to make you laugh.

I wish to thank my dissertation committee members Paul Lucey, Robert Wright, Hope Ishii, Sarah Fagents and Peter Gorham for the support and comments.

Many thanks also to my comprehensive exam committee members, Paul Lucey, Robert Wright, G. Jeff Taylor, Jeff Gillis-Davis and Bridget Smith-Konter.

I want to thank my course instructors Patty Fryer, Paul Lucey, Jeff Taylor, Paul Wessel, Jasper Konter, Michael Garcia and James Foster.

I would like to thank Eric Pilger and Ethan Kastner for providing technical support, and Vi Nakahara, Lily Shao, Grace Furuya, Sharon Ellazar, Rena Lefevre, Karynne Morgan and Susan Van Gorder for all the help and administrative work.

Many thanks to Dr. David Blewett for recommending me to UH and giving me helpful advice about living in Hawaii.

Many thanks to my office mates and friends Elizabeth Shields, Caroline Caplan, Estelle Bonny, Melissa Adams, Macey Sandford, Hannah Moss-Davies, Emily Costello, the famous "twins" Chiara Ferrari-Wong and Abigail Flom, Collin Ferguson, Erin Fitch, Shuai Li, Andrea Gabrieli and David Frank. It is so fun to work and hang out with you lovely people!

Thanks to all the HIGP and Earth Sciences department fellows for creating such a wonderful working environment.

Last but not least, thanks to my family for always being there for me and supporting me no matter what.

Abstract

In this dissertation, I analyze the mineralogy of lunar soil and core samples with spectroscopy. Using these sample data as ground truth, I study the global mineral abundances and Mg# (molar Mg/(Mg+Fe)) distribution through radiative transfer modeling and remotely sensed images.

In Chapter 2, I study the major compositional classes of Apollo 15, 16 and 17 samples from the glass-free mineral modes derived by X-ray diffraction (XRD). Using sample data as ground truth, I mapped the global compositional class distributions, and our results suggest that both the lunar highlands and South Pole-Aitken (SPA) basin are enriched with noritic materials. I propose a"two mantles" hypothesis: The noritic composition in highland and SPA basin revealed an low-Ca pyroxene (LCP) rich upper mantle (low in Mg#) that existed before the mantle overturn; while the olivine-rich basin rings trapped the post-overturn upper mantle (high in Mg#).

In Chapter 3, I present a model that can unmix mineral abundance and chemistry based on radiative transfer theory. A new set of optical constants for olivine, orthopyroxene and clinopyroxene is reported. I build a spectral library containing mineral mixtures of plagioclase, olivine, low-Ca pyroxene and high-Ca pyroxene and Mg# ranging within 40-90. The accuracy of our model is <3 vol% for olivine, low-Ca pyroxene and high-Ca pyroxene, <6 vol% for plagioclase, and <10 for Mg#. A global Mg# map is produced using our model and the Moon Mineralogy Mapper data, and the Mg# value is consistent with results from Lunar Prospector gamma-ray spectrometer.

In Chapter 4, I present the preliminary results of the multiband images and hyperspectral measurements for the first dissection of core 73002. Both multiband images and hyperspectral data show systematic darkening and reddening from bottom to top of the core, indicating an increasing maturity from subsurface to surface soils. FeO and TiO_2 abundances suggest the soils within the core have homogeneous compositions, suggesting little contamination from lateral mixing. An optical maturity profile along the core suggests the local vertical regolith reworking depth is about 14 cm, corresponding to a time range around 61 million years. During this time, maturity of surface soils changed from immature to submature.

Table of Contents

List of Tables

List of Figures

List of Abbreviations

ANGSA	Apollo Next Generation Sample Analysis
ASD	Analytical Spectral Devices
CAAAS	Consortium for the Advanced Analysis of Apollo Samples
CBOE	Coherent backscatter opposition effect
CPX	Clinopyroxene
FHT	Feldspathic Highlands Terrane
FMR	Ferromagnetic resonance
FOV	Field of view
FWHM	Full width at half maximum
GRS	Gamma-ray spectrometer
HCP	High-Ca pyroxene
KREEP	Potassium, rare earth elements and phosphorus
LCP	Low-Ca pyroxene
LKFM	Low Potassium Fra Mauro
LM	Lunar Module
LP	Lunar Prospector

LRO	Lunar Reconnaissance Orbiter
LROC	Lunar Reconnaissance Orbiter Camera
LRV	Lunar Roving Vehicle
LSCC	Lunar Soil Characterization Consortium
M^3	Moon Mineralogy Mapper
MGM	Modified Gaussian Model
MI	Multi-band Imager
NAC	Narrow Angle camera
OMAT	Optical Maturity
OPX	Orthopyroxene
PKT	Procellarum KREEP Terrane
SHOE	Shadow hiding opposition effect
SP	Spectral Profiler on board Kaguya
SPA	South Pole-Aitken
SPAT	South Pole-Aitken Terrane
SSA	Single Scattering Albedo
USGS	U.S. Geological Survey
UVVIS	Ultra violet and visible bands
VLT	Very low titanium
XRD	X-ray Diffraction

List of Nomenclature

α	Absorption coefficient
$\langle D \rangle$	Thickness of the equivalent slab
ω	Single scattering albedo
ϕ	Filling factor
Θ	Absorption of light when it transmits within grains
S_e	Integral of external Fresnel reflection coefficients
S_i	Integral of internal Fresnel reflection coefficients
$B(g)$	Function of shadow hiding opposition effect
D	Grain size
D_R	Regolith reworking depth
e	Emission angle
En	Molar Mg*100/(Ca+Fe+Mg) for pyroxene
Fa	Molar Fe*100/(Mg+Fe) for olivine
Fo	Molar Mg*100/(Mg+Fe) for olivine
Fs	Molar Fe*100/(Ca+Fe+Mg) for pyroxene
g	Phase angle

$G.a.$	One billion years
h_s	Angular half width at half maximum SHOE
i	Incidence angle
K	Porosity coefficient
k	Imaginary index of optical constants
$M.a.$	One million years
$Mg\#$	Molar Mg*100/(Mg+Fe)
n	Real index of optical constants
$P(g)$	Single particle angular scattering function
R	Correlation coefficient
r	Reflectance
R^2	Coefficient of determination
$vol\%$	Volume percent
Wo	Molar Ca*100/(Ca+Fe+Mg) for pyroxene
$wt.\%$	Weight percent

Chapter 1

Introduction

1.1 Why the Moon?

The Earth-Moon system is suggested to have originated from a giant impact (Cameron and Canup, 1998): About 4.5 billion years ago, the proto-Earth collided with a Mars-sized planet, and the Moon was formed from the ejecta.

The Moon is the only natural satellite of the Earth. Unlike the Earth, the Moon is airless, thus major geological events can be recorded and preserved. The age of the oldest lunar rock is around 4.5 Ga (Nyquist et al., 2010), which is similar to the age of Earth. Thus the Moon can be regarded as a natural geologic laboratory for exploring the origin and evolution of the Earth-Moon system.

1.2 Evolution of the Moon: The magma ocean hypothesis

After the return of Apollo 11 samples, anorthosite was suggested to constitute lunar crust, and the magma ocean model was proposed to explain the formation of this anorthositic crust (Wood et al., 1970; Warren, 1985). Based on the magma ocean hypothesis, the Moon was once a global molten magma ocean, and olivine crystallized first, followed by orthopyroxene and clinopyroxene, and they sank to form the mantle; plagioclase started to crystallize near 80% solidification of the magma ocean, and due to its low density compared

to the residual liquids, plagioclase floated on the surface and accumulated to form the crust. At the final stage of magma ocean solidification, a layer composed of incompatible elements (KREEP) and ilmenite was left between the crust and mantle. This layer is enriched in iron and titanium and is heavier than the underlying Mg-rich olivine and pyroxene, thus the system was gravitationally unstable and might have resulted in mantle overturn (Snyder et al., 1991). During the mantle overturn, KREEP and ilmenite sank downwards, and olivine and pyroxenes rise upwards to upper mantle.

The chemistry of residual liquid changed during the fractional crystallization of the magma ocean. Mg atoms preferentially enter olivine and pyroxene over Fe atoms. Thus, Mg was consumed first, causing Mg# (molar Mg*100/(Mg+Fe)) of the residual liquids to decrease. Mg# of early crystallized olivine may have been as high as 90, and it decreased to near 40 at the late stage of magma ocean solidification (Snyder et al., 1991; Elkins-Tanton et al., 2011). Before mantle overturn, the Mg# increased with depth in the mantle; after the overturn, Mg# decreased with depth, because Mg-rich olivine and orthopyroxene were brought to the upper mantle and iron rich materials sank to the deep mantle (Elkins-Tanton et al., 2011).

1.3 Major lunar minerals and spectral properties

The Apollo 11, 12, 14, 15, 16 and 17 missions returned 382 kg lunar samples from known sampling sites, which allow us to relate sample mineralogy information to local geologic settings.

Major lunar minerals include plagioclase, olivine, low-Ca pyroxene and high-Ca pyroxene, and they usually present in the form of rocks. Stöffler et al. (1980) classified lunar plutonic highland rocks with a ternary diagram (Figure 1.1). In the second chapter, I will use this diagram to classify the compositional classes for lunar soils and map lunar surface compositional classes. This enables us to compare the mineralogy around the Moon and investigate the representativity of the Apollo samples on lunar surface.

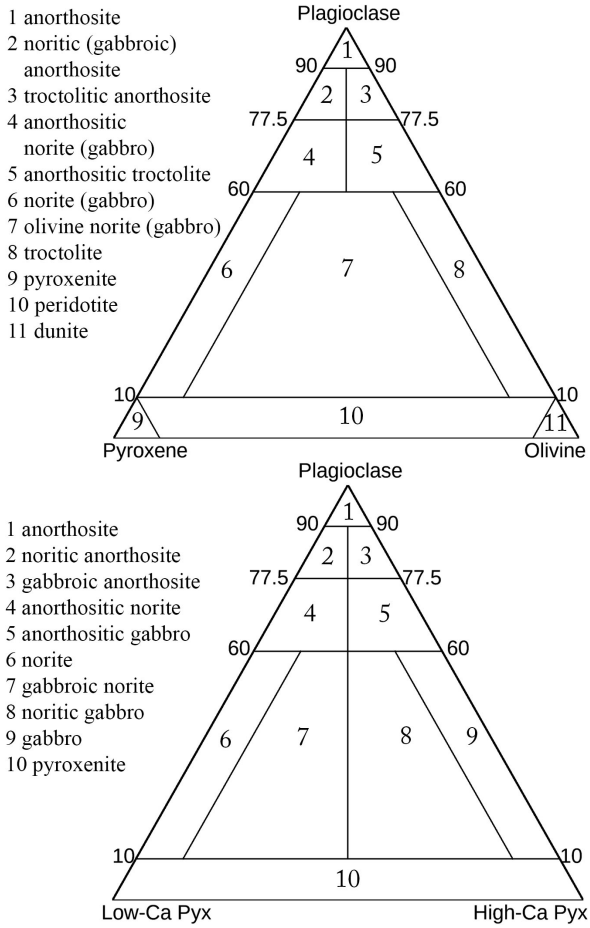

Figure 1.1: Compositional classification diagram of Stöffler et al. (1980) for lunar plutonic highlands sample.

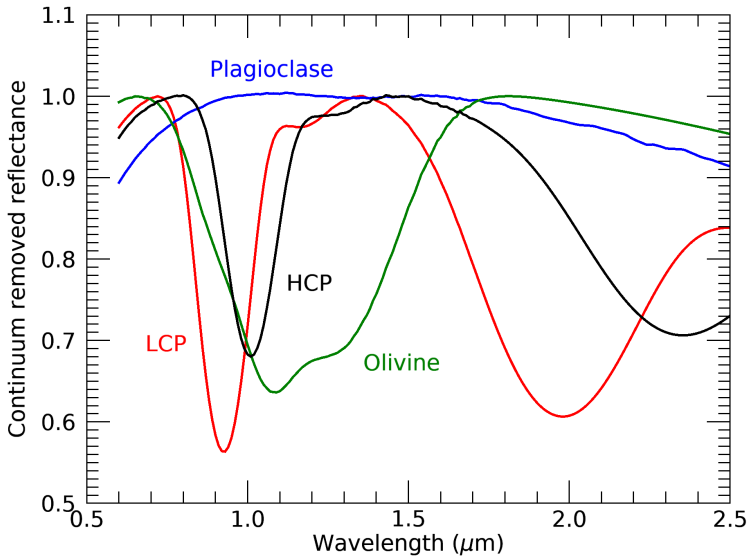

Figure 1.2: Near infrared spectra of plagioclase, olivine, low-Ca pyroxene (LCP) and high-Ca pyroxene (HCP).

I present the near infrared spectra of olivine, low-Ca pyroxene, high-Ca pyroxene and plagioclase in Figure 1.2. Pyroxenes usually have two diagnostic absorptions at 1 and 2 microns and olivine has three overlapping diagnostic absorptions centered near 900 nm, 1050 nm and 1200 nm in the one micron region. These absorption features vary with mineral chemistry. The three olivine absorption centers shift toward longer wavelengths with decreasing forsterite number (Fo, molar $Mg \times 100/(Mg+Fe)$) (Sunshine and Pieters, 1998). Pyroxene absorption centers shift toward longer wavelengths with increasing wollastonite number (Wo, molar $Ca \times 100/(Ca+Fe+Mg)$) and decreasing enstatite number (En, molar $Mg \times 100/(Ca+Fe+Mg)$)(Klima et al., 2011). Plagioclase has one weak characteristic absorption centered at 1250 nm, and this feature is easy to be flattened by space weathering.

1.4 Lunar surface compositional analysis

Taylor et al. (2019) analyzed the mineral abundances for over one hundred lunar soil samples using X-ray diffraction (XRD), and their results are consistent with those measured

by Taylor et al. (1996) and Taylor et al. (2001). Using the mineral modal abundances of lunar sample data as ground truth, I can develop global mineral maps through remote sensing, and map the distribution of major compositional classes on the Moon. In Chapter 2, I extract the spectral data of forty Apollo sampling stations using Kaguya Multiband Imager (MI) data, and derive the abundances of plagioclase, olivine, low-Ca pyroxene and high-Ca pyroxene using the radiative transfer model from Lemelin et al. (2015). To validate the radiative transfer model, abundances of these minerals are compared to those measured by XRD of lunar soils. I present the major compositional classes for Apollo 15, 16 and 17 soils. This in situ study is extended to the regional and global Moon by mapping regions that have similar mineralogically defined compositional classes to the landing sites, and track the possible origin of landing site regolith. I also present global maps of major compositional class distributions on the Moon.

In Chapter 3, I present updated optical constants for olivine with Fo ranging from 0.1 to 97, orthopyroxene with En ranging from 0 to 97.5, and clinopyroxene with Wo ranging from 8 to 46 and En ranging from 0 to 52. Based on the new optical constants, I develop a radiative transfer model that can calculate mineral content and chemistry. Forward modeling is applied with powdered pure minerals and Lunar Sample Characterization Consortium (LSCC) lunar soils to test the ability of deriving reflectance spectra from known mineral mode and Mg#. I also apply inverse modeling to derive a spectral mixing library with both varying mineral abundances and Mg#. To test the accuracy in estimating mineral contents and Mg#, I add noise comparable to the Kaguya Multiband Imager (MI) data into our spectral library and report the errors caused by noise. The mineral mode and Mg# of LSCC lunar soils were modeled and compared to those measured by X-ray digital imaging. A global Mg# map was produced using our model and Moon Mineralogy Mapper images, and this Mg# map was compared with that developed by Lunar Prospector gamma-ray data.

Chapter 4 introduces the preliminary results of our spectral measurements of a recently opened lunar core sample. The double drive tube 73001/2 was sampled at Station 3 during

the extravehicular activity (EVA) 2 of Apollo 17 mission, located near the rim of Lara crater, on the light mantle southwest of Taurus-Littrow valley (Butler, 1973). In December 2019, the Apollo Next Generation Sample Analysis (ANGSA) team opened core 73002 to examine the first of the two pristine core samples. As part of the preliminary examination, spectral imaging and hyperspectral scans of the cores are being carried out by the University of Hawai‘i, supported by the CAAAS (Consortium for the Advanced Analysis of Apollo Samples) team of ANGSA and the curatorial facility. In this chapter, I present some preliminary results of multiband imaging and hyperspectral profiles obtained during the first dissection of core 73002. I also apply the radiative transfer model introduced in chapter 3 to the hyperspectral data and calculate the mineral mode and Mg# for core 73002.

Chapter 2

Compositional class mapping of Apollo landing sites and the global Moon

2.1 Introduction

It has been 51 years since the first Apollo lunar sample was returned, and most of the available Apollo rock and soil samples have been intensively studied (Heiken et al., 1991; Papike et al., 1998). Our understanding of the landing sites has been improved through time, especially since the "J" missions (Apollo 15, 16 and 17) returned samples from areas with more complex geological settings (Spudis and Pieters, 1991). Based on these sample studies, remote sensing data has broadly extended the sample studies to a global scale (Lucey et al., 1995; Blewett et al., 1997; Lucey et al., 2000a; Lucey, 2004).

The Apollo 15 lunar module landed at the Hadley-Apennine area, located among Hadley Rille, Apennine Front and Mount Hadley (Figure 2.1, 2.2) (Apollo Lunar Geology Investigation Team, 1972; Spudis and Ryder, 1985). Rocks returned by this mission contain both mare basalts and highland materials, and the mare basalts fall into two chemical groups with similar ages ($\sim$3.3 Ga): olivine normative and quartz normative (Spudis and Ryder, 1985). KREEP basalts were found in the Apollo 15 regolith samples and were suggested to be ejecta of Aristillus and Autolycus (Apollo Lunar Geology Investigation Team, 1972). Highland samples were mainly collected at the Apennine Front, and most are impact melt and fragmental breccias. The breccias contain clasts of pristine highland rocks, including

ferroan anorthosites, norites, and troctolites, and these breccias are more mafic than those collected from the Apollo 16 site (Spudis and Ryder, 1985). The famous "black-and-white" rocks 15445 and 15455 collected from Apennine Front, with an age of 3.9 Ga and having a magnesian low-K Fra Mauro (LKFM) composition, are suggested to originate from Imbrium impact melts (Ryder and Bower, 1977; Ryder and Wood, 1977). Primary lunar crustal rocks are represented by "Genesis Rock" 15415 that is composed of 99% plagioclase, plus small amount of pyroxene and silica (Steele and Smith, 1971; Wilshire et al., 1972).

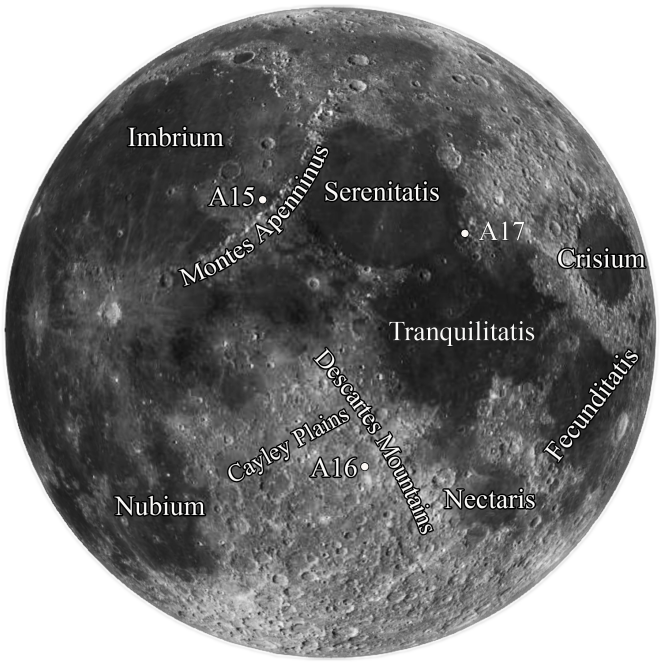

Figure 2.1: Apollo 15, 16 and 17 landing sites shown on global lunar map (LROC WAC).

Apollo 16 visited the near-side highlands at the edge of Cayley Plains and Descartes Mountains, and landed between two Copernican craters: South Ray and North Ray (Figure 2.1, 2.2). Even though located in the near-side highlands region, the Apollo 16 landing area is surrounded by several multi-ring impact basins: Imbrium, Serenitatis and Nectaris. Petro and Pieters (2006) modeled the basin ejecta mixing of magaregolith at the Apollo 16 landing site, and they suggest that Imbrium, Serenitatis and Nectaris basins each contributed $\sim$ 10% to the regolith. Hodges et al. (1973) suggested that the top layer of the Cayley Plains

deposit might have originated from Orientale basin, and the Descartes Mountains might also be overlaid with blankets generated by basin forming events.

Apollo 17 explored the Taurus-Littrow valley, which is located on the rim of Serenitatis basin. There are three feldspathic massifs surrounding this valley: South Massif, North Massif and Sculptured Hills (Figure 2.1, 2.2). South and North Massifs are suggested to be covered by the impact ejecta of Serenitatis and Crisium, while the Sculptured Hills are suggested to contain more Imbrium ejecta (Schmitt et al., 2017; Wilhelms et al., 1987). Robinson and Jolliff (2002) studied this area using Clementine FeO and TiO_2 maps, and they suggested that the massifs are composed of noritic impact melts and feldspathic materials, while the Sculptured Hills have a more mafic composition. The central valley is filled by basaltic lava flows, and mixed with pyroclastic deposits, for example, orange and black volcanic glasses (Robinson and Jolliff, 2002).The South Massif features a light mantle deposit formed as a landslide, and it is suggested to be the result of Tycho secondary impact (Lucchitta, 1977). Schmitt et al. (2017) suggested that the light mantle consists of two units, one has lower albedo, and could be caused by an avalanche earlier than the Tycho event. Jolliff et al. (1996) analyzed 789 fragments from five soil samples returned by Apollo 17, and found that their compositional classes are very diverse, including several very low titanium (VLT) mare basalts.

A recent study mapped the global distribution of lunar light plains (Meyer et al., 2018, 2020), and their results show the impact deposits of Orientale and Imbrium have extensive coverage all over the lunar surface, and that the Orientale-related impact might have erased most of those light plains related to Imbrium. Based on their map, it is possible that the landing areas of Apollo 15, 16 and 17 are covered by Orientale and/or Imbrium basin ejecta, especially the Apollo 16 area, which is located on a typical light plain: the Cayley Plains.

In this chapter, I analyze the mineral modal abundances and compositional class for forty Apollo sampling stations, with the help of mineral maps derived from Multi-band Imager (Lemelin et al., 2015) and lunar samples quantitatively analyzed through X-Ray Diffraction (XRD) (Taylor et al., 2019). This in situ study is then extended to the regional and global

Moon by mapping regions that have similar mineralogically defined compositional class to the landing sites, and the possible origin of landing site regolith. I will also present global maps of major compositional class distributions on the Moon.

2.2 Data and methods

Mineral maps derived from the SELENE Multi-band Imager (MI) (14 m spatial resolution) are used to study the petrology of Apollo 15, 16 and 17 sampling stations (Lemelin et al., 2015; Ohtake et al., 2013). The mineral modes of plagioclase, olivine, low-Ca pyroxene (LCP) and high-Ca pyroxene (HCP) were resolved in MI images with a radiative transfer model (Lemelin et al., 2015). This model first mixed olivine, LCP and HCP in 10 vol% steps, then added plagioclase to this mafic mixture in 1 vol% steps. The error of mineral modes prediction is 1 vol% for plagioclase, and 10 vol% for olivine, LCP and HCP. The mineral maps, optical maturity (OMAT) maps and FeO maps that I used in this work can be found on the USGS website: https://astrogeology.usgs.gov/search/map/Moon/Kaguya/MI/MineralMaps/Lunar_Kaguya_MIMap_MineralDeconv_OlivinePercent_50N50S.

Taylor et al. (2019) applied a quantitative analysis of the mineral abundances for 118 lunar soils with X-Ray Diffraction (XRD) and Rietveld refinement. All the XRD data can be found in the Open Data Repository (https://odr.io/lunar-regolith-xrd). The major glass-free mineral modes reported by Taylor et al. (2019) include plagioclase, olivine, augite, orthopyroxene and pigeonite. I summed pigeonite and orthopyroxene as low-Ca pyroxene, and augite is referred as high-Ca pyroxene in this work.

In order to take advantage of the XRD results, I use the XRD minerals as ground truth to the sampling stations extracted from MI mineral maps. The mineral contents of Apollo 15, 16 and 17 sampling stations were extracted from the MI mineral maps (Figure 2.2) by connecting MI images with LROC NAC traverse maps using geometric registering. For each sampling station, the mineral abundances were averaged by a 3×3 box. For XRD results, I assigned each sample to a sampling station based on the catalog of Apollo rocks

documented by the Johnson Space Center (Ryder and Norman, 1985, 1980; Ryder, 1993). When there are multiple samples collected from one single sampling station, the averaged glass-free mineral abundances (Taylor et al., 2019) of those samples were used as the mode of this station.

2.3 Results

2.3.1 Mineral modal abundances of the sampling stations from MI maps and XRD

We used forty sampling stations from Apollo 15 - 17 missions for both MI maps and XRD results, and their mineral abundances are listed in Table 2.1 and Table 2.2. We plot the mineral abundances of MI sampling stations versus those of XRD in Figure 2.3. The regression coefficient is 0.90, indicating that the mineral modes from MI maps are consistent with the XRD mineral abundances, and the relative accuracy in mineral abundances is about 10%.

We find that the MI mineral maps tend to show somewhat higher values for plagioclase, and slightly lower values for low-Ca pyroxene compared with XRD in Figure 2.3. To test if this is an artificial effect of the mineral unmixing model, we validated this model with thirty-five RELAB spectra of the same lunar soils analyzed by Taylor et al. (2019). The RELAB spectra were resampled to MI wavelengths, and their mineral modes were derived with the mineral unmixing model. The derived abundances of plagioclase, olivine, LCP and HCP from RELAB spectra versus those from XRD are plotted in Figure 2.4, with a regression coefficient at 0.92, showing a good linear correlation between XRD and radiative transfer modeling results. We did not observe overestimation of plagioclase or underestimation of LCP, suggesting the trend we observed from MI maps is not an artificial effect of the model.

A possible reason for the offset for plagioclase and LCP on MI maps could be spatial mixing. Recall that we used a 3×3 box ($\sim$ 42 m $\times$ 42 m) to cancel out possible artificial effects on MI images, but this range is much larger than the area that was actually sampled.

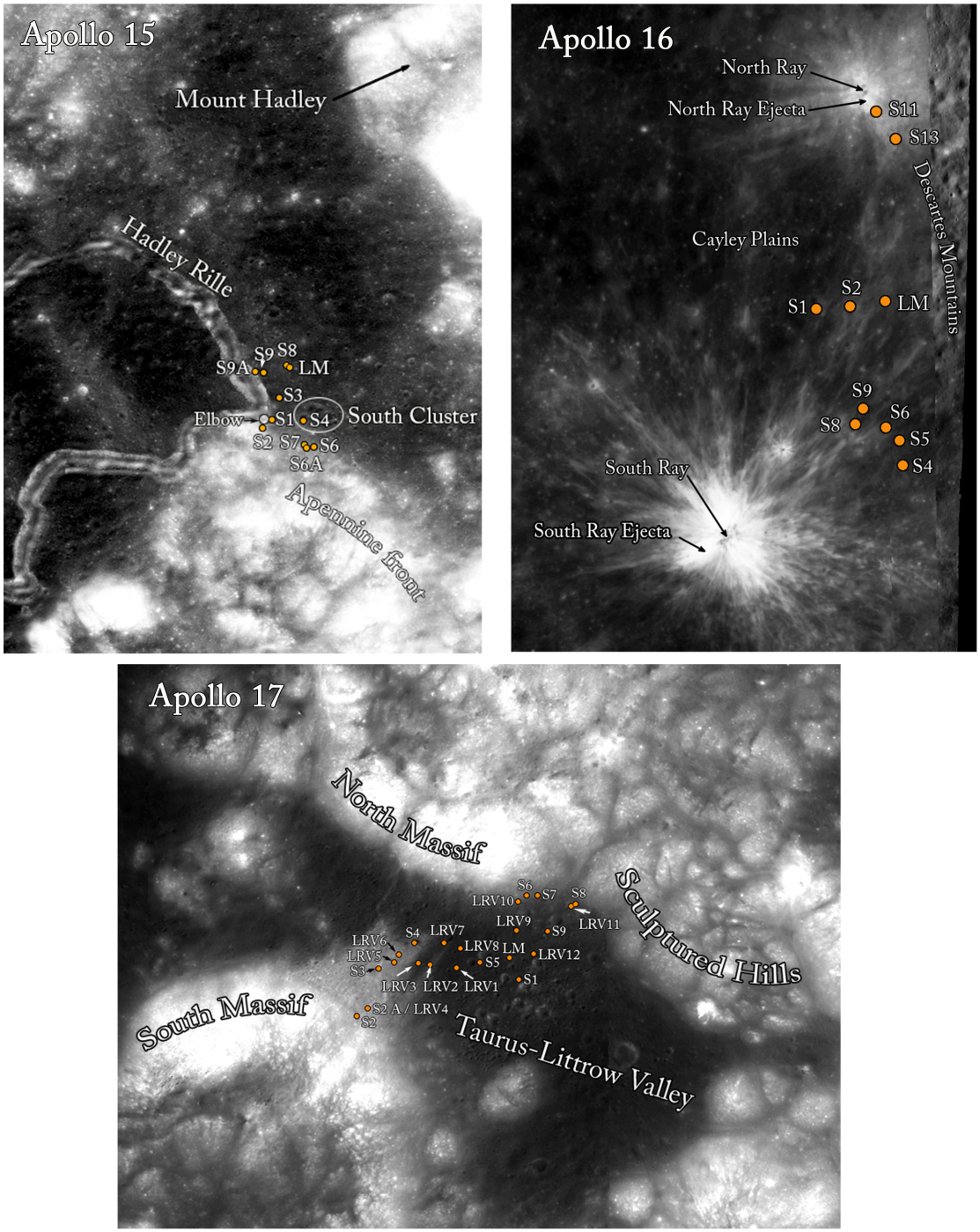

Figure 2.2: The landing area features and sampling stations of Apollo 15, 16 and 17 shown on MI images.

For example, most of the sampling stations are close to feldspathic basin rings, and it is possible that we might have included some extra feldspathic materials when collecting pixels from MI maps, thus causing a slightly higher estimation for plagioclase at landing sites.

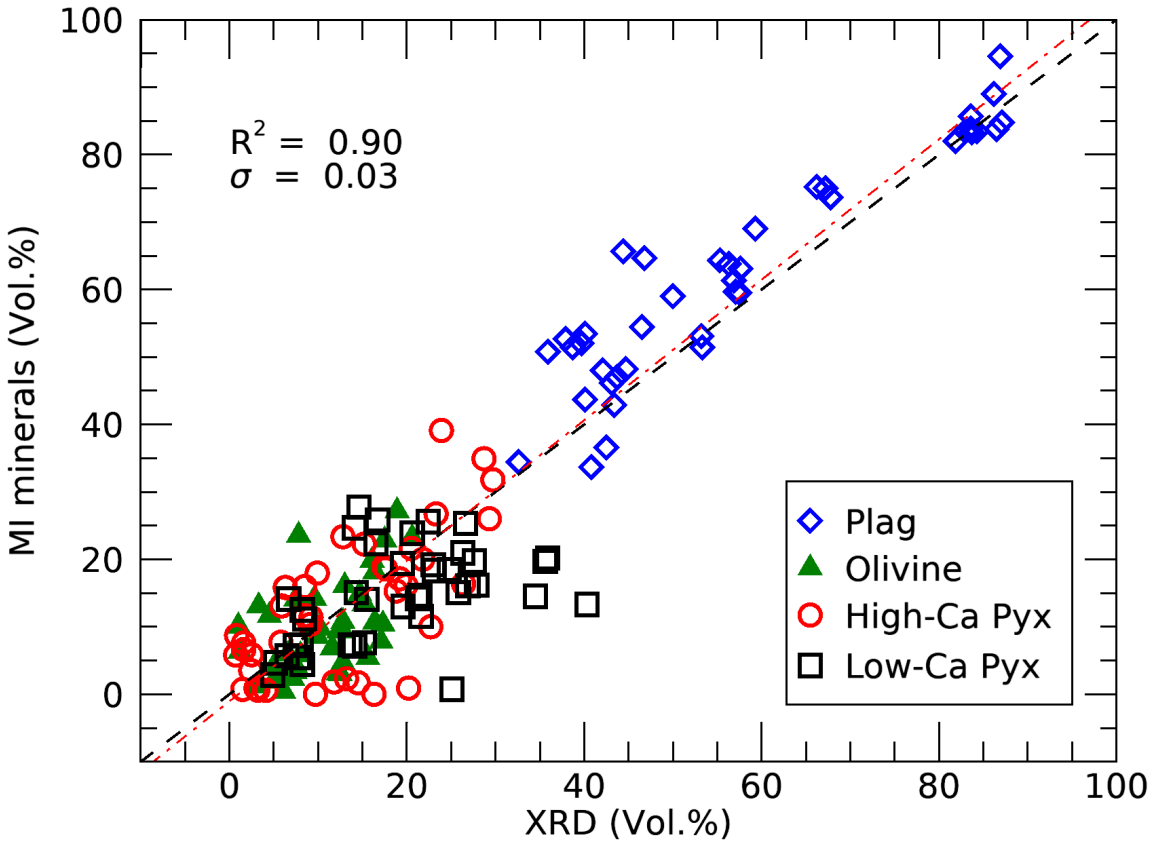

Figure 2.3: Mineral modes of forty sampling stations of Apollo 15, 16 and 17 missions from MI mineral maps vs. X-ray Diffraction analysis of lunar soil samples (glass-free mineral mode). The black dashed line is 1:1 ratio, and the red dash dot line is the regression line.

2.3.2 Compositional classes of the sampling stations

We plotted the mineral modes of Apollo 15, 16 and 17 sampling stations derived from XRD over the compositional class ternary definition diagram of Stöffler et al. (1980), and compared them to those extracted from MI mineral maps (Figure 2.5 - 2.7). Compositional class names in Stöffler et al. (1980) apply to intrusive igneous rocks, thus mare basalts or

Table 2.1: Mineral modes derived by XRD analysis of lunar soils (glass-free mode) and geologic settings for Apollo 15-17 sampling stations, mineral contents are in vol.% (Taylor et al., 2019).

Stations	Plagioclase	Olivine	High-Ca Pyx	Low-Ca Pyx	Geologic settings
A15-LM	40.1	10.2	15.2	34.5	Mare
A15-S1	39.7	4.5	19.9	35.9	Elbow
A15-S2	56.9	9.9	8.5	24.8	Apennine Front
A15-S4	38.7	12.8	20.5	27.9	Dune (South Cluster)
A15-S6	55.3	9.8	9.1	25.8	Apennine Front
A15-S6A	46.8	17.1	9.2	26.9	Apennine Front
A15-S7	57.6	12.3	8.5	21.6	Apennine Front
A15-S9	35.9	9.6	18.8	35.6	Rille
A15-S9A	32.6	3.3	23.9	40.3	Rille
A16-LM&S10	87.1	3.2	1.6	8.1	Cayley Plains
A16-S1	84.3	7.1	0.8	7.8	Cayley Plains
A16-S2	83.6	7.5	0.7	8.2	Cayley Plains
A16-S4	86.5	5.4	1.6	6.5	Descartes Mountains
A16-S5	83.6	5.0	3.0	8.5	Descartes Mountains
A16-S6	83.0	7.3	1.5	8.2	South Ray
A16-S8	81.9	7.4	4.1	6.7	South Ray
A16-S9	83.7	6.6	2.4	7.4	South Ray
A16-S11	86.9	5.0	3.2	4.9	North Ray
A16-S13	86.2	6.1	2.5	5.2	North Ray
A17-LM	42.1	11.6	23.3	23.1	Valley
A17-S1	40.8	8.0	28.7	22.4	Valley
A17-S2	66.2	12.5	5.8	15.5	South Massif
A17-S2A/LRV4	67.2	12.8	5.9	14.1	Light Mantle
A17-S3	67.8	12.3	6.3	13.6	Light Mantle
A17-S4	44.4	7.8	22.7	25.1	Light Mantle
A17-S5	43.4	1.0	29.3	26.3	Valley
A17-S6	56.3	17.3	9.7	16.7	North Massif
A17-S7	57.5	15.2	13.2	14.1	North Massif
A17-S8	53.2	12.8	12.8	21.2	Sculptured Hills
A17-S9	43.1	7.5	21.8	27.6	Valley
A17-LRV1	40.1	13.0	26.4	20.6	Valley
A17-LRV2	50.0	16.1	14.5	19.5	Valley
A17-LRV3	46.5	20.6	16.3	16.5	Valley
A17-LRV5	59.3	15.6	9.9	15.2	Light Mantle
A17-LRV7	37.9	18.9	20.2	23.0	Valley
A17-LRV8	43.7	17.5	19.2	19.6	Valley
A17-LRV9	44.7	16.4	17.4	21.5	Valley
A17-LRV10	57.1	16.4	11.8	14.6	North Massif
A17-LRV11	53.3	14.7	17.6	14.3	Sculptured Hills
A17-LRV12	42.5	1.2	29.7	26.6	Valley

Table 2.2: MI Mineral modes and geologic settings for Apollo 15-17 sampling stations, minerals contents are in vol.%.

Stations	Plagioclase	Olivine	High-Ca Pyx	Low-Ca Pyx	Geologic settings
A15-LM	53.4	9.8	22.3	14.5	Mare
A15-S1	52.0	11.7	16.1	20.2	Elbow
A15-S2	61.3	8.5	11.7	18.5	Apennine Front
A15-S4	51.4	10.8	21.6	16.2	Dune (South Cluster)
A15-S6	64.3	10.3	10.3	15.1	Apennine Front
A15-S6A	64.7	7.8	11.4	16.1	Apennine Front
A15-S7	63.1	9.3	16.0	11.6	Apennine Front
A15-S9	50.8	14.2	15.3	19.7	Rille
A15-S9A	34.4	13.1	39.1	13.3	Rille
A16-LM&S10	84.8	1.3	6.6	7.3	Cayley Plains
A16-S1	83.4	2.4	8.7	5.5	Cayley Plains
A16-S2	85.7	4.1	5.8	4.4	Cayley Plains
A16-S4	83.8	2.9	7.6	5.7	Descartes Mountains
A16-S5	83.9	4.1	0.9	11.2	Descartes Mountains
A16-S6	83.4	3.3	0.7	12.5	South Ray
A16-S8	82.0	3.3	0.6	14.1	South Ray
A16-S9	83.3	5.9	3.5	7.2	South Ray
A16-S11	94.6	2.0	0.6	2.9	North Ray
A16-S13	89.0	0.5	5.9	4.7	North Ray
A17-LM	48.0	6.9	26.7	18.4	Valley
A17-S1	33.7	5.8	34.9	25.6	Valley
A17-S2	75.2	3.0	7.7	14.1	South Massif
A17-S2A/LRV4	75.0	4.7	13.1	7.2	Light Mantle
A17-S3	73.7	3.2	15.8	7.3	Light Mantle
A17-S4	65.7	23.6	10.0	0.7	Light Mantle
A17-S5	42.9	10.1	26.0	21.0	Valley
A17-S6	63.8	10.4	0.0	25.8	North Massif
A17-S7	59.6	13.4	2.3	24.7	North Massif
A17-S8	53.1	9.3	23.4	14.2	Sculptured Hills
A17-S9	46.1	14.1	20.0	19.7	Valley
A17-LRV1	43.7	16.1	16.4	23.9	Valley
A17-LRV2	59.0	19.9	1.7	19.4	Valley
A17-LRV3	54.4	23.2	0.0	22.3	Valley
A17-LRV5	69.0	5.4	18.0	7.6	Light Mantle
A17-LRV7	52.7	27.2	0.9	19.2	Valley
A17-LRV8	47.0	22.9	17.1	13.0	Valley
A17-LRV9	48.2	18.2	18.9	14.7	Valley
A17-LRV10	59.7	10.7	1.8	27.8	North Massif
A17-LRV11	51.4	14.9	18.6	15.1	Sculptured Hills
A17-LRV12	36.6	6.3	31.8	25.3	Valley

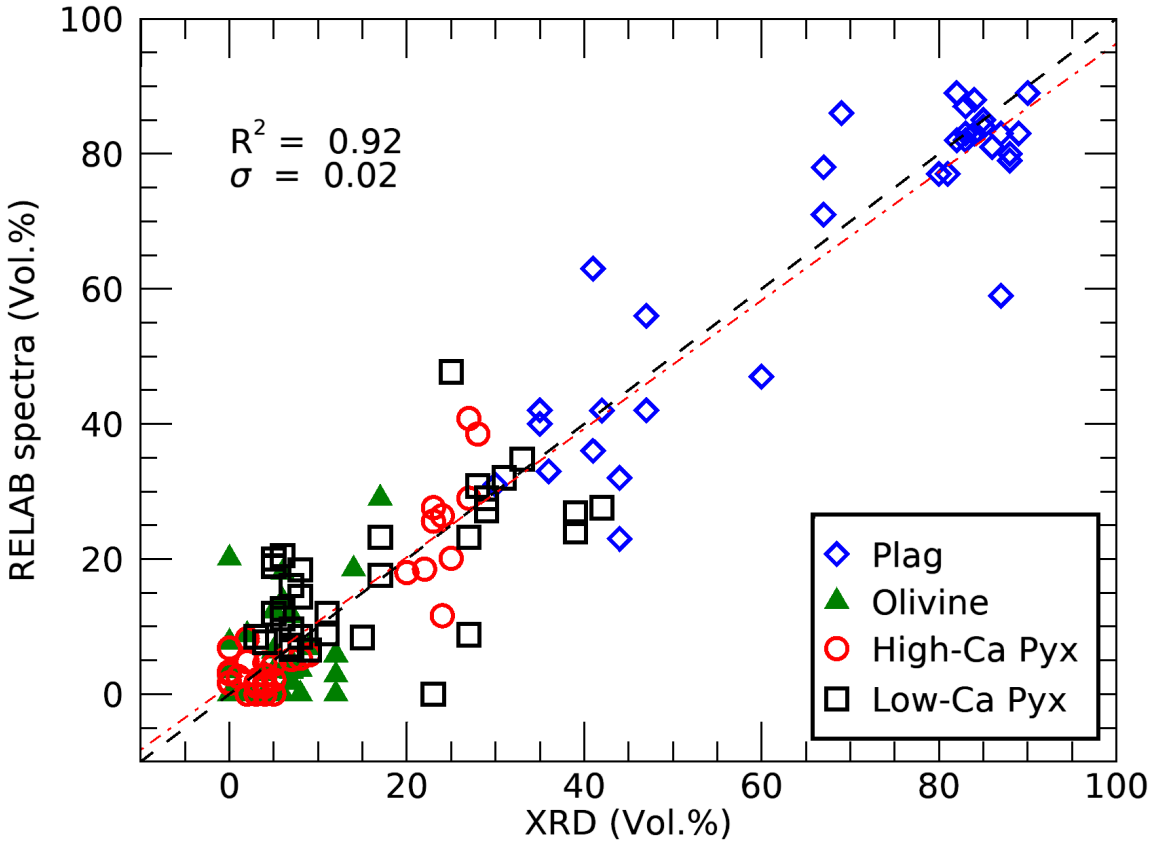

Figure 2.4: Mineral modes derived from RELAB spectra versus XRD for thirty-five lunar soils (grain size: 0 - 150 μm) (Taylor et al., 2019), the black dashed line is 1:1 ratio, and the red dash dot line is the regression line.

KREEP basalts would plot in the regions designated 6 (norite or gabbro) and 7 (olivine norite or gabbro) from Figure 2.5 - 2.7. The use of these diagrams is not to imply that the regolith, which is a mixture of rocks, is composed only of rocks in a given field. The diagrams are useful for comparing regolith compositions around the Moon. In order to show a comprehensive geological view for the Apollo landing area, we also extracted the mineral modes for nearby geological settings (immature area with OMAT > 0.25 only, Lemelin et al. (2015); Lucey et al. (2000b)) from the MI mineral maps (Figure 2.2), and over-plotted them with standard deviations on the ternary diagrams (Figure 2.5-2.7). To better show the geological background of the landing sites, we mapped the surrounding nonmare immature

areas having similar compositional class to the landing sites using mineral constraints, shown in Figure 2.8. More details are given below.

Compositional class of Apollo 15 sampling stations

XRD results (Figure 2.5) show that most of the Apollo samples are mafic mare basalts, and the only anorthositic materials were collected near the Apennine Front. Major compositional class from the XRD analysis are dominated by norite/gabbro and olivine norite/gabbro. They fall into two groups, one contains more anorthositic materials, and they were mainly from the Apennine Front; the other group were slightly more mafic, and they were mostly collected within the maria. Compositional class from MI maps (Figure 2.5) for the same landing stations show a more anorthositic and gabbroic composition, with the Apennine Front dominated by anorthositic norite/gabbro, the rest dominated by olivine norite/gabbro.

Major geological features near the sampling stations include Mount Hadley to the north of the landing area, the elevated area of the Apennine Front, the South Cluster and the Elbow crater (Figure 2.2, 2.5). Mount Hadley and Apennine Front belong to the Montes Apenninus - the outer basin ring of Imbrium, and their compositional class are dominated by anorthositic norite, with Mount Hadley being slightly more anorthositic than the Apennine Front. The South Cluster is suggested to be secondary craters generated by the impacts that have formed Aristillus or Autolycus (Spudis and Ryder, 1985), and the Apollo samples were collected from the rim of Dune crater. Both XRD and MI results show that the samples collected from Dune crater are mineralogically consistent with mare basalt. MI results show a slightly more gabbroic composition compared to XRD, while South Cluster possesses compositions in between. This result shows that South Cluster craters did not penetrate the mare deposits because they are secondary craters that did not penetrate the top mare deposit layer (Spudis and Ryder, 1985). Elbow crater and samples collected near the Hadley Rille also show a similar composition to the mare basalts. From MI mineral maps, Elbow crater has a more anorthositic composition than the XRD results, which

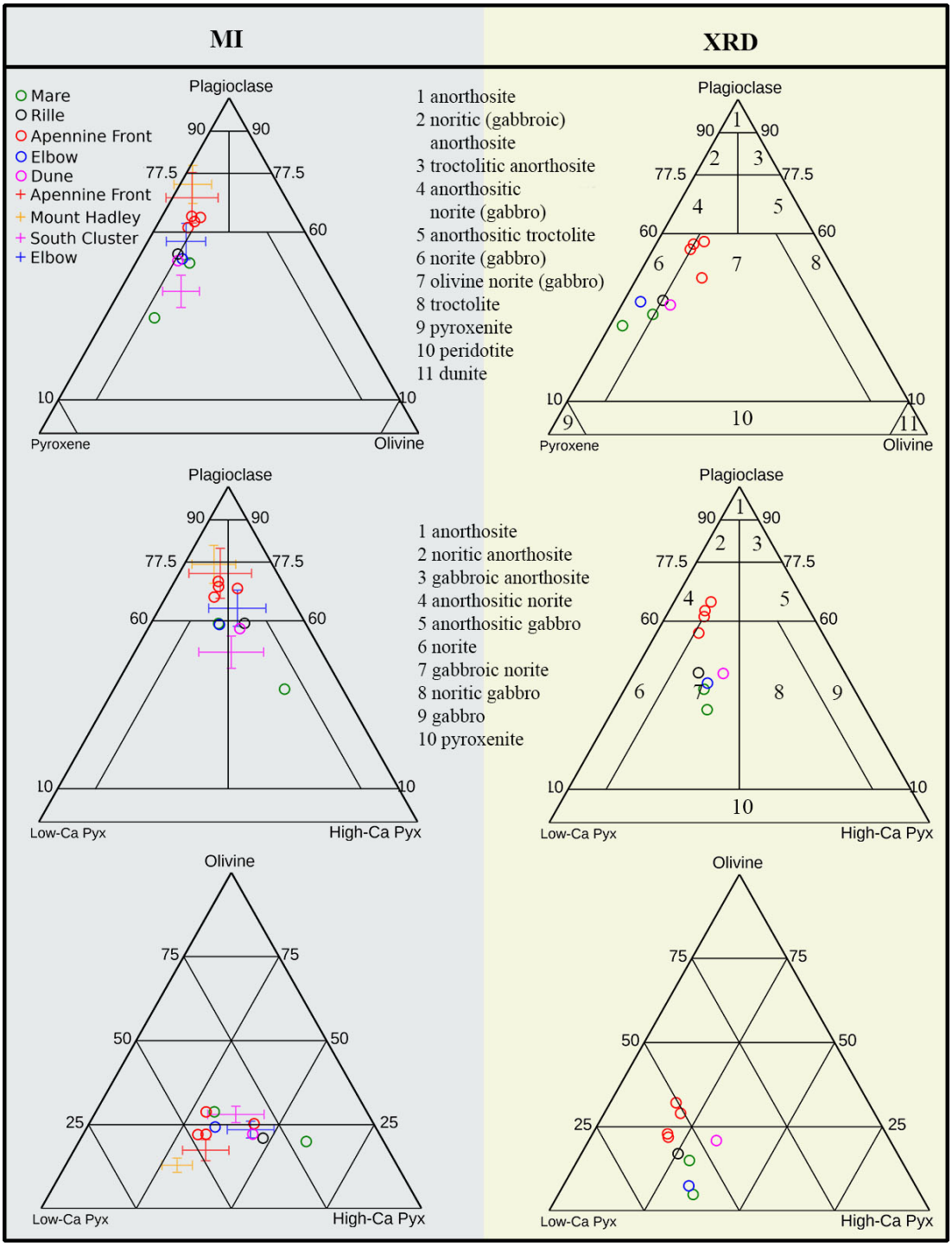

Figure 2.5: Ternary plot of minerals (vol%) for Apollo 15 sampling stations analyzed by XRD (right) and those derived from MI (left) spectral images (circles), mineral ranges from MI maps of the nearby geological features are shown by '+' symbols. Igneous compositional class identification is based on Stöffler et al. (1980).

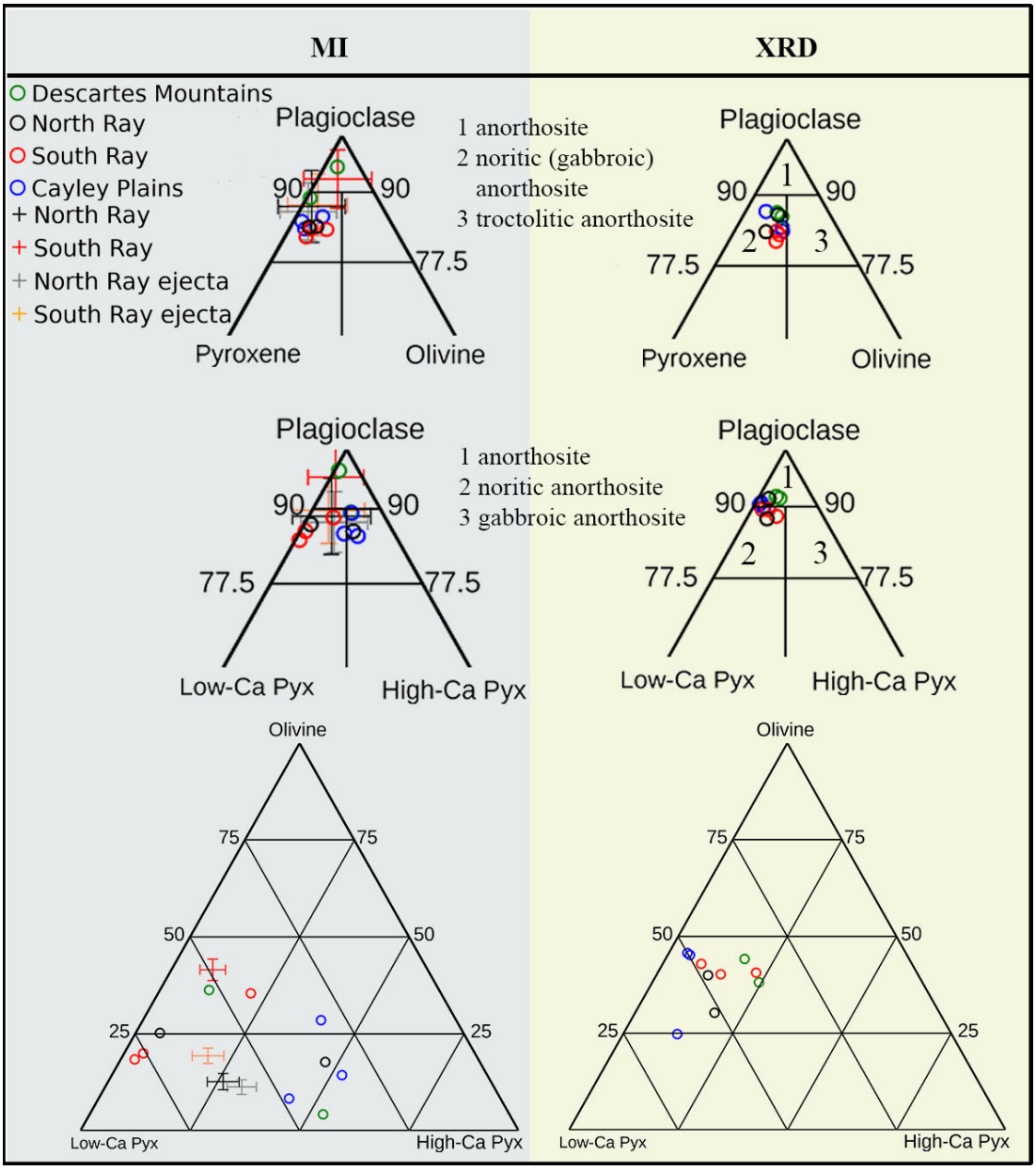

Figure 2.6: Ternary plot of minerals (vol%) for Apollo 16 sampling stations analyzed by XRD (right) and those derived from MI (left) spectral images (circles), mineral ranges from MI maps of the nearby geological features are shown by '+' symbols.

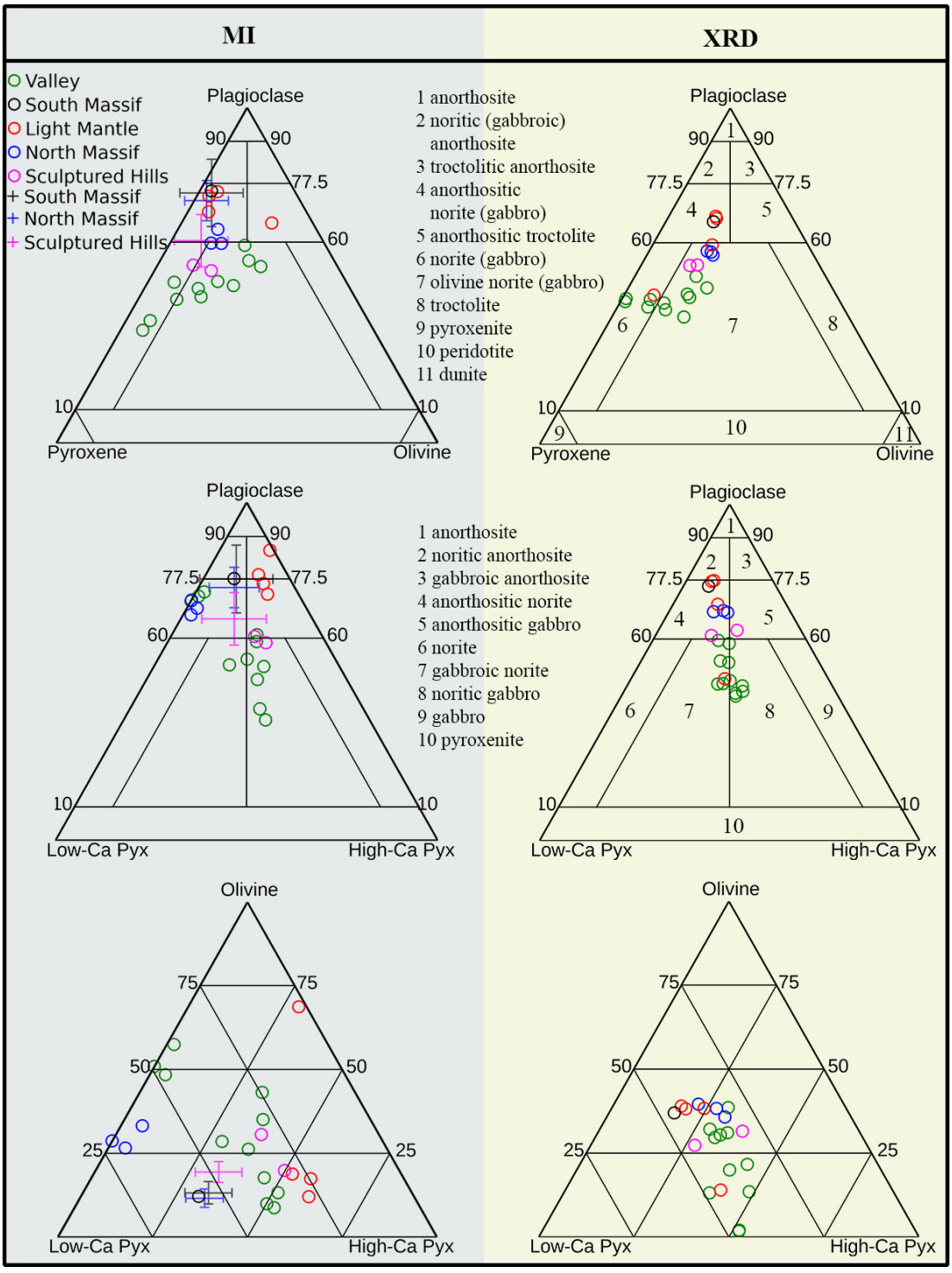

Figure 2.7: Ternary plot of minerals (vol%) for Apollo 17 sampling stations analyzed by XRD (right) and those derived from MI (left) spectral images (circles), mineral ranges from MI maps of the nearby geological features are shown by '+' symbols.

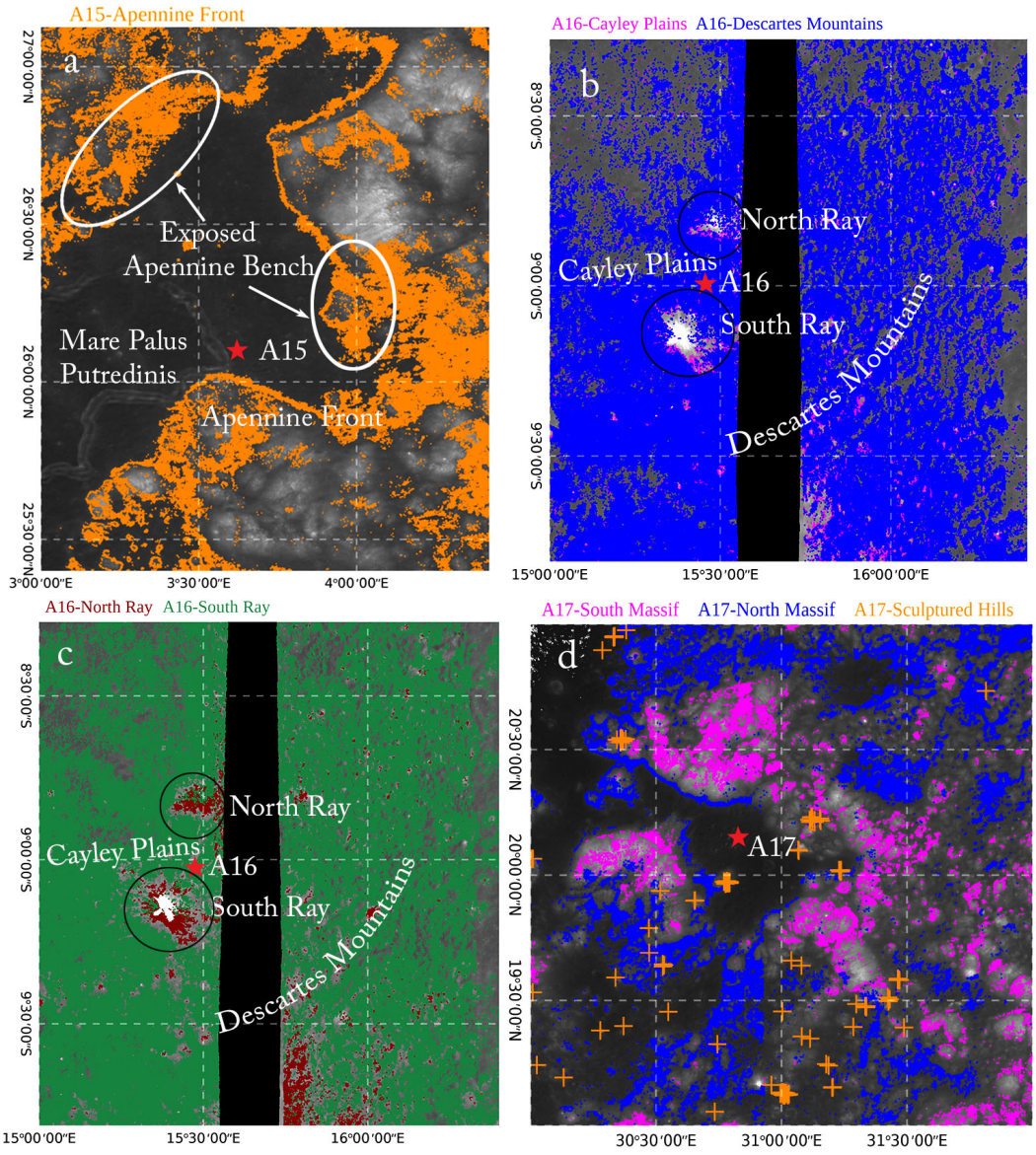

Figure 2.8: Regions having similar compositional class to (a) Apollo 15 Apennine Front (orange) samples, (b) Apollo 16 Cayley Plains (pink) and Descartes Mountains (blue) samples (most of the pink areas can not be seen because they are overlaid by blue), (c) Apollo 16 North Ray (red) and South Ray (green) samples (most of the red areas can not be seen because they are overlaid by green), and (d) Apollo 17 South Massif (pink), North Massif (blue) and Sculptured Hills (orange) samples.We were only matching nonmare areas (FeO $<$ 13 wt.%).

might be the result of including pixels from Apennine Front that are more anorthositic on MI maps.

We mapped areas that have compositional class similar to the Apennine Front samples in Figure 2.8a, and they are: rim areas that lie between Montes Apenninus and mare Palus Putredinis, where basaltic mare material and feldspathic highlands materials mix; the exposed Apennine Bench formation (Figure 2.8a), which is suggested to be composed of KREEP basalts underlying the mare lava flow near the landing sites (Taylor et al., 2012). The rims areas between mare and highlands and the Apennine bench formation have different origins, but they both contain anorthositic norites composition.

Compositional class of Apollo 16 sampling stations

The Apollo 16 module landed on the nearside highlands, at the edge of Cayley Plains and Descartes mountains, between two Copernican craters - North Ray and South Ray. Major compositional classes are shown in Figure 2.6. Both XRD and MI results suggest a highly anorthositic composition, and the major compositional classes are noritic anorthosite and anorthosite based on sample analysis. The MI map suggests the major compositional classes are anorthosites and noritic/gabbroic anorthosite. Mineralogy of sampling stations collected from MI images are consistent with XRD results, except they are slightly more gabbroic. This area has a significant coverage of ejecta from both North-Ray and South-Ray craters (Figure 2.2).

We attempted to compare the returned soils sampled around the two craters to those located inside and on the ejecta of the North Ray and South Ray. We extracted and over-plotted the compositional classes of materials from inside of and ejecta from North and South Ray craters with the sampling stations in Fig 2.6. The compositional classes of materials from crater inside and ejecta are very similar to those sampled around the craters, and South Ray crater contains the most anorthositic material.

By matching compositional classes of Apollo 16 sampling stations to a broader area (Figure 2.8b, c), we find that Cayley Plains and Descartes Mountains are similar in

composition. Cayley Plains are suggested to be ejecta deposits from Orientale and/or Imbrium (Meyer et al., 2018, 2020). It is possible that compositions of Descartes Mountains materials have been blurred by basin ejecta.

Compositional classes of Apollo 17 sampling stations

Apollo 17 explored the Taurus-Littrow valley (Figure 2.2). Both the XRD analysis of lunar soils (Figure 2.7) and MI maps suggest South Massif is dominated by anorthositic norite. Modes of soils from sampling stations on the light mantle have relatively diverse compositions; those samples collected near the base of South Massif have similar compositions to the massif, and others are more mafic due to mixing with mare basalt in the valley. The North Massif is less anorthositic than South Massif, and its major compositional class is olivine norite from sample analysis, and anorthositic norite from MI maps. Samples collected from Sculptured Hills have the same compositional class to those collected from North Massif, but from MI maps, Sculptured Hills are dominated by gabbro and olivine gabbro. Sculptured Hills has the most abundant mafic compositions among the three local highlands features.

These massifs and hills are located at the outer ring of Serenitatis basin, so it is likely that they contain information regarding the basin forming impacts. Both Moon Mineralogy Mapper (M^3) (Schmitt et al., 2017) and LROC (Spudis et al., 2011) data suggest Sculptured Hills might be ejecta from Imbrium instead of Serenitatis. Compositional classes derived from MI mineral maps suggest more anorthositic and gabbroic compositions than those from XRD, but the relative compositions are consistent with XRD results. Samples from the Valley are mainly basaltic rocks (norite/gabbro, olivine norite/gabbro in Fig 2.7).

Regional compositional class mapping results of South Massif, North Massif and Sculptured Hills are shown in Figure 2.8d. It can be seen that those relatively elevated areas are dominated by compositional classes similar to the South Massif, while areas located at the base of Massifs and Hills are mainly consist of compositional classes similar to North Massif samples. Compositional classes similar to Sculptured Hills samples have relatively

less coverage in this area. Considering that it is likely that South Massif, North Massif and Sculptured Hills are overlaid by ejecta blankets from later formed basins, those materials on the Sculptured Hills might have a different source region from the two Massifs.

2.3.3 Global distributions of similar compositional classes to the Apollo sampling sites

It was suggested previously that the lunar highlands sampled by Apollo 15, 16 and 17 might be mixtures of ejecta from several basin ejecta. After deriving compositional classes for Apollo sampling stations, we used MI mineral maps to search Moon-wide for areas having similar compositional classes to the landing stations. We focus on highland rocks, namely the Apollo 15 samples collected from Apennine Front, Apollo 16 samples collected from South Ray, North Ray, Cayley Plains and Descartes Mountains, and Apollo 17 samples collected from South Massif, North Massif, Sculptured Hills and the Light Mantle. The range of mineral abundances for each compositional class is confined as the minimum and maximum abundances of plagioclase, olivine, high-Ca pyroxene and low-Ca pyroxene for each geologic setting (see Table 2.1). We only searched areas having FeO < 13 wt.% and OMAT > 0.25 (Lemelin et al., 2015; Lucey et al., 2000b); the global matching results are mapped in Figure 2.9.

The Apennine Front consists of anorthositic norite/gabbro (Figure 2.5). Regions having similar compositional classes to Apennine Front are mainly located at the rim of Procellarum KREEP Terrain (PKT), cryptomaria in Schiller-Schickard and north South Pole-Aitken (SPA). Spudis and Ryder (1985) suggested that Apennine Front is contaminated with basaltic materials that are possibly origin from mare Palus Putredinis. This is consistent with the composition of PKT rim region, where lunar mare and highlands interact, and mixtures of basalts and feldspathic materials would be frequent there. Cryptomaria are suggested to be ancient mare deposits that are excavated by impacts (Whitten and Head, 2015), in comparison to non-cryptomare light plains, where no basaltic materials are involved. Schiller-Schickard is suggested to be a mixture of volcanic basalts and feldspathic

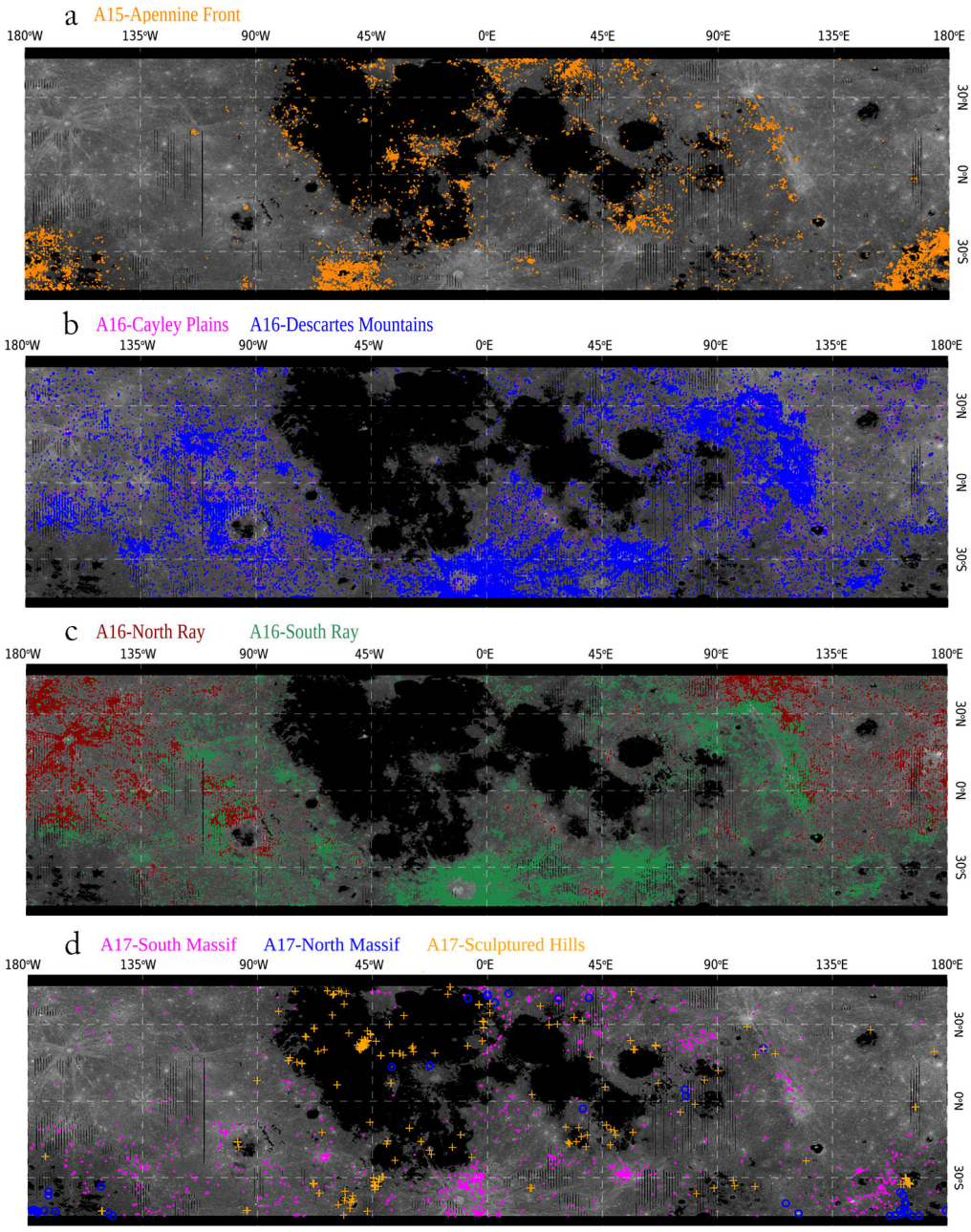

Figure 2.9: Regions having similar compositional classes to (a) Apollo 15 Apennine Front (orange) samples, (b) Apollo 16 Cayley Plains (pink) and Descartes Mountains (blue) samples (most of the pink areas can not be seen because they are overlaid by blue), (c) Apollo 16 North Ray (red) and South Ray (green) samples, and (d) Apollo 17 South Massif (Pink), North Massif (blue) and Sculptured Hills (orange) samples. We were only matching nonmare and immature areas (FeO < 13 wt.%, OMAT > 0.25).

impact ejecta from Orientale basin (Blewett et al., 1995; Whitten and Head, 2015). Our results are also consistent with mixture of feldspathic and mare materials. We also find similar compositional classes in South Pole-Aitken, and they mostly surround recognized mare and cryptomaria, indicating that extensive impact related surface reworking and material mixing have taken place.

Apollo 16 sampled the nearside highland, and its major compositional classes are anorthosite, noritic/gabbroic anorthosite. Cayley Plains and Descartes Mountains are suggested to be covered by impact ejecta and are not representative of typical lunar highlands (Hodges et al., 1973). Meyer et al. (2020) also showed a global map of light plains (including Cayley Plains). These light plains are possibly related to Imbrium and Orientale impact ejecta. From our compositional class matching result (Figure 2.9 b), it can be observed that areas having similar compositional classes to Cayley Plains and Descartes Mountains overlap substantially, suggesting that Cayley Plains and Descartes Mountains might be covered by a layer of ejecta from the same source. Orientale is the most likely source for these ejecta, since we found abundant similar compositional classes on the Hevelius Formation, the major basin ejecta deposit of Orientale. North Ray and South Ray samples (Figure 2.9 c) are more noritic compared to Cayley Plains and Descartes Mountains. Regions with compositional classes similar to North Ray are concentrated on lunar far-side highlands, while regions having similar compositional classes to South Ray are mainly concentrated on the nearside highlands, with some outcrops on the farside. This result suggests that North Ray samples are representative of lunar farside material compositions, which should be noritic anorthosite.

We plotted regions with compositional classes similar to Apollo 17 sampling stations in Figure 2.9 d, and the geologic features include the Light Mantle, South Massif, North Massif and Sculptured Hills. Light Mantle contains a mixture of South Massif landslide and central valley basalts, and matched areas are concentrated at the rim of impact basins like Imbrium, Orientale and Moscovience. There are also distributions in some cryptomaria like Schiller-Schickard and Milne (see Whitten and Head (2015) for locations). Compositional

classes similar to South Massif are mainly located on the outer rings of major impact basins, including Serenitatis, Imbrium, Procellarum, Orientale and SPA, demonstrating the pertinence of Apollo 17 samples to studying the basin ring compositions of the Moon. North Massif samples are less anorthositic than the South Massif, and the global matching results suggest concentrations of similar compositional classes around Imbrium and inside South Pole-Aitken. Sculptured Hills samples consist of the most mafic compositions among the highlands features in Taurus-Littrow Valley. Regions that have similar compositional classes to Sculptured Hills are concentrated inside impact basins like Imbrium, Crisium and Procellarum, as well as the inner ring of Orientale and Moscovience. Both North Massif and Sculptured Hills contain very few compositions similar to Serenitatis basin, which imply these two features might be blanketed in impact ejecta, possibly from Imbrium and/or Crisium.

2.3.4 Global compositional class mapping

In addition to searching for compositional classes similar to the landing sites, we also mapped all outcrops of the compositional classes for immature (OMAT > 0.25) and nonmare surface (FeO < 13 wt.%) to interpret the global petrological properties of the lunar crust. We plotted histograms of the targeted areas on a compositional class classification ternary diagram, shown in Figure 2.10 a, b. It is evident that the lunar crust is depleted in olivine, and the majority of the lunar crust is noritic, and this is consistent with the observations of Lucey et al. (2014) and Melosh et al. (2017). The percentage of the spatial coverage of each compositional class is labeled in Figure 2.10 c, and the most abundant compositional class is noritic anorthosite ($\sim$40%), followed by anorthositic norite (24.1%) and anorthosite (23%); the rest only constitute $\sim$13% of the lunar crust.

The outcrops of major compositional classes displayed in Figure 2.10 a, b are mapped in Figure 2.11. It can be seen that anorthosite and noritic anorthosite represent the range of Feldspathic Highlands Terrane (FHT) very well (Jolliff et al., 2000), indicating that a high concentration of plagioclase, and 10-20% of low-Ca pyroxene exists in the lunar crust.

Anorthositic norite is widespread overall, but we notice some concentrations around the PKT and Orientale basin, and also inside South Pole-Aitken Terrane (SPAT) (Jolliff et al., 2000). The major norite and olivine norite concentrations are in SPAT and cryptomaria like Schiller-Schickard and Hercules (Whitten and Head, 2015). Gabbroic constitute less than 9% of the targeted areas, and most of the outcrops are either related to craters or basins. Olivine-bearing classes constitute less than 2% of the targeted areas, reinforcing the conclusion that olivine is a rare mafic mineral compared to pyroxenes in lunar highlands and SPA (Lucey et al., 2014; Melosh et al., 2017).

2.4 Discussion

2.4.1 Compositional classes on the Moon

The Apollo missions only visited the near side of the Moon, and we have not yet acquired any sample known to originate from the farside. However, by searching areas that have the same compositional classes to the sampling stations, we find that the current Apollo samples represent broad areas on the Moon. For example, it can be seen from Figure 2.9 that North-Ray and South-Ray samples from Apollo 16 missions well represent the major compositional classes for both nearside and farside highlands, and samples collected from Cayely Plains and Descartes Mountains well represent impact ejecta of Orientale.

Based on the compositional class mapping results, noritic anorthosite is the most abundant compositional class all over the FHT, followed by anorthosite and anorthositic norite, indicating that FHT is very rich in plagioclase, and the dominate mafic mineral is low-Ca pyroxene. This is consistent with the small crater survey of Lucey et al. (2014).

Both our results and those of Lucey et al. (2014) show the presence of abundant low-Ca pyroxene across the crust, but where did these mafic minerals form? Based on the Lunar Magma Ocean hypothesis, the lunar crust was formed by plagioclase cumulating upwards from the magma ocean (Wood et al., 1970; Warren, 1985). Plagioclase started to crystallize when the lunar magma ocean was $\sim$ 80% solidified, while most of the mafic

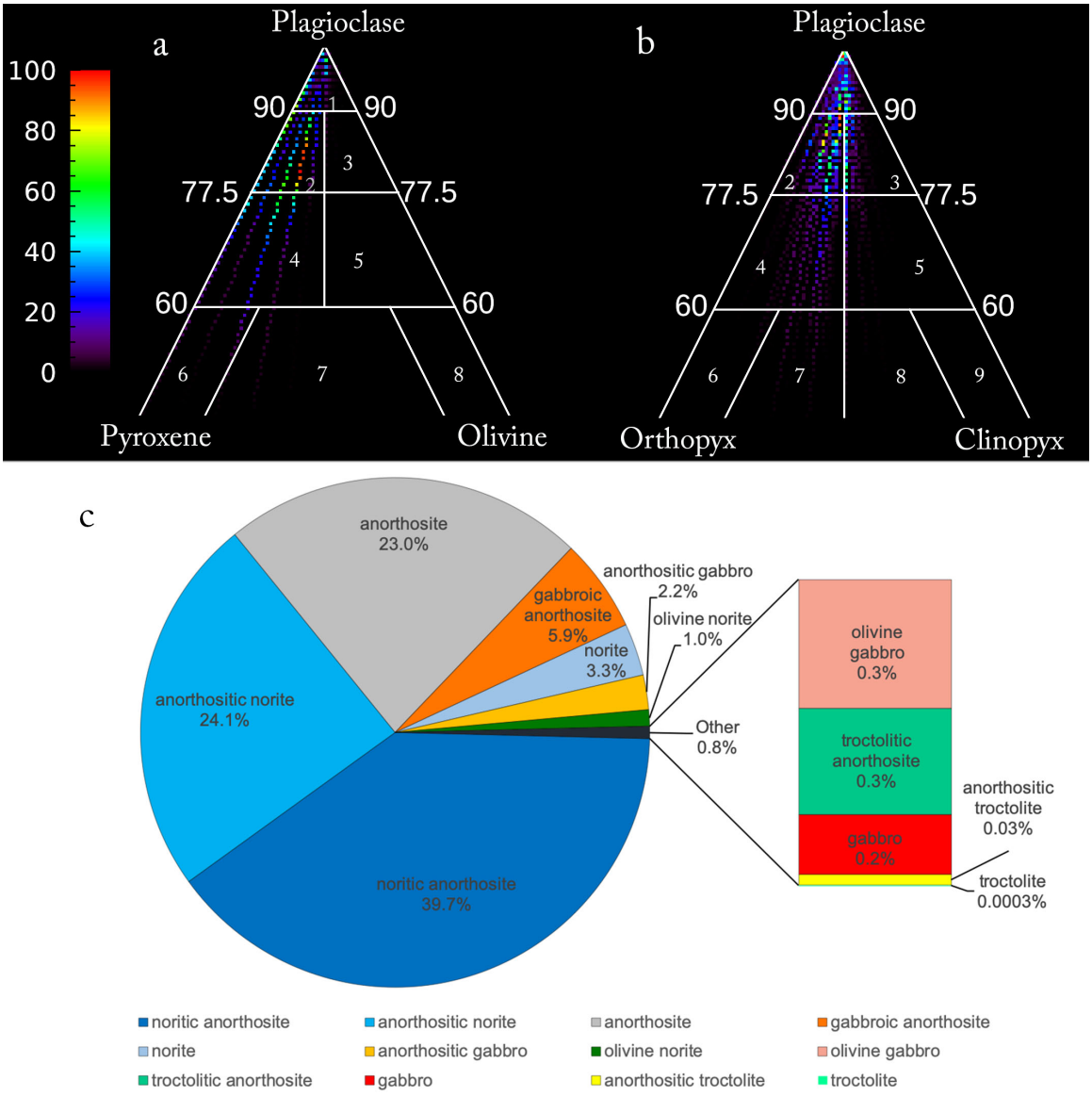

Figure 2.10: (a) and (b), compositional classification for nonmare and immature global Moon, (c) spatial coverage percentage of the lunar global distribution of compositional classes mapped in Figure 2.11 .

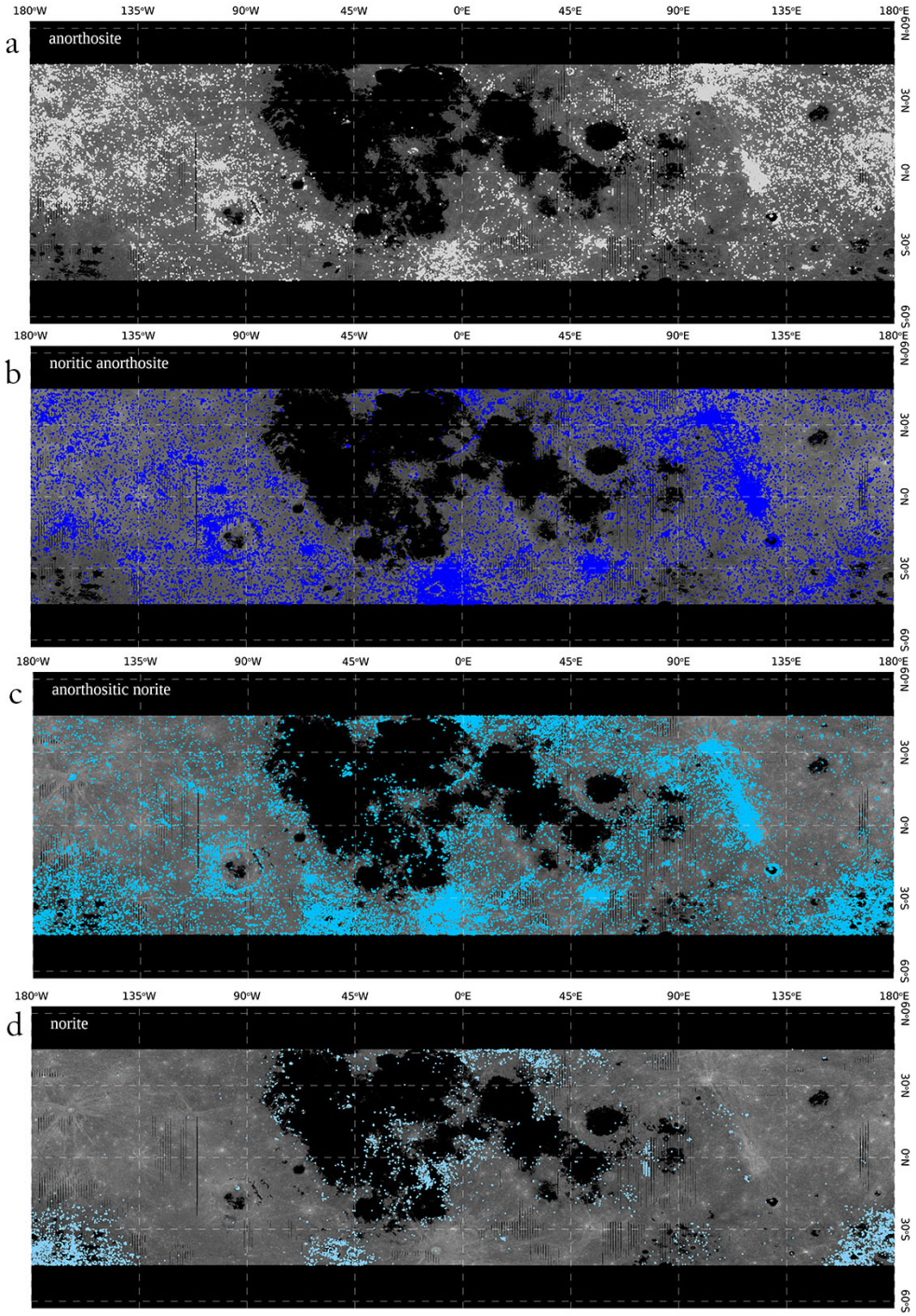

Figure 2.11: Global compositional class mapping for lunar immature (OMAT $>$ 0.25) and nonmare (FeO $<$ 13 wt.%) areas. (a) anorthosite, (b) noritic anorthosite, (c) anorthositic norite, (d) norite, (e) gabbroic anorthosite, (f) anorthositic gabbro, (g) olivine gabbro, (h) gabbro, (i) olivine norite, (j) troctolitic anorthosite, (k) anorthositic troctolite, (l) troctolite. Note that mare areas are masked from the images by the FeO constraint.

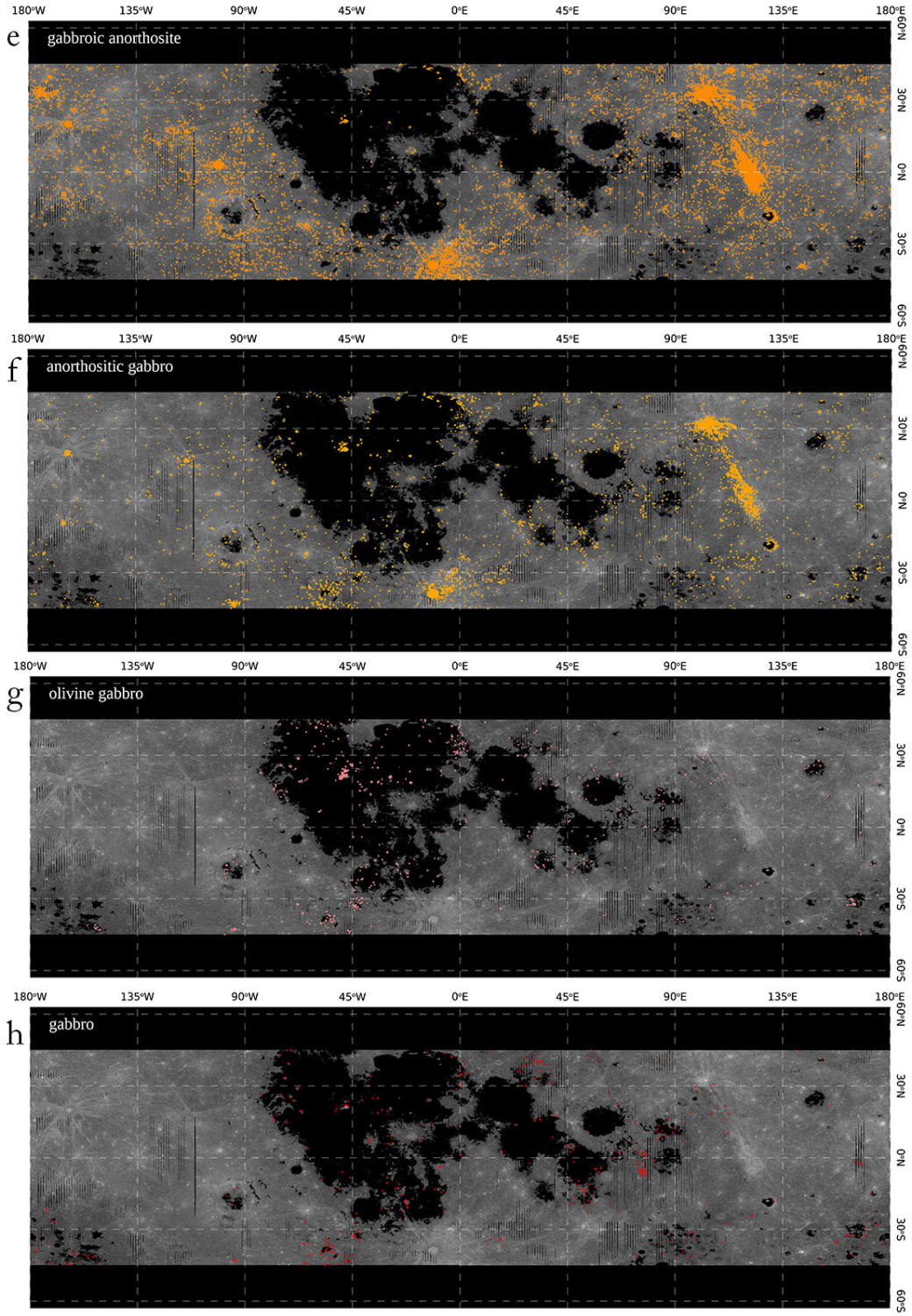

Figure 2.11: (continued)

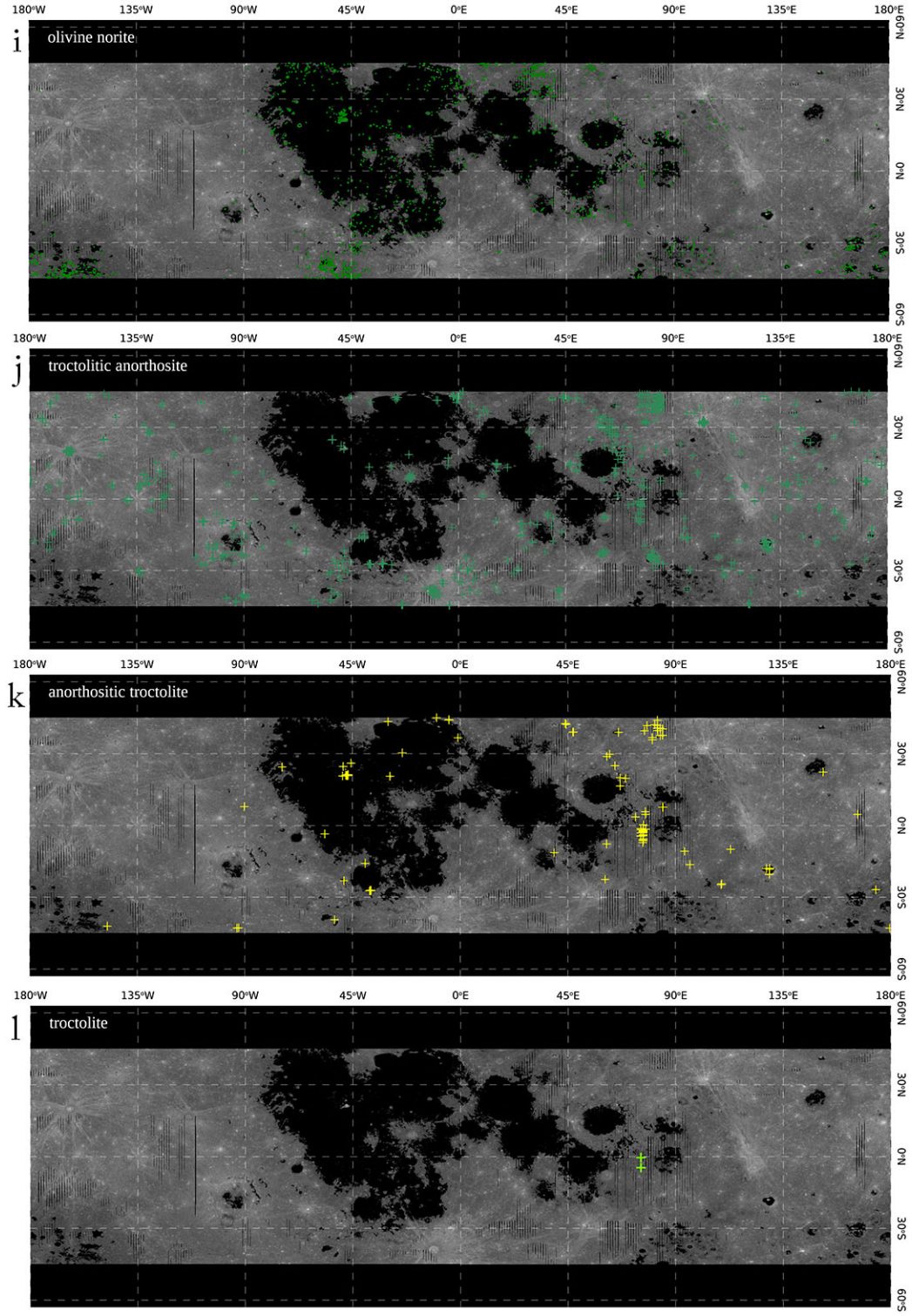

Figure 2.11: (continued)

minerals like olivine and low-Ca pyroxene had already crystallized and sunk to form the mantle. The residual magma that lay between mantle and crust is enriched in KREEP, cumulate ferroan augite (and/or pigeonite) and ilmenite; the pyroxene-ilmenite layer is denser than the underlying olivine and pyroxene (Elkins-Tanton et al., 2011). However, this arrangement is gravitationally unstable and mantle overturn might have happened, which would bring deep seated olivine and orthopyroxene to the upper mantle.

Yamamoto et al. (2010) investigated the global exposure of olivine, and they proposed that those olivine enrichments found near impact basins originated from the upper mantle. Based on their discovery and the crustal thickness derived from Gravity Recovery and Interior Laboratory (GRAIL) data, Miljković et al. (2015) simulated the basin-forming impact process for Crisium and Moscovience, and they suggested that these olivine-bearing basins indeed excavated mantle materials, and they mainly represent the uppermost mantle.

SPA is much larger than Crisium and Moscovience basins, and the excavation depth of SPA should be much deeper than these two basins. It is reasonable to infer that SPA has excavated mantle materials. However, olivine rich compositional classes are not observed inside SPA, consistent with Yamamoto et al. (2010) and Melosh et al. (2017). We observed abundant distribution of low-Ca pyroxenes ($> 20\%$) in SPA instead, consistent with Lucey et al. (2014), Pieters et al. (2001) and Melosh et al. (2017). In situ data returned from Chang'E-4 also discovered low-Ca pyroxene inside SPA (Li et al., 2019; Hu et al., 2019).

Our results suggest that SPA is enriched in norites and depleted in anorthosites. According to Pieters et al. (2001), most of the anorthositic crust in this region was removed during the basin-forming bombardment, and thus revealed the underlying noritic lower crust. In spite of few outcrops of gabbros and troctolites, this lack of gabbros and olivine-bearing compositional classes (Figure 2.11) indicates that SPA and cryptomaria have a distinct composition compared to typical mare basaltic materials, supporting the result of Lucey et al. (2014). We observed concentrations of anorthositic norite, norite and olivine norite in SPA, which suggests that norites might constitute the major lower crust, indicating the presence of more than 20% low-Ca pyroxene. Except in the SPA region, we also find

enrichment of norite and anorthositic norite in Maunder crater inside Orientale, and this observation supports the equilibrium crystallization model of Vaughan et al. (2013). Since there is abundant low-Ca pyroxene in the SPA, and the FHT is more anorthositic compared to SPA, it is possible that the current FHT is composed of norites from SPA and local anorthosites.

In addition, it can be seen from anorthositic norite, norite and olivine norite maps (Figure 2.11 c, d, i) that cryptomaria Schiller-Schickard is also enriched with these minerals, which is similar to the SPA. However, there are also distributions of noritic anorthosite, anorthositic gabbro, olivine gabbro, gabbro and troctolite in Schiller-Schickard. Lucey et al. (2014) suggested that cryptomaria Schiller-Schickard has similar spectra to SPA, but our compositional class mapping results show that Schiller-Schickard has more variety in petrology compared to SPA. This is consistent with Whitten and Head (2015), who suggested that Schiller-Schickard has a large variety of mineralogy based on the band center plots; they suggested that this variety could be a result of mixing with impact ejecta from Orientale.

2.4.2 The "Two Mantles" hypothesis

Lucey et al. (2014) interpreted the noritic feature of the FHT crust to be basin ejecta. However, their analysis was focusing on immature small craters in the highlands, and these small craters are anomalous because most small craters do not expose immature or rocky materials. We suggest the highland craters from Lucey et al. (2014) penetrated the thin basin ejecta and sampled the pre-basin basement, which is uniformly noritic. The uniformity of the samples suggests these materials are not overlapping plutons, but rather a highly mixed ancient surface that formed before the mantle overturn. An LCP-rich upper mantle might have been exposed by ancient basins.

Enrichment of norites in the SPA are also suggested to be representative of upper mantle composition. Considering SPA is the most ancient existing basin on the Moon, the basin-forming event might have happened before lunar mantle overturn, and the upper mantle

mineral may be dominated by low-Ca pyroxene, as proposed in this work and by Miljković et al. (2015).

While at the late stage of lunar magma ocean differentiation, a layer enriched in ilmenite and KREEP accumulated on top of the mantle and below the anorthositic crust. This residual layer is heavier in density compared to the mantle, thus ilmenite and KREEP tend to sink down toward the deep mantle; at the same time, olivine and LCP would rise up to the upper mantle. After the mantle overturned, the upper mantle would be enriched in olivine. Since the nearside crust has been thinned by basin-forming impacts, olivine bearing upper mantle materials are suggested to have been excavated by large impact basins like Imbrium, Serenitatis and Crisium (Miljković et al., 2015; Corley et al., 2018). We mapped the ratio of olivine and the total mafic minerals in Figure 2.12, and it is evident that in the nearside, where mafic minerals are abundant, the ratio of olivine to total mafics is high on most of the basin rings.

There is an apparent quandary about the upper mantle composition between the olivine-rich features excavated by basin rings and the noritic nature of the highland and the SPA. To explain this quandary, we propose a"two mantles" hypothesis: the noritic nature revealed by SPA and highlands represents the pre-overturn upper mantle composition; while the olivine rich basin rings excavated the post-overturn upper mantle, when olivine was brought up to due to gravitational instability.

The Mg# distribution can be a good verification for this hypothesis: The exposed upper mantle compositions before overturn should be more iron rich due to Fe accumulation within magma ocean, while after mantle overturn, the upper mantle should be more magnesium rich. The lunar magma ocean solidification model from Elkins-Tanton et al. (2011) supports our hypothesis. Their model suggested that before the overturn, the Mg# of the upper mantle was about 40-60, while after overturn, the Mg# increased to ¿90. A Mg# map for lunar highlands pyroxene was developed by Ohtake et al. (2012) using Kaguya Spectral Profiler data. They suggested the average Mg# for lunar farside highlands is near 55. Gamma ray data returned by Lunar Prospector also suggested that the lunar farside

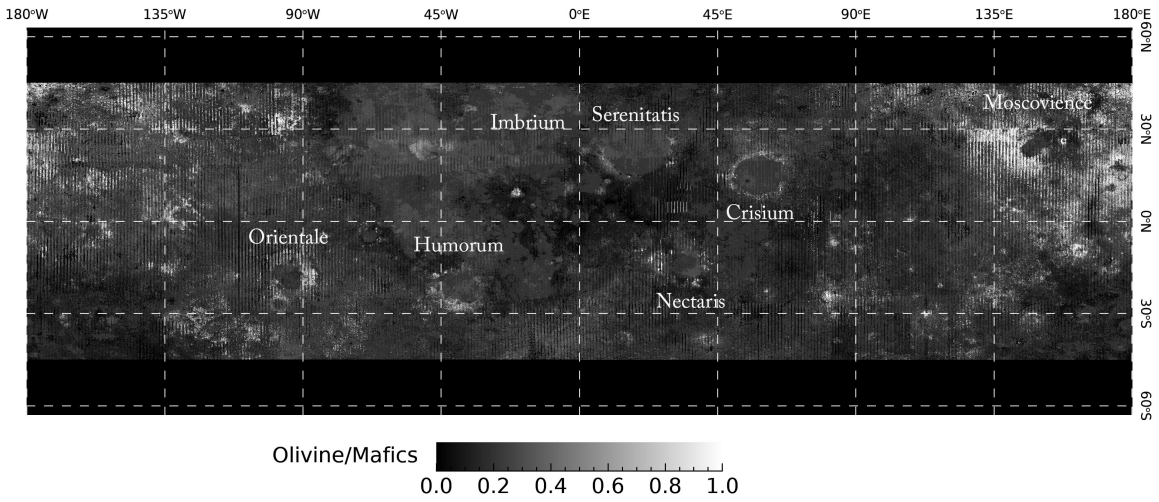

Figure 2.12: The ratio of olivine and the total of mafic minerals (olivine + LCP + HCP). On the nearside, which is enriched in mafic minerals, the ratio of olivine to total mafics is very high on the impact basin rings.

highlands have Mg# of near 60 (Crites and Lucey, 2015). Their results are consistent with the pre-overturn mantle composition. Corley et al. (2018) found high Mg# mantle olivine exposures within Crisium basin (Mg# = 90), which is consistent with a post-overturn mantle composition.

2.5 Conclusions

Using the quantitative XRD analysis of lunar soils as ground truth, we tested the mineral contents derived by radiative transfer model from MI images, then analyzed the compositional classes for Apollo 15, 16 and 17 landing stations. To determine how representative Apollo samples are, we searched for areas having similar compositional classes on both regional and global scales.

To further expand the regional study of the sampling sites, we also mapped the compositional classes for lunar global nonmare immature surfaces. We found that the FHT mainly consists of noritic anorthosite, anorthosite and anorthositic norite, while SPA mainly consists of anorthositic norite, norite and olivine norite. The enrichment of noritic

compositions indicate the presence of abundant low-Ca pyroxene in lunar highlands. We also find that olivine is not abundant in the highlands.

Noritic highland and SPA from our study suggest a LCP dominated upper mantle, while the olivine rich basin rings in the nearside trapped an olivine rich mantle. To better explain this quandary, we proposed a "two mantle" hypothesis, which suggests that the highlands and SPA were exposing a pre-overturn upper mantle that is dominated by LCP, while the basin rings trapped a post-overturn upper mantle that is dominated by olivine. This hypothesis consists with current Mg# studies and the lunar solidification model, and it can be tested by higher spatial resolution Mg# mapping results in the future.

Chapter 3

Unmixing mineral content and chemistry with radiative transfer modeling: Theory and applications

3.1 Introduction

The lunar crust is mainly composed of plagioclase, olivine and pyroxenes, and their relative abundances are closely related to the origin of crustal rocks. These minerals can be detected through spectroscopy, and because the source rocks are mixtures of minerals, they mostly occur in the form of mixtures. The relative abundances of minerals define the types of rocks present on the Moon and contribute to understanding the origin and evolution of the lunar crust.

Due to the reduced environment of the Moon, major lunar mineral absorptions in the near infrared wavelengths are dominated by Fe^{2+}. When Fe^{2+} is situated in a crystal field, the energy level of its d orbitals split, allowing absorption of photons at specific wavelengths (Burns and Burns, 1993). For example, pyroxenes usually have two diagnostic absorptions at 1 and 2 microns and olivine has three overlapping diagnostic absorptions centered near 900 nm, 1050 nm and 1200 nm in the one micron region. These absorption features vary with mineral chemistry. The three olivine absorption centers shift toward longer wavelengths with decreasing forsterite number (Fo=molar $Mg \times 100/(Mg + Fe)$)

(Sunshine and Pieters, 1998). Pyroxene absorption centers shift toward longer wavelengths with increasing wollastonite number (Wo=molar $Ca \times 100/(Ca+Fe+Mg)$) and decreasing enstatite number (En=molar $Mg \times 100/(Ca+Fe+Mg)$)(Klima et al., 2011).

Currently, the most widely used algorithms in mineral unmixing using near IR spectra are the Modified Gaussian Model (MGM) (Sunshine et al., 1990) and radiative transfer models (Hapke, 1981). MGM uses a Gaussian curve to fit each absorption band, and it has been successfully applied in deriving relative abundances of mafic minerals from mixtures, such as high-Ca and low-Ca pyroxene mixtures (Noble et al., 2006), and pyroxene and olivine mixtures (Clénet et al., 2011). MGM has also been applied to near IR spectra acquired by the lunar rovers Yutu and Yutu-2 for quantitative analysis of local mineral abundances (Ling et al., 2015; Li et al., 2019). However, it is difficult to use MGM to retrieve the abundances of plagioclase from lunar soils, since the characteristic absorption of plagioclase near 1250 nm is weak, susceptible to loss from shock and is easily obscured by the optical effects of space weathering.

In contrast, radiative transfer models can take advantage of the high reflectance of plagioclase to overcome the inconsistency of its absorption feature. Radiative transfer theory describes the relation between the optical behavior (e.g., reflectance) and grain properties within a medium (Hapke, 1981). Major factors that can affect the optical behavior of the medium include sizes and absorbance of grains, porosity and viewing geometry. One approach of spectral unmixing using radiative transfer modeling is to compute a large library of spectra of mineral mixtures (plagioclase, olivine, orthopyroxene and clinopyroxene) that can be compared to an unknown spectrum to estimate mineral abundances.

There are many applications in deriving mineral maps by applying radiative transfer models to remotely sensed datasets. Using radiative transfer modeling and the five-band UVVIS spectral images from Clementine, Lucey (2004) mapped the global distribution of plagioclase, olivine, orthopyroxene and clinopyroxene. Radiative transfer modeling has also been applied to investigate lunar crustal compositions through central peaks, which represent exposures of crustal materials at different depth, such as Cahill et al. (2009) and

Lemelin et al. (2015), who used Clementine UVVIS and Kaguya Multiband Imager data, respectively, to analyze the mineralogy of lunar global central peaks. Lemelin et al. (2019) also applied a radiative transfer model to analyze the mineral abundances of impact basin rings.

However, most of these radiative transfer models used end members with fixed mineral chemistry (i.e., Mg#) to represent the major minerals on the Moon. Investigations of Apollo samples have shown the Mg# of lunar regolith varies from 40 to over 90 (Wieczorek et al., 2006). An Mg# map derived by Ohtake et al. (2012) using pyroxenes and Kaguya Spectral Profiler data suggests that Mg# variation within lunar crust can be detected. Corley et al. (2018) analyzed olivine exposures on the Moon with data from Chandrayaan-1 Moon Mineralogy Mapper (M^3), and they determined that exposures of olivine having Mg# = 65 and Mg# = 90 were generated from different geologic progresses and sources.

The variation of Mg# can cause significant variation in the spectral properties of olivine and pyroxenes. For olivine, when Mg# changes from 90 to 40, the three one micron absorptions of olivine can shift by up to 100 nm toward longer wavelengths, and significant changes in the intensity of absorption bands were also observed by Sunshine and Pieters (1998). Pyroxene spectra vary with both Mg# and Ca content. When Mg# changes from 90 to 40, absorption centers near one micron can shift about 50 nm and that near two microns by 150 nm. When the relative abundance of Ca varies from 0% to 50%, absorption centers can shift about 100 nm near one micron and over 200 nm near two microns (Klima et al., 2011). Therefore, the use of a fixed Mg# is not able to cover the variation of mineral chemistry on the Moon and introduces as-=yet unquantified abundance errors.

The key for deriving Mg# using radiative transfer modeling is quantifying the optical constants of minerals as a function of mineral chemistry, because optical constants govern the absorption and scattering of lunar soils. Optical constants are composed of a real part n and an imaginary part k, and they must be measured as a function of chemistry. Direct measurements of optical constants requires gem quality samples, which are not available for many compositions. However, optical constants can be modeled from spectra of powdered

pure minerals using radiative transfer theory. The real index n has often been treated as a constant for a mineral with certain chemistry because it does not vary substantially with wavelength, and Lucey (1998) provided equations to estimate n for olivine, orthopyroxene and clinopyroxene. The imaginary index k carries the absorption information regarding Fe^{2+} and varies with wavelength. Lucey (1998) modeled k spectra with composition by correlating k values at each wavelength to Mg#. Denevi et al. (2007) used MGM to deconvolve k spectra of pyroxenes, then they developed correlations between Gaussian parameters and Fs (ferrosilite number=molar Fe/(Fe+Mg+Ca)), Wo. Trang et al. (2013) updated this correlation using synthetic pyroxenes, and they also modeled the optical constants for olivine. With these correlating relationships and radiative transfer theory, the spectra of olivine, orthopyroxene and clinopyroxene at any given chemistry can be simulated.

Lawrence and Lucey (2007) developed an algorithm for estimating mineral abundances and chemistries with radiative transfer modeling, and they suggested that a wider composition range for pyroxene optical constants can improve the model accuracy. Cahill et al. (2010) also introduced a radiative transfer model that can derive mineral mode and Mg#, but their comparison with LSCC (Lunar Sample Characterization Consortium) soils suggest poor results for low Mg# soils, and they recommended to improve the optical constants for low Mg# minerals.

In this work, we present updated optical constants for olivine with Fo ranging from 0.1 to 97, orthopyroxene with En ranging from 0 to 97.5, and clinopyroxene with Wo ranging from 8 to 46 and En ranging from 0 to 52. Based on the new optical constants, we develop a radiative transfer model that can calculate mineral content and chemistry. Forward modeling is applied with powdered pure minerals and LSCC lunar soils to test the ability of deriving reflectance spectra from known mineral mode and Mg#. We also apply inverse modeling to derive a spectral mixing library with both varying mineral abundances and Mg#. To test the accuracy in estimating mineral contents and Mg#, we add noise comparable to the Kaguya Multiband Imager (MI) data into our spectral library and report

the errors caused by noises. The mineral mode and Mg# of LSCC lunar soils are modeled and compared to those measured by X-ray digital imaging. A global Mg# map is produced using our model and Moon Mineralogy Mapper images, and this Mg# map is compared with that developed by Lunar Prospector gamma-ray data.

3.2 Radiative transfer theory

If a medium is filled with closely packed particles, and their grain sizes are large compared to wavelengths, then the reflectance of this medium can be described with an equivalent thin slab model (Hapke, 1981, 2001, 2012), which allows us to relate reflectance to the optical constants of the grains. Optical constants consist of a real part n and an imaginary part k. For the real part n, we apply equations 8a-c from Lucey (1998). For the imaginary part k, we introduce in this section how to derive it from reflectance based on a more complete radiative transfer model than that used by Lucey (1998).

3.2.1 Bidirectional reflectance

The bidirectional reflectance equation (Hapke, 1986, 2012) that we use in this work is expressed as:

$$r(i,e,g) = K\frac{\omega}{4}\frac{1}{\mu_0+\mu}\left\{P(g)\left[1+B(g)\right]+\left[H(\mu_0/K)H(\mu/K)-1\right]\right\}, \tag{3.1}$$

where r is the reflectance factor, defined by the ratio of reflectance to a standard that is measured under the same illumination geometry (Hapke, 2012), which is relevant to most cases of laboratory measured reflectance. The average single-scattering albedo (SSA) is expressed as ω. The illuminating geometry for the spectra we use in this work is at incidence angle $i = 30°$, extinction angle $e = 0°$ and phase angle $g = 30°$, and their cosine values are used in the equation, $\mu_0 = cos(i)$, $\mu = cos(e)$. Equation (3.1) also includes the porosity coefficient K (defined below), the single particle phase function $P(g)$, the opposition effect $B(g)$ and the Ambartsumian-Chandrasekhar H function that governs isotropic scattering.

The porosity of lunar soils has a strong effect on reflectance, but it has been neglected in previous derivations of optical constants, leading to systematic errors in average k values. The porosity coefficient K describes how closely the particles are embedded within the medium, and it can be calculated with the filling factor ϕ from (Hapke, 2012)

$$K = -\frac{ln(1 - 1.209\phi^{2/3})}{1.209\phi^{2/3}}. \tag{3.2}$$

For lunar soils, filling factor $\phi = 0.41$ based on the values reported by Hapke (1986), so $K = 1.64908$. Usually, when the porosity of the medium increases, filling factor ϕ and K decrease, and reflectance decreases because more shadow can be seen by the detector (Hapke, 2008).

Porosity can affect reflectance by affecting the opposition effect, including shadow hiding opposition effect (SHOE) and coherent backscatter opposition effect (CBOE). We only consider SHOE here because for a medium having less than 0.5 filling factor (like lunar soils), the effect of CBOE is trivial (see Figure 2 from Hapke (2008)). SHOE can be calculated with

$$B(g) = (1 + \frac{tan(g/2)}{h_s})^{-1}, \tag{3.3}$$

(from equation 9.27 of Hapke (2012)), where h_s is the angular half width at half maximum of SHOE and can be estimated by

$$h_s = \frac{3\sqrt{3}}{8}\frac{K\phi}{ln(1000)} \tag{3.4}$$

(Hapke, 2012). Taking the values of K and ϕ into equation (3.4), then $h_s = 0.06357$, and the corresponding angular width of SHOE is around 7.3°. To inspect the influence of SHOE with different phase angles, we plotted the values of B(g) versus phase angle in Figure 3.1. B(g) reaches its maximum at zero phase angle and decreases with increasing phase angle.

P(g) is the single particle angular scattering function, and it describes the anisotropic scattering of the particles within a medium. $P(g)$ can be estimated by a two-term Legendre polynomials:

$$P(g) = 1 + b \cdot cos(g) + c \cdot (1.5cos^2(g) - 0.5) \tag{3.5}$$

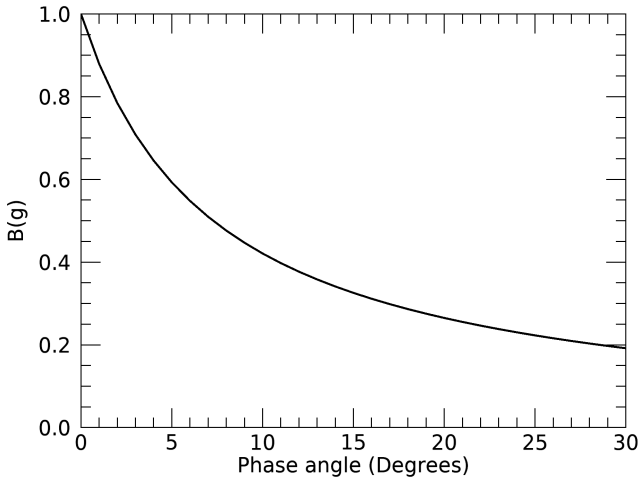

Figure 3.1: B(g) values at phase angles ranging from 0° to 30°.

(Hapke, 1981). Mustard and Pieters (1989) studied the values of b, c for a set of minerals including olivine, enstatite, anorthite and magnetite, and the Lucey (1998) model used average values of b and c from Mustard and Pieters (1989): $b = -0.4, c = 0.25$, which are also applied in this model. This set of values for b and c mainly reflect the forward scattering.

Hapke (2002) presented an improved approximation for the Ambartsumian-Chandrasekhar H function, and the accuracy is <1%,

$$H(x) = [1 - \omega x(r_0 + \frac{1 - 2r_0 x}{2} ln \frac{1 + x}{x})]^{-1}, \tag{3.6}$$

where

$$r_0 = \frac{2}{1 + \sqrt{1 - \omega}} - 1. \tag{3.7}$$

We can calculate single scattering albedo from reflectance using equations (3.1)-(3.7), or derive reflectance from single scattering using equations (3.7)-(3.1).

3.2.2 Converting between optical constants and single scattering albedo

From the equivalent slab model of Hapke (2012), the single scattering albedo (SSA) can be expressed by the equation below:

$$\omega = S_e + (1 - S_e)(1 - S_i)\frac{\Theta}{1 - S_i\Theta}, \tag{3.8}$$

where S_e and S_i are the integral of external and internal Fresnel reflection coefficients of all the grains (Hapke, 2012). For major lunar minerals, the optical constants satisfy the conditions $1.2 \leq n \leq 2.2$ and $k \ll 1$ (Hapke, 1981). Then, based on the estimation of Lucey (1998), S_e and S_i can be expressed as:

$$\begin{aligned} S_e &= \frac{(n-1)^2}{(n+1)^2} + 0.05, \\ S_i &= 1.014 - \frac{4}{n(n+1)^2}. \end{aligned} \tag{3.9}$$

The absorption of light when it transmits within grains is Θ, and when the absorption coefficient α is small, it can be expressed as

$$\Theta = e^{-\alpha\langle D\rangle}, \tag{3.10}$$

where

$$\alpha = \frac{4\pi k}{\lambda}, \tag{3.11}$$

and $\langle D\rangle$ represents the thickness of the equivalent slab, which can be calculated with the average grain size D (Hapke, 2012),

$$\langle D\rangle = \frac{2}{3}\big[n^2 - \frac{1}{n}(n^2-1)^{3/2}\big]D. \tag{3.12}$$

From equations (3.10) and (3.11), we have

$$k = \frac{1}{4\pi\langle D\rangle} ln\frac{1}{\Theta}, \tag{3.13}$$

where Θ can be solved by rearranging equation (3.8) to

$$\Theta = \big[\frac{(1 - S_e)(1 - S_i)}{\omega - S_e} + S_i\big]^{-1}. \tag{3.14}$$

Therefore, k can be expressed by

$$k = \frac{1}{4\pi\langle D\rangle} ln\big[\frac{(1-S_e)(1-S_i)}{\omega - S_e} + S_i\big]. \tag{3.15}$$

On one hand, using equations (3.8) - (3.12), we will be able to calculate single scattering albedo if optical constants n and k, and grain size D are given. On the other hand, the imaginary part of optical constants k can also be calculated using equation (3.15) if SSA, n and D are known. This transform is important for calculating the imaginary part of optical constants k for laboratory measured olivine, orthopyroxene and clinopyroxene, which allows us to explore correlations between k and mineral chemistries.

3.2.3 Difference in imaginary index k

Using different radiative transfer equations can result in significant differences in the k values. The spectra of k are calculated from the reflectance spectra of olivine from the Hawai‘i green sand beach (PO27 from Sunshine and Pieters (1998), Fo = 89, D = 22.5 μm) using equations (3.1)-(3.15) from this work and those from Lucey (1998), and the two k spectra are overplotted in Figure 3.2. Spectra of k from these two algorithms both show characteristic absorption features of olivine, but obvious differences in k values can be observed. Higher k values derived from this work are mainly caused by including porosity and the opposition effect in the Hapke functions (equation 3.1).

3.3 Modeling optical constants with mineral chemistry

We update the optical constants because: 1) We are using new radiative transfer equations (equation 3.1) that include lunar soil porosity and back scattering effect, thus the k values would be different from models that neglect these factors; 2) Olivine k is modeled with a wider range of Fo (e.g., Fo = 0-97) than that of Trang et al. (2013); 3) We found that classifying pyroxenes into orthopyroxene (Wo $\sim$ 0) and clinopyroxene (0<Wo<50) can result

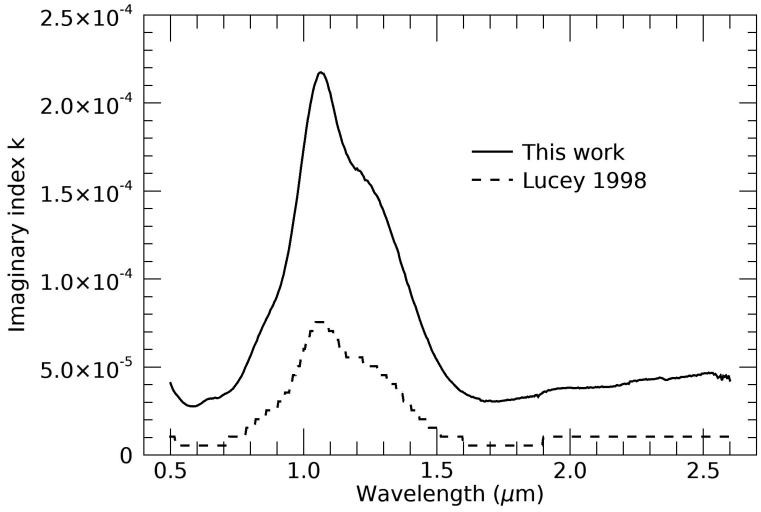

Figure 3.2: Spectra of the imaginary index k of olivine from Hawai'i green sand beach. Solid line is k calculated using equations (3.1) - (3.15) from this work, and dashed line is k calculated using the algorithm introduced in Lucey (1998).

in better fits compared to the low-Ca pyroxene (Wo<20) and high-Ca pyroxene (Wo>20) used by Trang et al. (2013).

The Fo of olivine, Wo and En of orthopyroxene and clinopyroxene that are used in this work are plotted in Figure 3.3 and listed in Table 3.1. Olivine data have an Fo range of 0.1-97 based on the olivine analyzed by Sunshine and Pieters (1998), King and Ridley (1987), and those from Mineral and Rock Sample Database at Center for Terrestrial and Planetary Exploration (https://ctape.uwinnipeg.ca/Sample_Database/) by Cloutis (2020). Orthopyroxenes (Wo $\sim$ 0) come from Klima et al. (2007), and the En of these data ranges from 0 to 97.5. Clinopyroxene data are from Klima et al. (2011), and their chemistries are: Wo ranges from 8 to 46, En ranges from 0 to 52, and Mg# range is 0 - 85. Clinopyroxenes having Wo greater than 49 are excluded in this work because: 1) Ca-saturated pyroxenes are not very common within lunar soils (Noble et al., 2006; Moriarty and Pieters, 2016), 2) excluding Ca saturated clinopyroxene can improve the correlation between optical constants and chemistries because their spectral features are less similar to those having Wo $<$ 49 (Klima et al., 2011).

Following the basic approach of Denevi et al. (2007), we used MGM analysis to deconvolve k spectra of olivine, orthopyroxene and clinopyroxene, then build correlations between k spectral parameters and mineral chemistries. We first removed the continuum for k, then used MGM to deconvolve the continuum removed k spectrum to obtain the center, width and strength of each Gaussian absorption. Then, the k spectrum can be expressed as the sum of the continuum and the major Gaussian curves. The continuum was calculated using a linear function in wavenumber space with the two bands found at the k minimum. Wavelength searching ranges for local k minimum are 0.65 - 0.95 μm and 1.45 - 1.85 μm for olivine, and 0.65 - 0.85 μm and 1.35 - 1.7 μm for orthopyroxene and clinopyroxene.

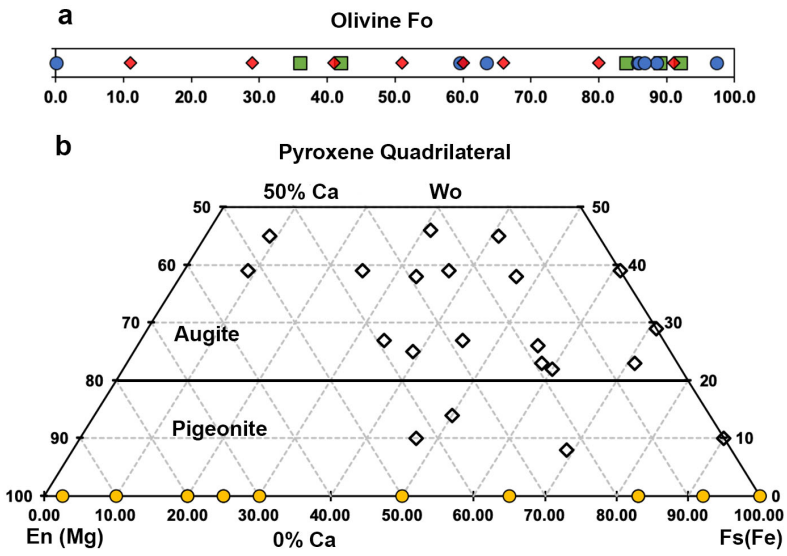

Figure 3.3: Chemistry index for olivine and pyroxene used in this study. (a) Olivine Fo numbers using data from three sources: green boxes are from Sunshine and Pieters (1998), blue circles are from Cloutis (2020), and red diamonds are from King and Ridley (1987). (b) Pyroxene quadrilateral. Golden dots are orthopyroxene from Klima et al. (2007), and black diamonds are clinopyroxene from Klima et al. (2011).

3.3.1 Olivine

Olivine k spectra before and after continuum removal are shown in Figure 3.4. Following the method of Denevi et al. (2007), we modeled the three overlapping absorptions at one

Table 3.1: Chemistry index of olivine (Fo), orthopyroxene (En) and clinopyroxene (En, Wo). The grain size range for orthopyroxene and clinopyroxene is 0-45 μm; we used a median value at 22.5 μm here. The grain sizes (D) for olivine are listed below.

Olivine			Orthopyroxene		Clinopyroxene		
Spectral ID	Fo	D(μm)	Spectral ID	En	Spectral ID	En	Wo
PO-CMP-076	92	22.5	DL-CMP-002-A	80	DL-CMP-009	43	10
PO-CMP-074	42	22.5	DL-CMP-003-A	75	DL-CMP-011	36	14
PO-CMP-072	36	22.5	DL-CMP-004-A	50	DL-CMP-050	19	23
PO-CMP-031	84	22.5	DL-CMP-020-A	17	DL-CMP-051	39	27
PO-CMP-027	89	22.5	DL-CMP-021-A	8	DL-CMP-053	23	8
OLV025	85.7	22.5	DL-CMP-022-A	75	DL-CMP-054	6	23
OLV022	63.4	22.5	DL-CMP-024-A	17	DL-CMP-055	18	26
OLV021	85.9	22.5	DL-CMP-025-A	35	DL-CMP-056	18	22
OLV020	59.5	22.5	DL-CMP-026-A	70	DL-CMP-057	36	25
OLV011	0.1	22.5	DL-CMP-027-A	80	DL-CMP-058	28	27
OLV010	88.5	22.5	DL-CMP-061-A	0	DL-CMP-066	15	38
OLV007	97.3	22.5	DL-CMP-064-A	97.5	DL-CMP-067a	52	39
OLV002	86.7	22.5	DL-CMP-065-A	90	DL-CMP-068	29	38
KI4143	41	30			DL-CMP-070	14	45
KI3291	29	30			DL-CMP-071	23	46
KI3189	60	30			DL-CMP-073a	36	39
KI3188	51	30			DL-CMP-074a	24	39
KI3054	66	30			DL-CMP-075	46	45
KI3005	11	30			DL-CMP-085	0	39
HS285.2B	80	37			DL-CMP-087	0	29
GDS71.b	91	30			DL-CMP-088	0	10

micron centered near 0.9 μm (M1), 1.0 μm (M2) and 1.2 μm (M1) with MGM for the continuum removed olivine k spectra. Figure 3.5 displays MGM analysis for a forsterite (Fo = 97.3) and a fayalite (Fo = 0.1), compared to the same olivine analyzed by Sunshine and Pieters (1998), the relative strength among the three olivine absorptions analyzed by this study is consistent with Sunshine and Pieters (1998). Our continuum is determined by finding local minima values on the spectra, which is common in remote sensing, thus our modeled relative strength at 0.9 μm and 1.0 μm bands will be slightly weaker compared to the continuum removal method used by Sunshine and Pieters (1998), and the center wavelength of the three absorptions may also be slightly affected.

The absorption center, width and strength of the three Gaussian absorptions for each olivine k spectrum are extracted from MGM deconvolution, and listed with the continuum wavelengths and k values in Table 3.2. Least squares regressions are applied to fit the

spectral parameters with olivine Fo. In order to achieve better fits, we used linear regression (equation 3.16) for the center, continuum wavelengths and k values, and quadratic regression (equation 3.17) for the width and strength. The regression results are shown in Figure 3.6, and the regression parameters and coefficient of determination R^2 are listed in Table 3.3.

$$Y = A + B \cdot Fo \tag{3.16}$$

$$Y = A + B \cdot Fo + C \cdot Fo^2 \tag{3.17}$$

From Figure 3.6, the absorption centers of the three bands migrate toward longer wavelengths with decreasing Fo (or increasing Fe/Mg), with each band shows a different decreasing rate. The two M1 bands centered near 0.9 μm and 1.2 μm decrease more rapidly than the M2 band centered near 1.0 μm, consistent with those observed by Sunshine and Pieters (1998) and Burns (1970). The width of the three absorptions show poor correlations with Fo, except for a slightly decreasing trend with increasing Fo (Figure 3.6). This decreasing trend is more obvious in the plot of widths versus centers (Figure 3.7a).

The strengths of the three bands decrease with Fo from Figure 3.6, and this decreasing trend is also obvious from the plot of strength versus absorption centers in Figure 3.7b. We also plot the strength normalized to 1.2 μm versus absorption center wavelengths in Figure 3.7c, and find the strength of k shows a similar variation trend to those observed by Sunshine and Pieters (1998) for olivine reflectance, and by Trang et al. (2013) for olivine k: the relative strengths of the two M1 bands is almost constant, suggesting a strong coupling between the M1 bands; the relative strengths of M2 band and longer M1 band show a significant decreasing trend with decreasing Fo.

The continuum wavelength near 0.65 μm for all the olivine k spectra is almost a constant, so we used an average wavelength of 0.66 μm instead of fitting it to Fo (Figure 3.6). The continuum wavelengths near 1.7 μm decrease linearly with Fo. This continuum variation suggests that the total width of the three overlapping olivine absorptions shrinks with increasing Mg/Fe ratio. The k values of the two continuum bands both decrease with Fo,

and k values near 0.65 μm decrease linearly with Fo, and they becomes more scattered near 1.7 μm .

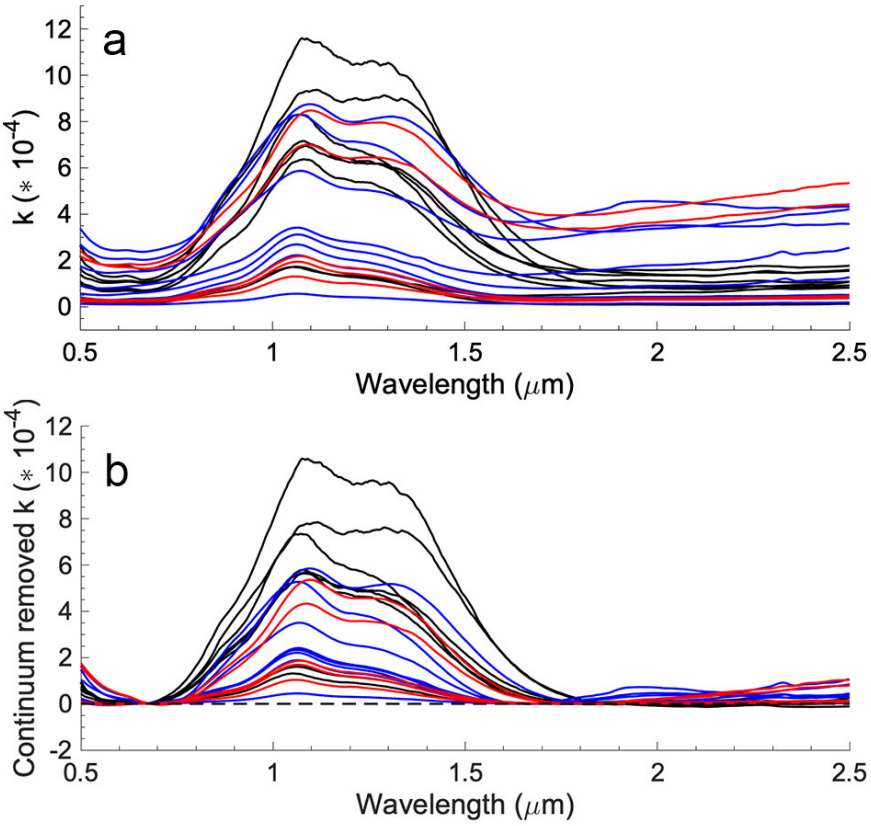

Figure 3.4: Olivine k spectra (a) before and (b) after continuum removal. Olivine from Sunshine and Pieters (1998) are shown in red, Cloutis (2020) olivine is shown in blue, and King and Ridley (1987) olivine is shown in black.

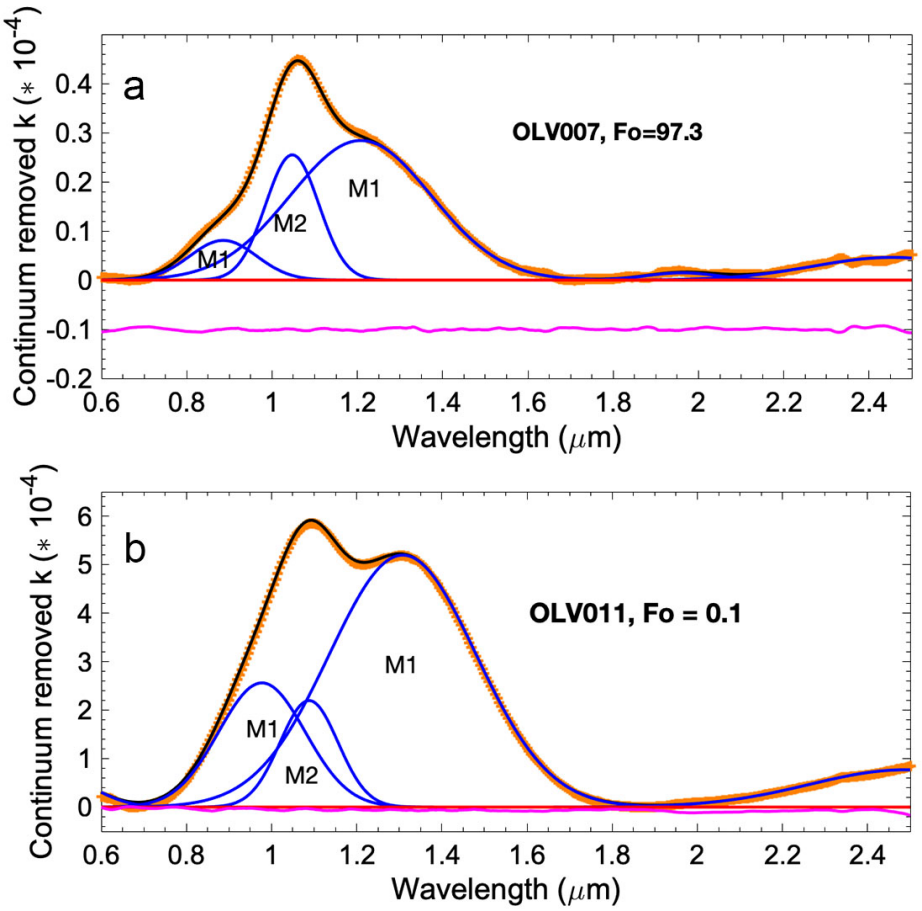

Figure 3.5: MGM analysis for (a) Forsterite, Fo = 97.3, and (b) Fayalite, Fo = 0.1.

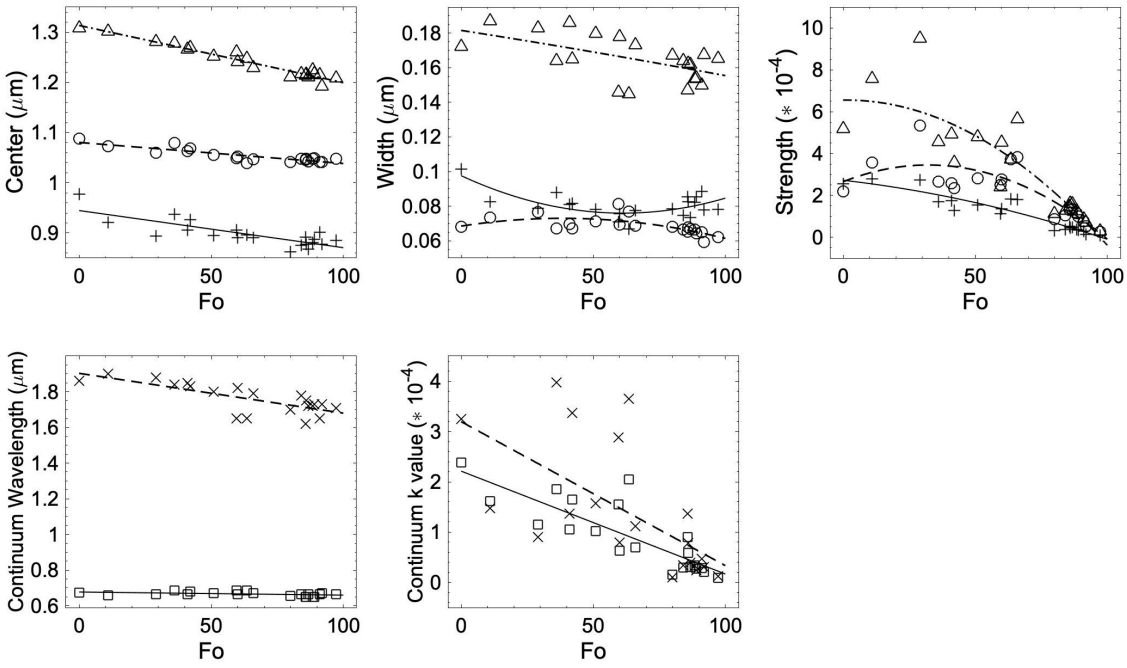

Figure 3.6: Olivine MGM analysis results. Top: from left to right are absorption centers, widths, and strengths of the three overlapping absorptions centered near 0.9 μm (pluses), 1.0 μm (circles) and 1.2 μm (triangles) regress with Fo, and the best fits are overplotted with solid lines for 0.9 μm, dashed lines for 1.0 μm and dash-dot lines for 1.2 μm. Bottom: from left to right are the wavelengths and k values of the two continuum removal bands near 0.65 μm (squares) and 1.7 μm (crosses) regressed with Fo, best fits are overplotted with solid lines for 0.65 μm and dashed lines for 1.7 μm. The regression parameters and coefficient of determination R^2 are listed in Table 3.3.

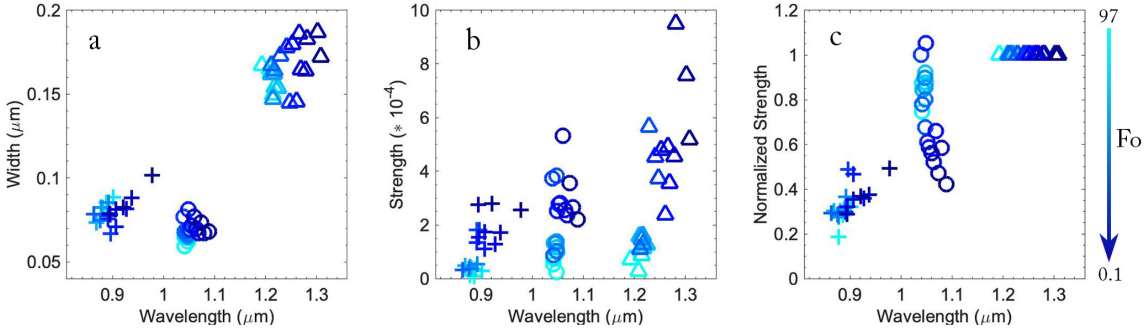

Figure 3.7: (a) width, (b) strength and (c) strength normalized to 1.2 μm for the three olivine absorptions near 0.9 μm (pluses), 1.0 μm (circles) and 1.2 μm (triangles) versus absorption center wavelength, and the shade of blue darkens with decreasing Fo.

Table 3.2: MGM analysis results for olivine k spectra, including the center, width and strength of the three Gaussian curves from MGM analysis of olivine k spectra, and wavelengths and k values of the two continuum removal bands. Olivine are from those analyzed by Sunshine and Pieters (1998) and King and Ridley (1987), and listed at Mineral and Rock Sample Database at The Center for Terrestrial and Planetary Exploration (Cloutis, 2020).

			Gaussian curves									Continuum			
			Center (μm)			Width (μm)			Strength($*10^{-4}$)			Wavelength (μm)		k value($*10^{-4}$)	
	Spectral ID	Fo	0.9 μm	1.0 μm	1.2 μm	0.9 μm	1.0 μm	1.2 μm	0.9 μm	1.0 μm	1.2 μm	0.65 μm	1.7 μm	0.65 μm	1.7 μm
Sunshine, 1990	PO76	92.0	0.877	1.041	1.192	0.078	0.059	0.167	0.132	0.531	0.710	0.670	1.730	0.210	0.302
	PO74	42.0	0.927	1.068	1.269	0.082	0.067	0.165	1.277	2.353	3.562	0.680	1.830	1.648	3.368
	PO72	36.0	0.938	1.080	1.278	0.088	0.067	0.164	1.707	2.666	4.562	0.685	1.840	1.849	3.975
	PO31	84.0	0.875	1.048	1.217	0.075	0.066	0.164	0.368	1.032	1.288	0.665	1.780	0.291	0.337
	PO27	89.0	0.888	1.049	1.217	0.085	0.064	0.154	0.350	0.991	1.130	0.650	1.730	0.271	0.237
Cloutis	OLV025	85.7	0.892	1.046	1.214	0.085	0.065	0.147	0.536	1.316	1.464	0.650	1.620	0.906	1.368
	OLV022	63.4	0.896	1.039	1.248	0.067	0.077	0.145	1.816	3.732	3.726	0.685	1.650	2.048	3.654
	OLV021	85.9	0.877	1.048	1.216	0.082	0.068	0.162	0.445	1.373	1.606	0.650	1.750	0.586	0.783
	OLV020	59.5	0.906	1.049	1.261	0.071	0.081	0.146	1.112	2.511	2.386	0.685	1.650	1.549	2.880
	OLV011	0.1	0.977	1.088	1.308	0.102	0.068	0.172	2.561	2.197	5.195	0.675	1.860	2.381	3.247
	OLV010	88.5	0.881	1.048	1.224	0.082	0.067	0.154	0.380	1.159	1.259	0.650	1.720	0.342	0.330
	OLV007	97.3	0.885	1.047	1.208	0.078	0.062	0.165	0.081	0.255	0.284	0.665	1.710	0.093	0.119
	OLV002	86.7	0.868	1.042	1.210	0.074	0.067	0.162	0.477	1.330	1.578	0.665	1.720	0.304	0.391
King and Ridley, 1987	KI4143	41.0	0.906	1.063	1.266	0.081	0.070	0.186	1.741	2.568	4.918	0.665	1.850	1.054	1.372
	KI3291	29.0	0.894	1.060	1.281	0.079	0.077	0.183	2.745	5.329	9.507	0.665	1.880	1.153	0.898
	KI3189	60.0	0.891	1.052	1.241	0.076	0.069	0.178	1.349	2.770	4.539	0.665	1.820	0.626	0.797
	KI3188	51.0	0.895	1.055	1.252	0.078	0.071	0.180	1.545	2.823	4.801	0.670	1.800	1.025	1.577
	KI3054	66.0	0.891	1.047	1.229	0.078	0.069	0.173	1.807	3.824	5.648	0.670	1.790	0.699	1.119
	KI3005	11.0	0.921	1.073	1.301	0.082	0.074	0.187	2.791	3.568	7.574	0.660	1.900	1.614	1.474
	HS285.2B	80.0	0.863	1.041	1.211	0.078	0.068	0.167	0.327	0.868	1.114	0.655	1.700	0.152	0.105
	GDS71.b	91.0	0.901	1.041	1.215	0.088	0.065	0.150	0.280	0.759	0.869	0.665	1.650	0.285	0.470

Table 3.3: The regression parameters for olivine Gaussian absorption centers, widths and strengths, and the continuum wavelengths and k values. The coefficient of determination R^2 for each regression is also listed.

			A	B(Fo)	C(Fo^2)	R^2
Gaussian curves	Center	0.9 μm	9.4473E-01	-7.3988E-04		0.65
		1.0 μm	1.0804E+00	-4.1948E-04		0.77
		1.2 μm	1.3135E+00	-1.1383E-03		0.95
	Width	0.9 μm	9.7633E-02	-7.0675E-04	5.7682E-06	0.50
		1.0 μm	6.8488E-02	2.3499E-04	-3.0610E-06	0.48
		1.2 μm	1.8155E-01	-2.3787E-04	-2.3284E-07	0.33
	Strength	0.9 μm	2.7212E-04	-1.4402E-06	-1.3829E-08	0.88
		1.0 μm	2.6519E-04	4.9644E-06	-7.7070E-08	0.70
		1.2 μm	6.5552E-04	1.5407E-07	-7.0952E-08	0.76
Continuum	Wavelength	0.65 μm	6.7741E-01	-1.7597E-04		0.19
		1.7 μm	1.9033E+00	-2.2325E-03		0.59
	k value	0.65 μm	2.2128E-04	-2.0447E-06		0.69
		1.7 μm	3.1965E-04	-2.8621E-06		0.41

3.3.2 Orthopyroxene

Orthopyroxene k spectra before and after continuum removal are shown in Figure 3.8. Two orthopyroxenes from Klima et al. (2007) were excluded because their k spectra show extremely strong absorption strengths and they were distinct from the others. For the MGM analysis, we used three bands centered near 0.9 μm (M1 & M2), 1.2 μm (M1) and 2.0 μm (M2) to model the continuum removed k spectra (Figure 3.9). The Gaussian parameters from MGM and continuum wavelengths and k values for all the orthopyroxene k spectra are listed in Table 3.4.

Least squares regressions are applied to fit the Gaussian parameters and the continuum wavelengths and k values with En. We used linear regressions for the Gaussian centers, widths and continuum wavelengths (equation 3.18) and quadratic regressions for the strength and continuum k values (equation 3.19). The fitting results are shown in Figure 3.10, and the regression parameters and coefficient of determination R^2 are listed in Table 3.5.

$$Y = A + B \cdot En \tag{3.18}$$

$$Y = A + B \cdot En + C \cdot En^2 \tag{3.19}$$

From Figure 3.10, wavelengths of absorptions centered near 0.9 μm, 1.2 μm and 2.0 μm all decrease linearly with En. Based on the regression relations we derived with equation (3.18) (coefficients are listed in Table 3.5), when En decreases from 100 to 0, the center wavelength of the three bands shift within the range of 0.91 - 0.95 μm, 1.1 - 1.22 μm and 1.83 - 2.1 μm, respectively. The band center at 2 μm shifts faster than those near one micron with En. The band widths of the 2 μm absorption are wider than those of the two absorptions near one micron, and they all decrease linearly with En.

The strength of the three absorptions decrease with En, and the rate decreases when En is high (Figure 3.10). The band at 0.9 μm is the strongest, which could be a combination effect of Fe^{2+} situating in M1 and M2 sites, strength at 2.0 μm being slightly weaker than 0.9 μm, and the 1.2 μm band being the weakest. Our observations of the variation trend for the absorption curves are consistent with those of Klima et al. (2007).

The continuum wavelengths near 0.65 μm do not vary significantly with En, so we used a fixed wavelength at 0.7 μm. The continuum wavelengths near 1.5 μm decrease linearly with En. The k values at the continuum bands show a variation trend similar to that of the strength of Gaussian curves: it decreases with En, and the variation rate decreases when En increases.

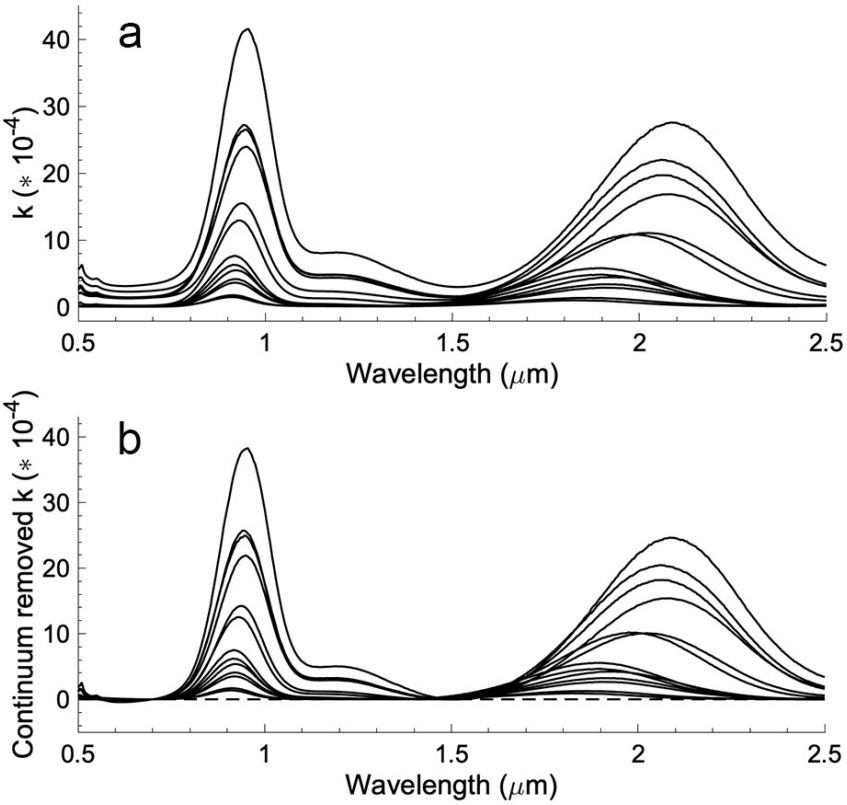

Figure 3.8: Orthopyroxene k spectra (a) before and (b) after continuum removal.

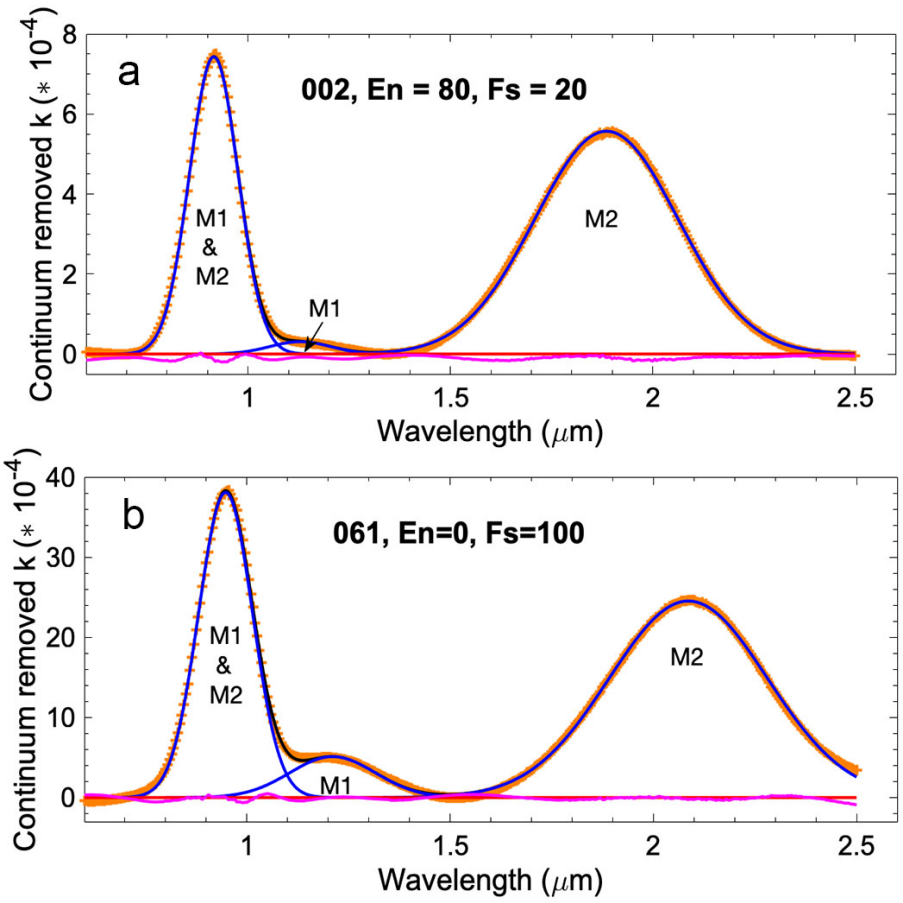

Figure 3.9: MGM analysis of (a) Mg orthopyroxene, En = 80 and (b) Fe orthopyroxene, En = 0.

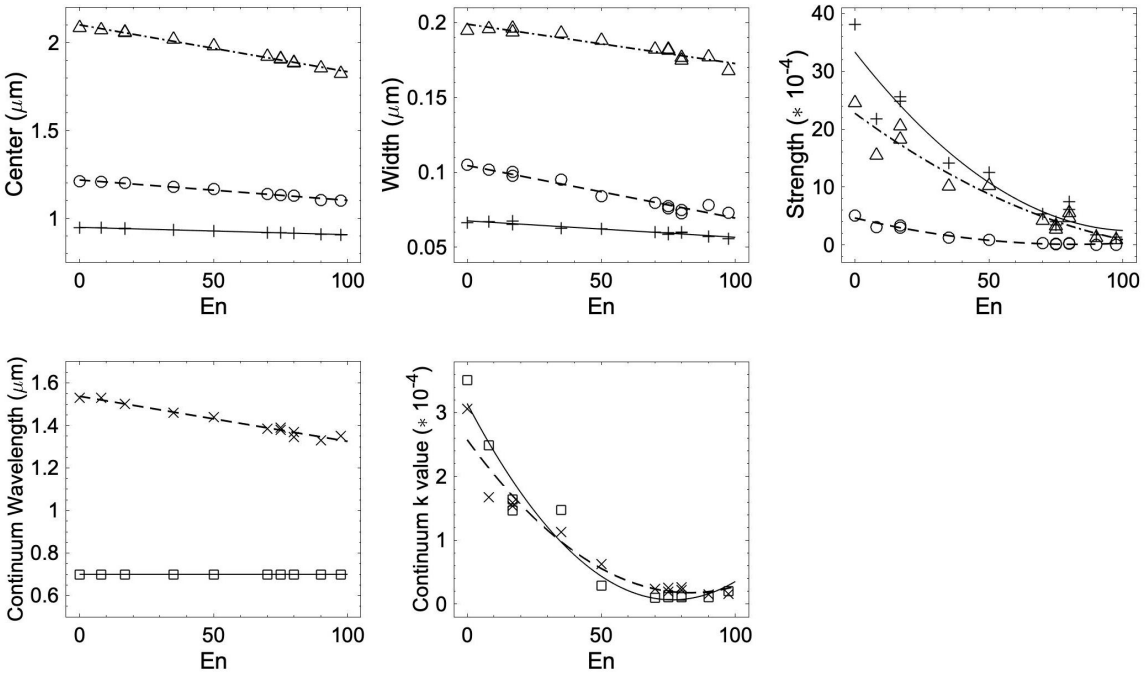

Figure 3.10: Orthopyroxene MGM analysis results. Top: from left to right are absorption centers, widths, and strengths of the absorptions centered near 0.9 μm (pluses), 1.2 μm (circles) and 2.0 μm (triangles) regress with En, and the best fits are overplotted with solid lines for 0.9 μm, dashed lines for 1.2 μm and dash-doted lines for 2.0 μm. Bottom: from left to right are the wavelengths and k values of the two continuum removal bands near 0.65 μm (square) and 1.5 μm (crosses) regress with En, best fits are overplotted with solid lines for 0.65 μm and dashed lines for 1.5 μm. The regression coefficients and coefficient of determination R^2 are listed in Table 3.5.

Table 3.4: MGM analysis of orthopyroxene k spectra, including the center, width and strength of the three Gaussian curves, wavelengths and k values of the two continuum removal bands. Orthopyroxene data are from Klima et al. (2007).

		Gaussian curves									Continuum			
		Center (μm)			Width (μm)			Strength ($*10^{-4}$)			Wavelength (μm)		k values ($*10^{-4}$)	
spectral ID	En	0.9 μm	1.2 μm	2.0 μm	0.9 μm	1.2 μm	2.0 μm	0.9 μm	1.2 μm	2.0 μm	0.65 μm	1.5 μm	0.65 μm	1.5 μm
002	80	0.916	1.129	1.886	0.060	0.075	0.177	7.434	0.309	5.570	0.700	1.345	0.134	0.259
003	75	0.918	1.131	1.909	0.060	0.078	0.182	4.035	0.178	3.223	0.700	1.380	0.104	0.193
004	50	0.928	1.168	1.981	0.062	0.084	0.188	12.483	0.829	10.184	0.700	1.440	0.293	0.627
020	17	0.942	1.202	2.059	0.068	0.098	0.196	24.788	3.305	20.499	0.700	1.500	1.639	1.588
021	8	0.945	1.207	2.074	0.067	0.102	0.196	21.748	3.096	15.463	0.700	1.530	2.493	1.677
022	75	0.917	1.131	1.907	0.059	0.076	0.181	3.466	0.140	2.640	0.700	1.390	0.139	0.254
024	17	0.941	1.200	2.058	0.065	0.100	0.194	25.580	2.993	18.224	0.700	1.500	1.469	1.536
025	35	0.934	1.179	2.018	0.063	0.095	0.193	14.103	1.225	10.086	0.700	1.460	1.477	1.128
026	70	0.920	1.140	1.922	0.060	0.080	0.182	5.336	0.252	4.224	0.700	1.385	0.101	0.235
027	80	0.915	1.128	1.885	0.060	0.072	0.175	6.150	0.241	4.639	0.700	1.370	0.110	0.224
061	0	0.948	1.211	2.086	0.066	0.105	0.195	38.086	5.107	24.526	0.700	1.530	3.511	3.060
064	97.5	0.907	1.102	1.824	0.056	0.073	0.168	1.339	0.033	0.899	0.700	1.350	0.202	0.160
065	90	0.910	1.105	1.856	0.057	0.078	0.177	1.680	0.048	1.254	0.700	1.330	0.107	0.146

Table 3.5: The regression parameters for orthopyroxene Gaussian absorptions center, width and strength, and the continuum wavelength and k value. The coefficient of determination R^2 for each regression is also listed.

			A	B(En)	C(En^2)	R^2
Gaussian curves	Center	0.9 μm	9.4846E-01	-4.1602E-04		1.00
		1.2 μm	1.2183E+00	-1.1612E-03		0.99
		2.0 μm	2.1014E+00	-2.6674E-03		0.99
	Width	0.9 μm	6.7615E-02	-1.0968E-04		0.94
		1.2 μm	1.0457E-01	-3.5123E-04		0.96
		2.0 μm	1.9893E-01	-2.6298E-04		0.91
	Strength	0.9 μm	3.3326E-03	-5.9333E-05	2.8485E-07	0.93
		1.2 μm	4.6496E-04	-1.1102E-05	6.7582E-08	0.97
		2.0 μm	2.2745E-03	-3.3987E-05	1.2134E-07	0.93
Continuum	Wavelength	0.7 μm	7.0000E-01	0.0000E+00		na*
		1.5 μm	1.5371E+00	-2.1197E-03		0.98
	k value	0.7 μm	3.1442E-04	-8.0333E-06	5.2422E-08	0.95
		1.5 μm	2.5754E-04	-5.7712E-06	3.4735E-08	0.94

* Not available

3.3.3 Clinopyroxene

Imaginary index k spectra of all the clinopyroxenes before and after continuum removal are shown in Figure 3.11. Similar to orthopyroxne, clinopyroxene spectroscopy is also dominated by Fe^{2+}, which occupies the M1 site and produces absorptions at 1 and 1.2 microns, and also produces absorptions near 1 and 2 microns by occupying M2 site. In addition, Ca^{2+} occupying the M2 site in clinopyroxene can affect the symmetry of the nearby M1 sites occupied by Fe^{2+}, and thus affect the spectral absorptions. We use MGM to deconvolve the clinopyroxene absorptions at 1 μm, 1.2 μm and 2 μm for the continuum removed k spectra. Two example MGM analysis for pigeonite (Wo = 8) and augite (Wo = 45) are shown in Figure 3.12.

The absorption center, width and strength, continuum wavelength and k values from MGM analysis are plotted with Wo and En in Figure 3.13 and listed in Table 3.6. To fit these Gaussian and continuum parameters, we applied a linear least squares regression with Wo and En, shown in equation 3.20. The fitted results are shown with a plane in Figure

3.13, and the regression parameters and coefficient of determination R^2 are listed in Table 3.7.

$$Y = A + B * En + C * Wo \tag{3.20}$$

Figure 3.13 shows that the centers of all three absorptions move to longer wavelengths with increasing Wo and decreasing En. Burns and Burns (1993) suggested that when more Ca^{2+} is substituted by Fe^{2+}, both of the M2 absorptions will move to shorter wavelengths, which is consistent with what we observed. The widths of the three absorptions do not show correlated variations with En and Wo. Strengths of the three absorptions all decrease with Wo and En, but they are more scattered compared to the center and width fittings.

Comparing to olivine and orthopyroxene, the strength of clinopyroxene Gaussian curves are more scattered. Strength, width and center for the absorptions centered near 1.2 μm (M1) are poorly correlated to chemistries. This may be due to Fe^{2+} not situating in the preferred site (M2) when pyroxene experienced rapid cooling during crystallization (Denevi et al., 2007; Trang et al., 2013). In addition, presence of Ca^{2+} complicates the crystal structure and spectrum of clinopyroxene by inducing distortions to nearby sites occupied by Fe^{2+}, and equation (3.20) may not be able to completely describe the corresponding spectral variations. However, our optical constants of clinopyroxene are tested with laboratory measured pure mineral data in section 3.4.

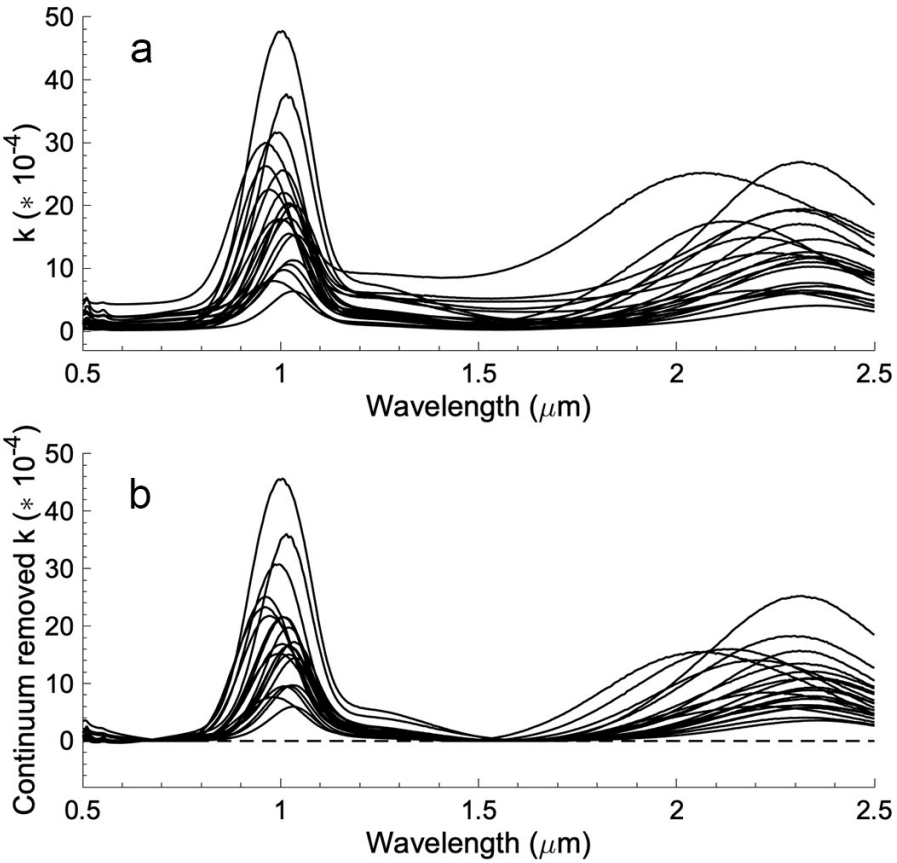

Figure 3.11: Clinopyroxene k spectra (a) before and (b) after continuum removal.

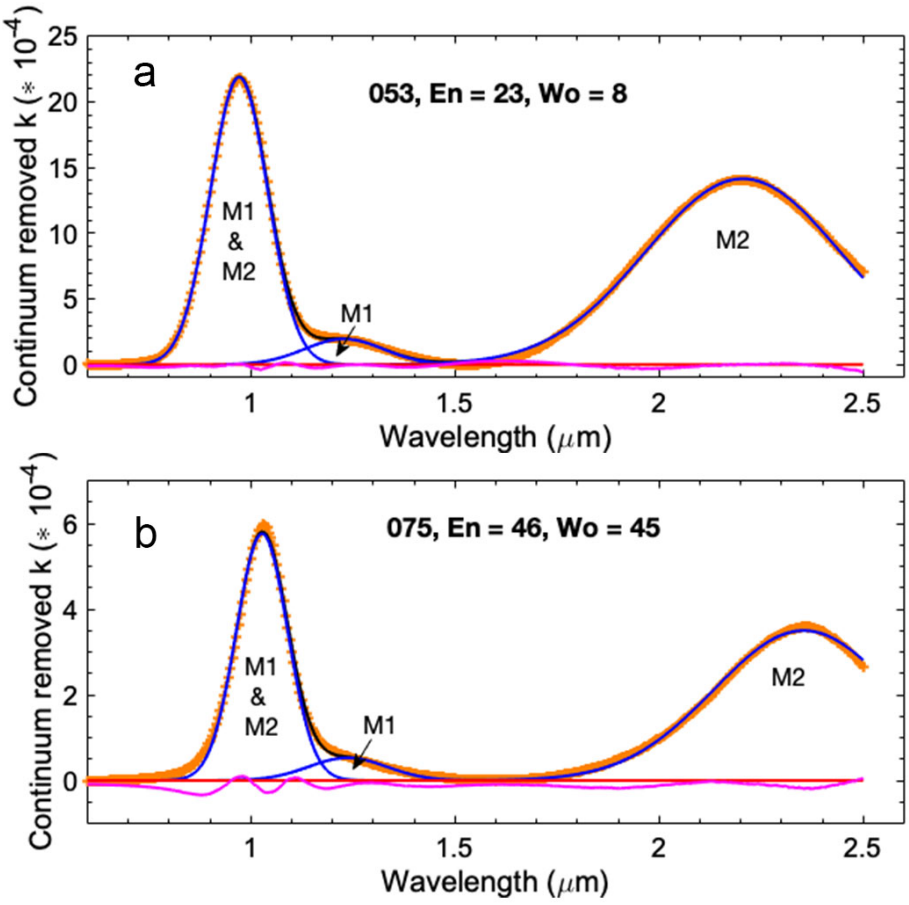

Figure 3.12: MGM analysis of (a) pigeonite, En = 23, Wo = 8 and (b) augite, En = 0, Wo=45.

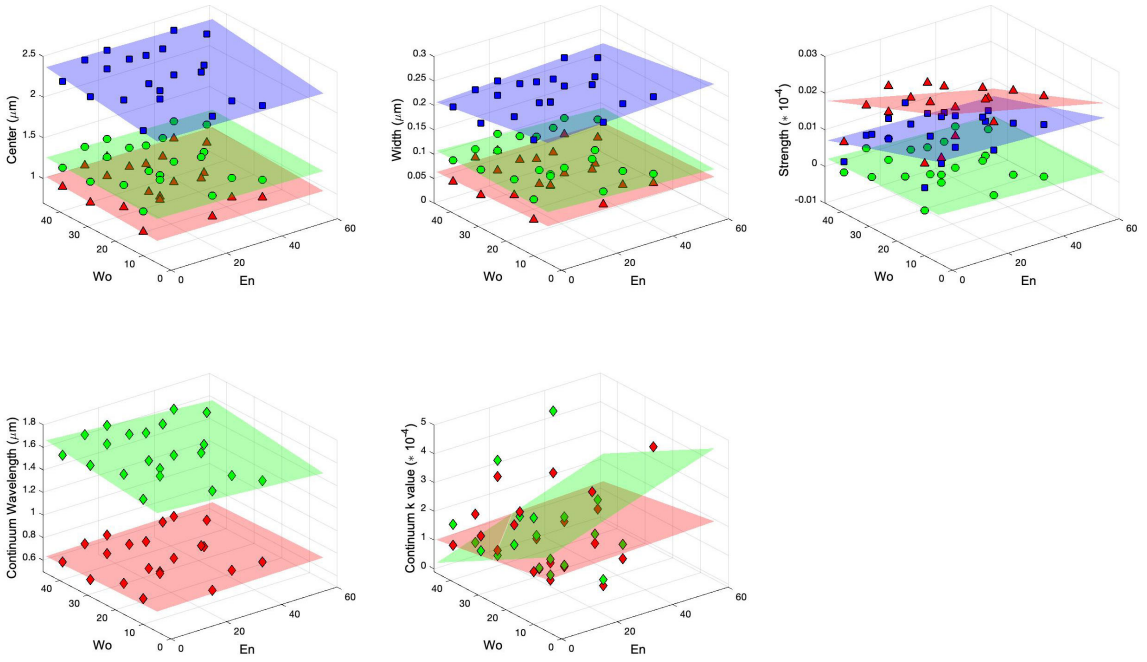

Figure 3.13: Clinopyroxene MGM analysis results. Top: from left to right are absorption centers, widths, and strengths of the absorptions centered near 0.9 μm (blue squares), 1.2 μm (green circles) and 2.0 μm (red triangles) regressed with En, and the best fits are overplotted with red surfaces for 0.9 μm, green surfaces for 1.2 μm and blue surfaces for 2.0 μm. Bottom: from left to right are the wavelengths and k values of the two continuum removal bands near 0.65 μm (red diamonds) and 1.5 μm (green diamonds) regressed with En, best fits are overplotted with red surfaces for 0.65 μm and green surfaces for 1.5 μm. The regression coefficients and coefficient of determination R^2 are listed in Table 3.7.

Table 3.6: MGM analysis results for clinopyroxene k spectra, including the center, width and strength of the three Gaussian curves, and wavelengths and k values of the two continuum removal bands.

			Gaussian curves									Continuum			
			Center (μm)			Width (μm)			Strength ($*10^{-4}$)			Wavelength (μm)		k values $*10^{-4}$	
Spectral ID	En	Wo	0.9 μm	1.2 μm	2.0 μm	0.9 μm	1.2 μm	2.0 μm	0.9 μm	1.2 μm	2.0 μm	0.65 μm	1.5 μm	0.65 μm	1.5 μm
009	43	10	0.961	1.174	2.092	0.073	0.092	0.250	23.409	1.423	15.653	0.725	1.445	4.777	8.560
011	36	14	0.962	1.200	2.146	0.069	0.098	0.236	25.028	2.010	16.143	0.650	1.490	0.895	1.401
050	19	23	0.990	1.254	2.290	0.070	0.094	0.242	30.953	2.448	18.320	0.650	1.565	0.804	0.928
051	39	27	0.997	1.258	2.320	0.069	0.097	0.246	16.695	1.315	10.754	0.670	1.575	0.680	1.001
053	23	8	0.971	1.228	2.205	0.070	0.097	0.239	21.850	1.949	14.131	0.650	1.530	0.649	0.865
054	6	23	1.000	1.270	2.313	0.075	0.106	0.235	45.772	4.997	25.127	0.650	1.615	2.508	1.828
055	18	26	1.003	1.263	2.333	0.067	0.096	0.234	21.289	1.630	11.977	0.650	1.605	0.476	0.510
056	18	22	0.980	1.228	2.217	0.076	0.095	0.246	7.621	0.917	6.064	0.655	1.520	0.290	0.462
057	36	25	1.000	1.259	2.305	0.068	0.090	0.242	21.399	1.447	13.347	0.725	1.550	2.659	5.211
058	28	27	1.002	1.253	2.317	0.069	0.080	0.247	9.316	0.698	6.165	0.650	1.565	0.207	0.258
066	15	38	1.017	1.251	2.336	0.064	0.105	0.218	14.544	1.428	7.215	0.650	1.620	0.601	0.413
067	52	39	1.016	1.240	2.352	0.064	0.101	0.227	9.288	0.782	5.772	0.650	1.605	0.872	1.192
068	29	38	1.016	1.247	2.352	0.063	0.109	0.221	19.213	1.626	10.806	0.650	1.610	0.587	0.695
070	14	45	1.032	1.259	2.327	0.071	0.089	0.210	13.718	2.068	5.661	0.650	1.620	1.525	0.536
071	23	46	1.029	1.246	2.332	0.067	0.101	0.210	16.551	2.194	7.640	0.650	1.620	2.518	3.078
073	36	39	1.016	1.245	2.342	0.062	0.112	0.211	16.153	1.084	9.120	0.755	1.625	2.617	4.764
074	24	39	1.017	1.248	2.338	0.067	0.116	0.223	15.880	1.781	8.751	0.650	1.625	1.621	1.460
075	46	45	1.028	1.237	2.354	0.063	0.096	0.220	5.763	0.528	3.500	0.650	1.600	0.306	0.470
085	0	39	1.027	1.256	2.319	0.065	0.109	0.218	9.362	1.107	4.031	0.675	1.620	1.167	1.902
087	0	29	1.012	1.266	2.311	0.067	0.119	0.214	34.970	3.862	15.521	0.650	1.660	2.003	1.491
088	0	10	0.992	1.243	2.238	0.073	0.115	0.237	15.059	2.291	8.468	0.725	1.605	1.728	3.599

Table 3.7: The regression parameters for clinopyroxene Gaussian absorptions center, width and strength, and continuum wavelength and k value. The coefficient of determination R^2 for each regression is also listed.

			A	B(En)	C(Wo)	R^2
Gaussian curves	Center	0.9 μm	9.6222E-01	-3.3329E-04	1.6790E-03	0.92
		1.2 μm	1.2348E+00	-7.5578E-04	9.4033E-04	0.47
		2.0 μm	2.1666E+00	-7.0670E-04	4.8952E-03	0.68
	Width	0.9 μm	7.6101E-02	-7.3125E-05	-2.1246E-04	0.52
		1.2 μm	1.0312E-01	-2.9375E-04	1.5893E-04	0.22
		2.0 μm	2.4999E-01	2.5323E-04	-9.0186E-04	0.70
	Strength	0.9 μm	3.1789E-03	-1.7867E-05	-2.9985E-05	0.24
		1.2 μm	3.1763E-04	-3.8642E-06	-1.5685E-06	0.37
		2.0 μm	1.8773E-03	-3.2684E-06	-2.5091E-05	0.33
Continuum	Wavelength	0.7 μm	6.8050E-01	3.6237E-04	-7.2471E-04	0.09
		1.5 μm	1.5325E+00	-1.7165E-03	3.1941E-03	0.72
	k value	0.7 μm	1.7726E-04	4.0627E-07	-1.5990E-06	0.03
		1.5 μm	2.7440E-04	3.3363E-06	-5.5308E-06	0.15

3.4 Forward modeling: replicating spectra

Forward modeling is a process using known mineral abundances (plagioclase, olivine, LCP and HCP) and chemistry (Mg#, Wo) to reproduce reflectance spectra (Lawrence and Lucey, 2007). Reflectance can be modeled using the regression coefficients of optical constants from section 3.3 and equations (3.8) - (3.12) from section 3.2. We present the reflectance for pure olivine, orthopyroxene and clinopyroxene having Mg# varying from 40 to 90 in Figure 3.14a-c, and spectra of clinopyroxene having Mg# = 60 and Wo ranging from 0 to 55 in Figure 3.14d. From Figure 3.14, absorption centers, widths and strengths of modeled spectra increase with decreasing Mg# for olivine, orthopyroxene and clinopyroxene, and the absorption center of clinopyroxene increases with Wo, consistent with those observed by previous workers (Sunshine and Pieters, 1998; Klima et al., 2007, 2011). Figure 3.14e and f show two examples of spectral mixing for olivine and clinopyroxene, orthopyroxene and clinopyroxene. These modeled spectra show that the shape of spectra varies with both mineral mode and chemistries.

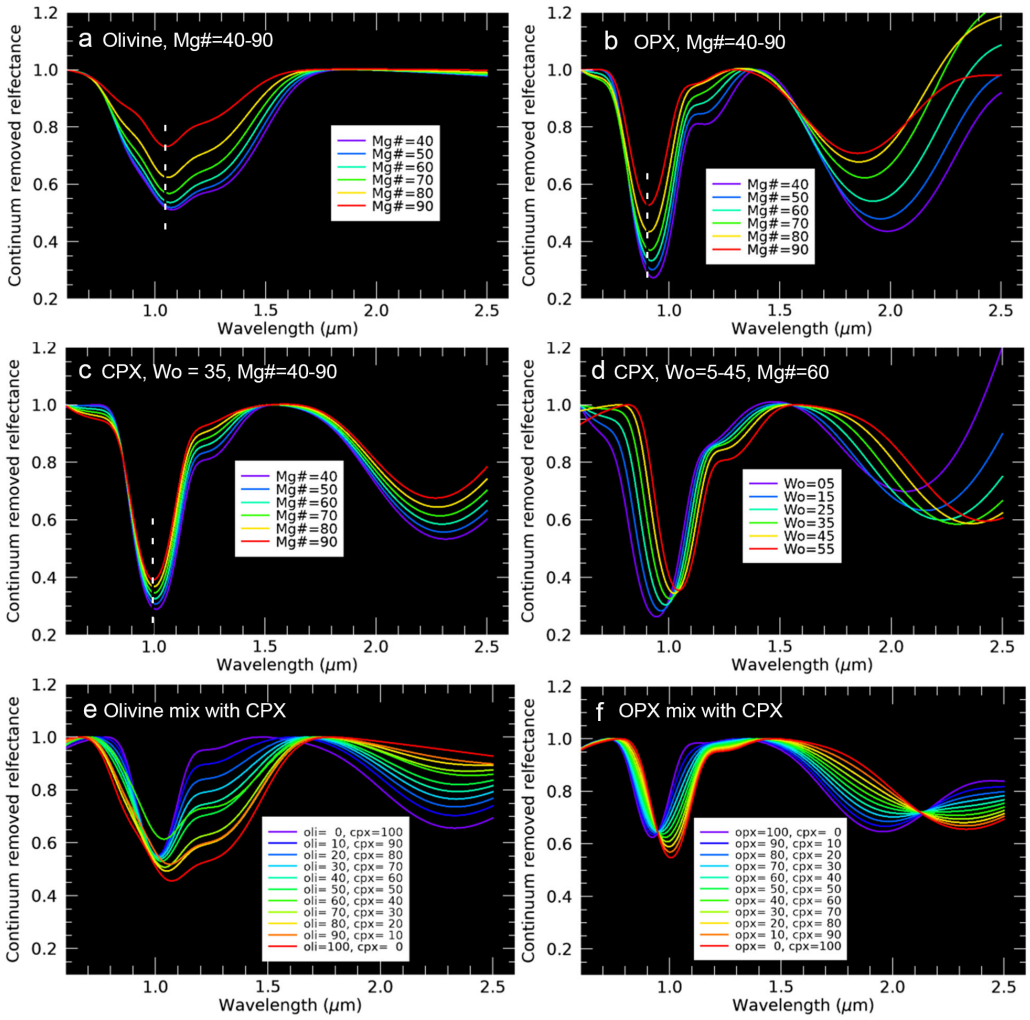

Figure 3.14: (a) Olivine and (b) orthopyroxene spectra with Mg# range from 40 to 90. (c) Clinopyroxene spectra with Wo = 35 and Mg# range from 40 to 90. (d) Clinopyroxene spectra with Mg# = 60 and Wo ranges from 5 to 45. (e) Spectral mixing of olivine and clinopyroxene, Mg# = 60. (f) Spectral mixing of orthopyroxene and clinopyroxene, Mg# = 60.

3.4.1 Modeling spectra of pure mineral end members

Data from powdered pure minerals with known chemistries measured in the laboratory are used to test the ability to derive reflectance spectra with our Hapke model and optical constants. For olivine, we used both data from Table 5 of Isaacson et al. (2014) and Table 3.1 of this work. The spectra derived from radiative transfer modeling are overplotted with

those measured in the laboratory, shown in Figure 3.15, and the Fo of olivine ranges from Fe-rich to Mg-rich. The modeled spectra are consistent with the measured ones.

For orthopyroxene, we present the modeled and measured spectra with varying En in Figure 3.16 a-d. For clinopyroxene, the modeled and measured spectra are overplotted in Figure 3.16 e-h, with both varying Mg# and Wo. Our modeled spectra of orthopyroxene and clinopyroxene both show consistent results compared with the measured laboratory spectra.

This test shows that major spectral characteristics with varying Mg# and Wo for olivine, orthopyroxene and clinopyroxene can be reproduced by our model and optical constants.

3.4.2 Modeling reflectance for LSCC lunar soils

The Lunar Soil Characterization Consortium measured reflectance spectra and the abundances of plagioclase, ilmenite, pyroxene, olivine and glasses for nineteen lunar soils using X-ray digital imaging (Taylor et al., 1996, 2001). The mineral mode and chemistry for these lunar soils can be found at: https://pgi.utk.edu/lunar-soil-characterization-consortium-lscc-data/. Each soil was sieved into four different grain sizes: $< 10\ \mu m$, 10 - 20 μm, 20 - 45 μm and $<45\ \mu m$ (Taylor et al., 1996). The 10-20 μm size fraction is used to validate our model as they are most similar to the bulk samples and dominate the major optical characteristics (Pieters et al., 1993; Lucey, 2006). Grain size D is set to 15 μm in the model.

In this work, we include four major minerals: plagioclase, olivine, low-Ca pyroxene and high-Ca pyroxene. Orthopyroxene and pigeonite from LSCC are summed as low-Ca pyroxene (LCP), and Mg-clinopyroxene and Fe-clinopyroxene are summed as high-Ca pyroxene (HCP). Pigeonite is a clinopyroxene (Wo $\sim$ 10), while spectroscopically, pigeonite is more similar to orthopyroxene than augite (Klima et al., 2011). For chemistry inputs, Mg# and Wo are from the fused bead chemistry of 10-20 μm sized LSCC soils (Taylor et al., 1996, 2001).

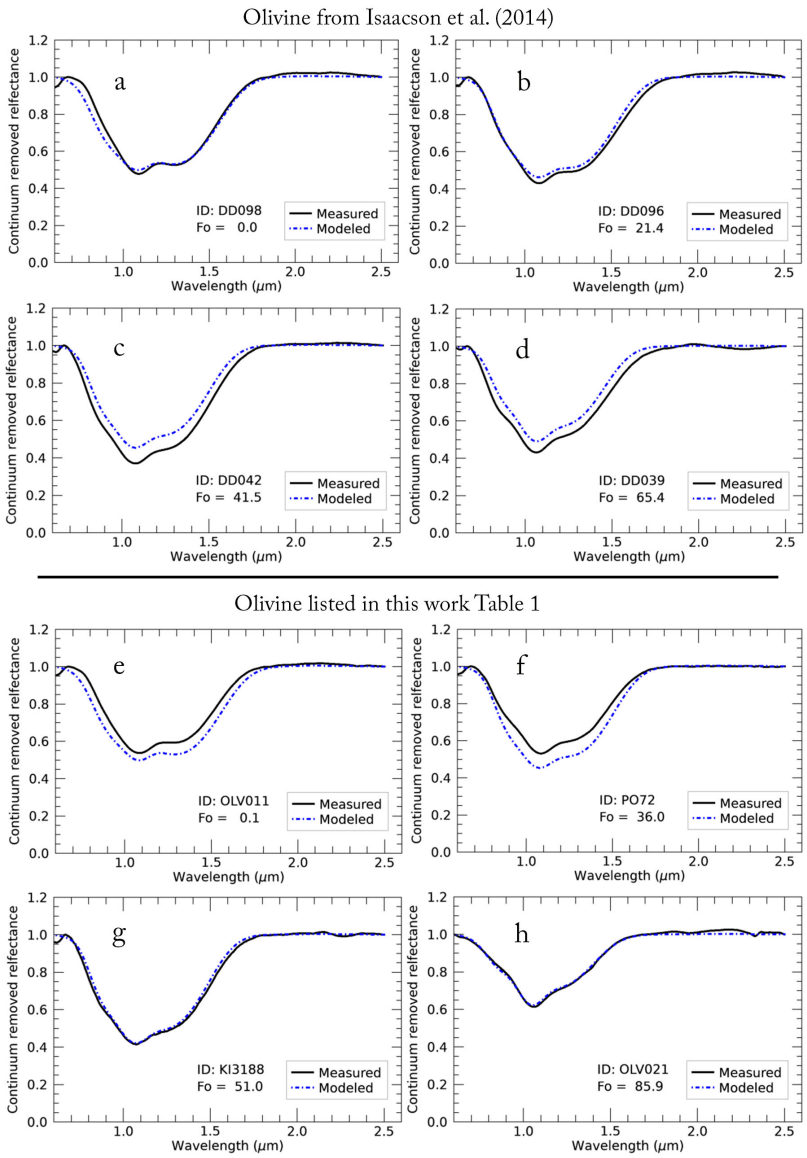

Figure 3.15: Reflectance modeled (blue dashed line) for 100% olivine and laboratory reported Fo (Mg#) compared to the laboratory measured reflectance (black solid line) of the same olivine. The spectral ID and Fo are labeled in the plot, (a-d) are from Table 5 of Isaacson et al. (2014), and (e-h) are from Table 3.1 of this work.

The comparison of modeled and measured LSCC reflectance spectra are shown in Figure 3.17. The correlation coefficients R for successful models are greater than 0.7. Overall, we successfully modeled the spectra for eighteen lunar soils and failed in modeling spectra of sample 71061 ($R^2 = 0.22$). Cahill et al. (2010) also reported the poorest results in modeling

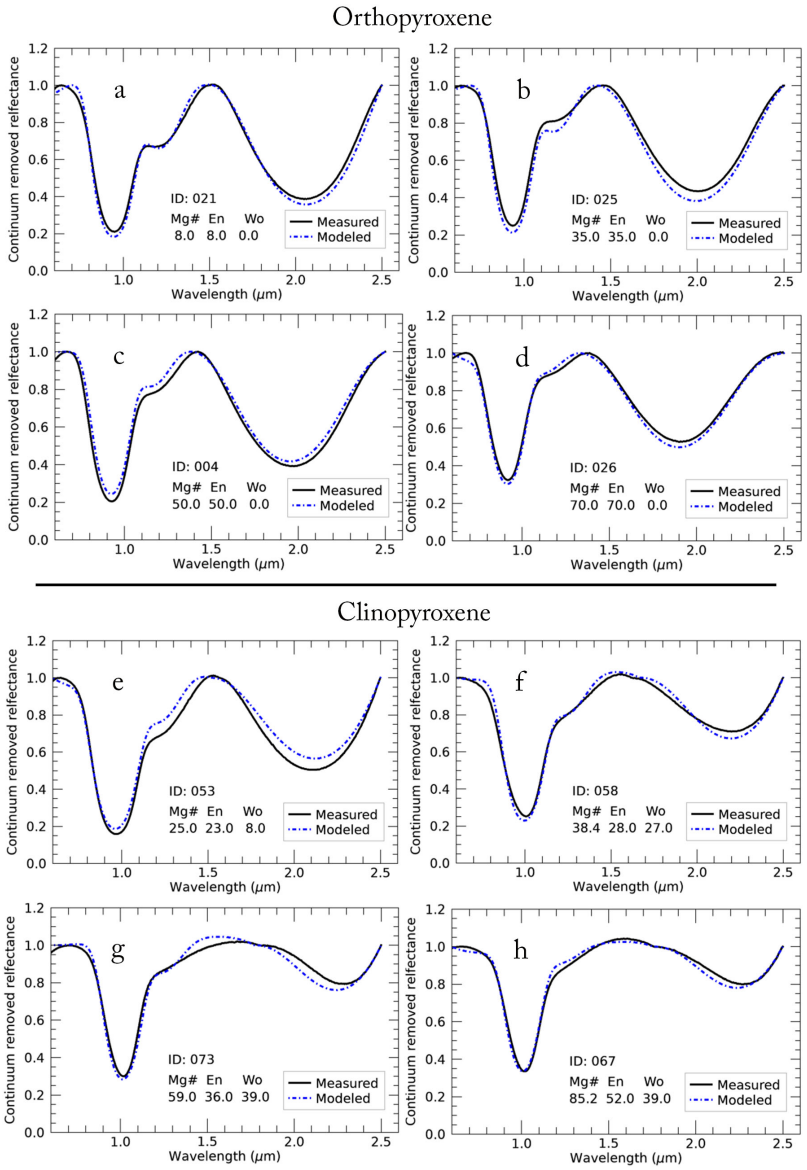

Figure 3.16: Modeled compared with laboratory measured spectra for (a-d) orthopyroxene with ranging En (Mg#) and (e-h) clinopyroxene with ranging En and Wo. Orthopyroxene and clinopyroxene data are listed in Table 3.1.

sample 71061, which could be caused by the presence of abundant black pyroclastic beads, which have optical properties not included in this model. From Figure 3.17, it can be seen that for most of the soils, absorption strength between modeled and measured spectra are more consistent near 1 micron than 2 microns.

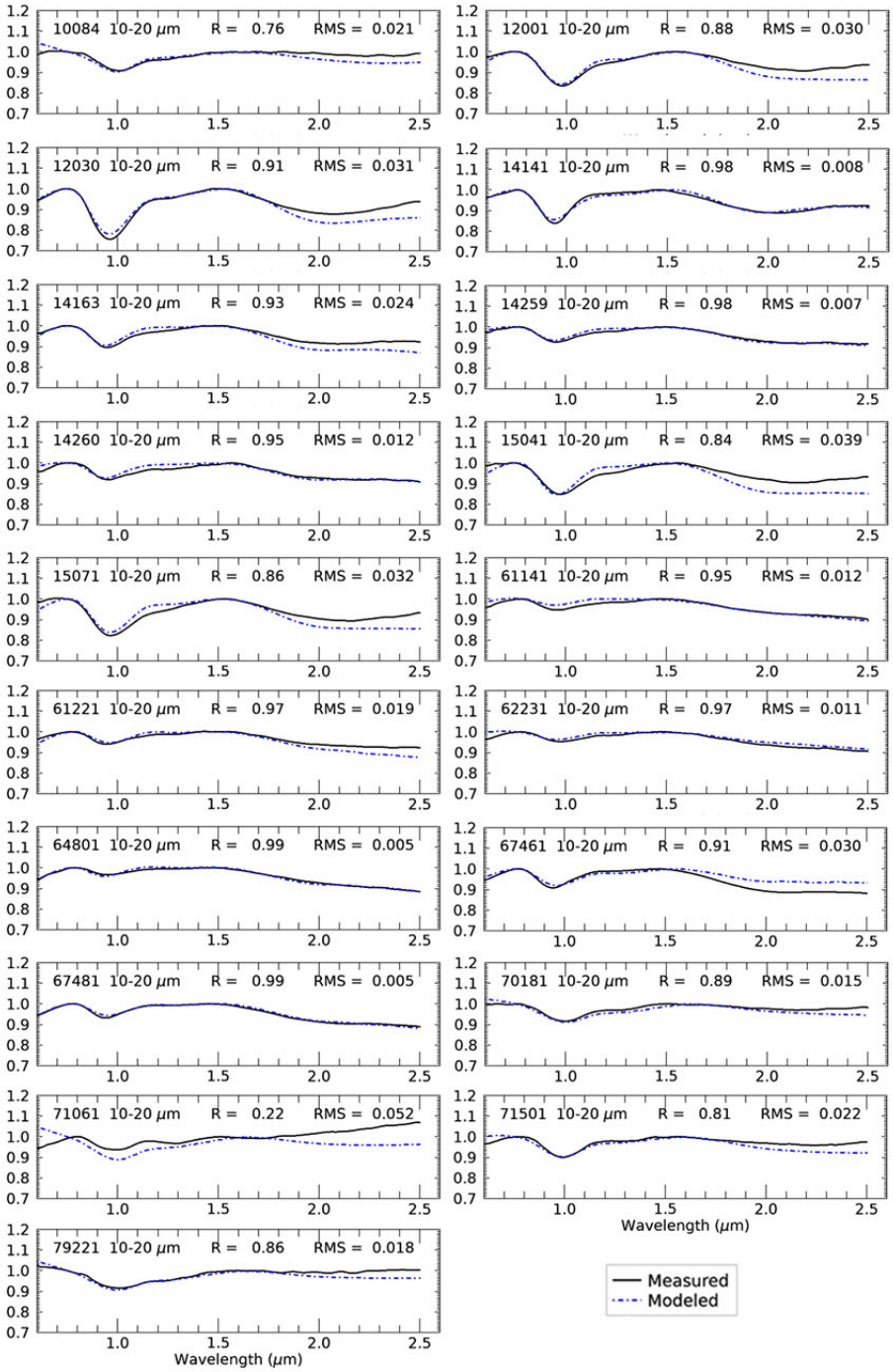

Figure 3.17: Modeled (dash-doted blue lines) versus measured (solid black lines) reflectance spectra for 19 LSCC lunar soils in the 10-20 μm size fraction; the correlation coefficient R and RMS of the two spectra over full wavelengths are labeled on the plot for each soil.

3.5 Inverse modeling: deriving mineral mode and Mg#

3.5.1 Establishing the spectral mixing library

A spectral library has been established for inverse modeling, and the procedures are shown in Figure 3.18. The first step is to build a mineral and chemistry mixing table. Olivine, LCP, HCP and plagioclase are included in the mineral mixing. The three mafic minerals are mixed within 0 - 100 vol.% at 10 vol.% steps, and 66 mixtures are derived. Each mafic mixture is then mixed with 0 to 100 vol% plagioclase at 2 vol% steps, and 3301 mineral mixtures are derived. Chemistry variations are then added into the mineral mixtures. To simplify the model, we allow the Mg# to vary from 40 to 90 at 5 intervals, and Wo is set to 0 and 35 for LCP and HCP, respectively. These mineral and Mg# combinations constitute a total of 36301 mixtures for the library.

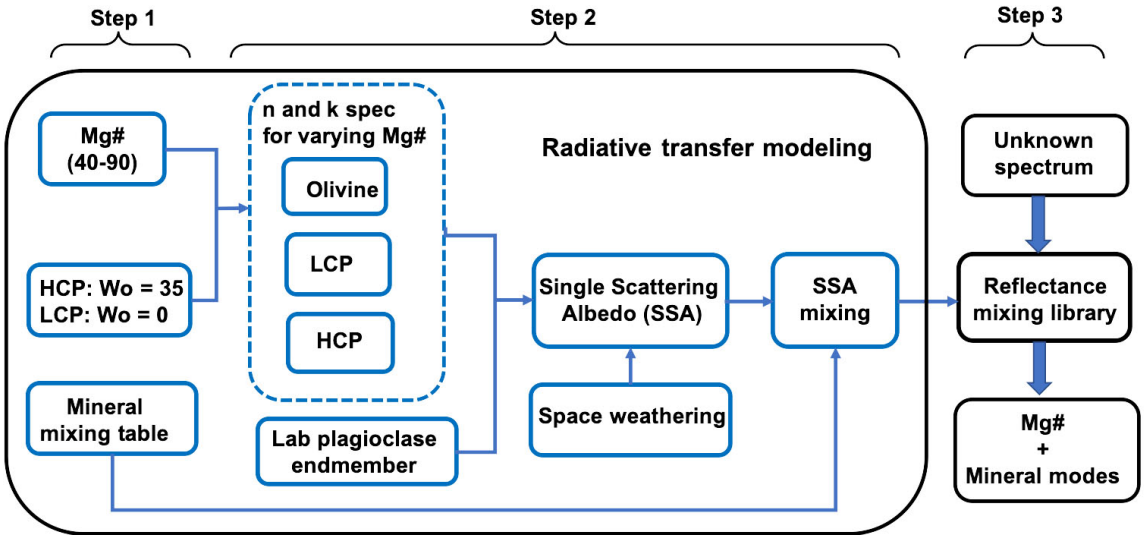

Figure 3.18: A flow chart diagram showing the modeling procedure of building the spectral mixing library and involving both varying Mg# and mineral modes (Lawrence and Lucey, 2007). Given an unknown spectrum, their Mg# and mineral modes can be derived by matching to the spectral mixing library.

The second step is to build the spectral mixing library. The single scattering albedo (SSA) of a mixture can be calculated following equation (3.21)(modified from equation 17 of Hapke (1981)), where ω_{mix} is the mixture SSA, and ω_i refers to the SSA of a single

mineral component with a specific Mg#, V_i is volume fraction of the mineral component, and D is grain size. The SSA for olivine, LCP and HCP can be determined using the optical constant coefficients introduced in section 3.3, and their volume fraction and chemistry are from the mixing table in step one. We used an anorthite spetrum (spectral ID: HS201.3B) from the U.S. Geological Survey spectral library as the plagioclase end member.

$$\omega_{mix} = \sum_i \frac{V_i}{D_i}\omega_i / \sum_i \frac{V_i}{D_i} \tag{3.21}$$

The last step is spectral matching. A criterion (CR, equation 3.22) composed of RMS and correlation coefficient (R) between the unknown spectrum and library spectra is calculated, and the least CR is used to determine the best match. We also use the abundances of FeO to constrain the spectral matching, similar to that applied by Cahill et al. (2010) and Lemelin et al. (2015). The FeO content of library mixtures are calculated stoichiometrically using mineral modes and Mg# (details can be found in Appendix A). The FeO content of the unknown spectrum can be estimated either by laboratory measurements or existing algorithms (Lucey et al., 2000a; Lemelin et al., 2015). When applying the spectral matching, the difference in FeO content between the unknown spectrum and library is limited up to ± 2 wt.%.

$$CR = 0.8 \times RMS + 0.2 \times (1 - |R|) \tag{3.22}$$

3.5.2 Sensitivity Test

To test the sensitivity of our model, we added noise to selected spectra from the look up table, and observed the effect of noise on the retrieval of composition from the spectra. We replicated each library spectrum 10,000 times and added noise comparable to that of Kaguya Multiband Imager reflectance data (see Appendix A for details of noise estimation). The spectra of nine typical lunar compositional classes as defined by Stöffler et al. (1980) (Figure 3.19a,b) are used to estimate the error of our model in deriving mineral content and

Mg#: anorthosite, noritic/gabbroic anorthosite, anorthositic norite/gabbro, norite/gabbro and olivine norite/gabbro. The mineral modes of these classes are listed under the clean columns in Table 3.8. Figure 3.19c and d show a comparison of noisy and input norite spectra when Mg# is 40 and 90.

Mineral modes of the noisy spectra are derived by matching them to the entire spectral mixing library using the criterion introduced in section 3.5.1. Figure 3.20 shows the distribution of mineral modes and Mg# of noisy spectra for norite having Mg# at 40 and 90, and the peak mineral and Mg# values of noisy spectra are consistent with the clean ones. All of the noisy test results are reported with both Mg-rich (Mg# = 90) and Fe-rich (Mg# = 40) chemistry. We list the peak values of noisy mineral modes, Mg# histograms for nine compositional classes, and the standard deviation for minerals derived from noisy spectra in Table 3.8. We plot the histograms of noisy mineral modes over the classification ternary diagrams in Figure 3.21. It can be observed that the noisy Mg# and mineral modes are highly concentrated near the clean values for all the compositional classes and different Mg#.

Based on this sensitivity test, the error of our model in deriving mineral abundances and Mg# can be estimated using the standard deviation (σ) (Table 3.8). When the clean Mg# is 40, the ranges (average) of errors of all the compositional classes are 0.2 - 2.7 vol% (0.8 vol%) for olivine, 0.2 - 2.4 vol% (1.1 vol%) for LCP, 0.2 - 4.8 vol% (1.0 vol%) for HCP, 1.2 - 8.7 vol% (2.7 vol%) for plagioclase and 2.2 - 13.2 (5.1) for Mg#. When clean Mg# is 90, the error ranges (average) are 0.6 - 5.2 vol% (2.3 vol%) for olivine, 0.6 - 4.8 vol% (2.6 vol%) for LCP, 0.2 - 6.2 vol% (2.0 vol%) for HCP, 2.0 - 12.3 vol% (5.8 vol%) for plagioclase and 1.8 - 15.5 (7.3) for Mg#. It can be seen that the error varies with Mg#. When Mg# is low, the spectral absorptions are more significant, making it easier to distinguish mineral components from the mixture, thus resulting in smaller errors. Higher errors in estimating Mg# of pure anorthosites (plagioclase > 90 vol.%) are due to spectral features getting too weak for our model to accurately estimate the Mg#. The error for plagioclase is higher than

mafic minerals from this test, because plagioclase has a much broader range in abundance than mafic minerals within lunar rocks.

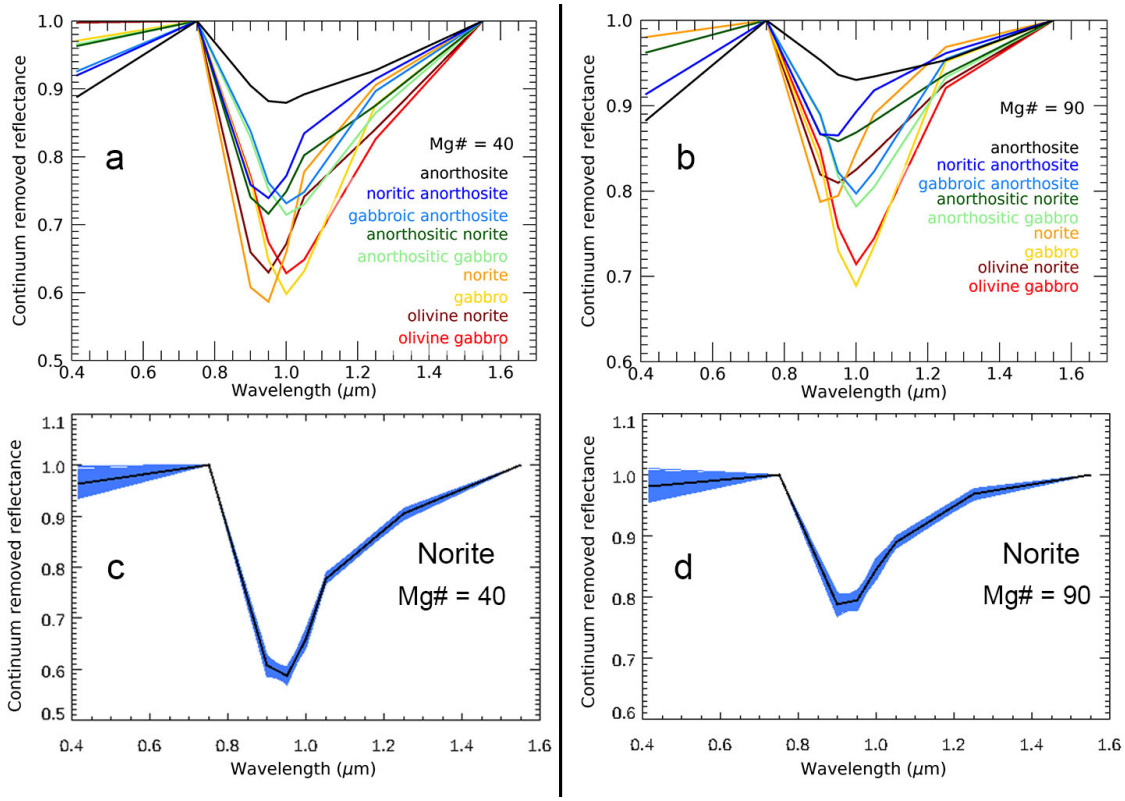

Figure 3.19: Input spectra of nine compositional classes with (a) Mg# = 40 and (b) Mg# = 90. Noisy (blue) and input (black) spectra comparison for norite with (c) Mg# = 40 and (d) Mg# = 90.

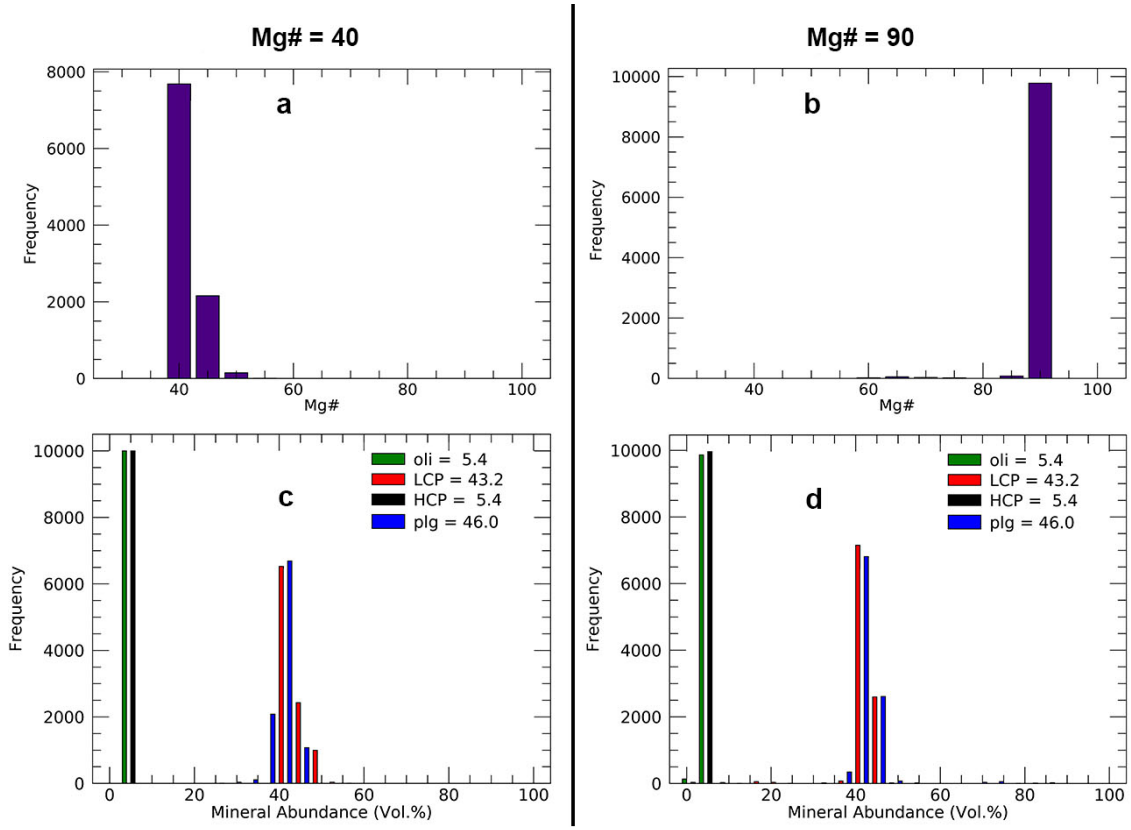

Figure 3.20: Histograms of the (a, b) Mg# and (c, d) four major minerals derived by matching noisy norite spectra to the spectral mixing library. The input mineral mode is labeled in (c) and (d), and the input Mg# is 40 for the left column and 90 for the right column. Peak values of noisy results are consistent with the input Mg# and mineral mode.

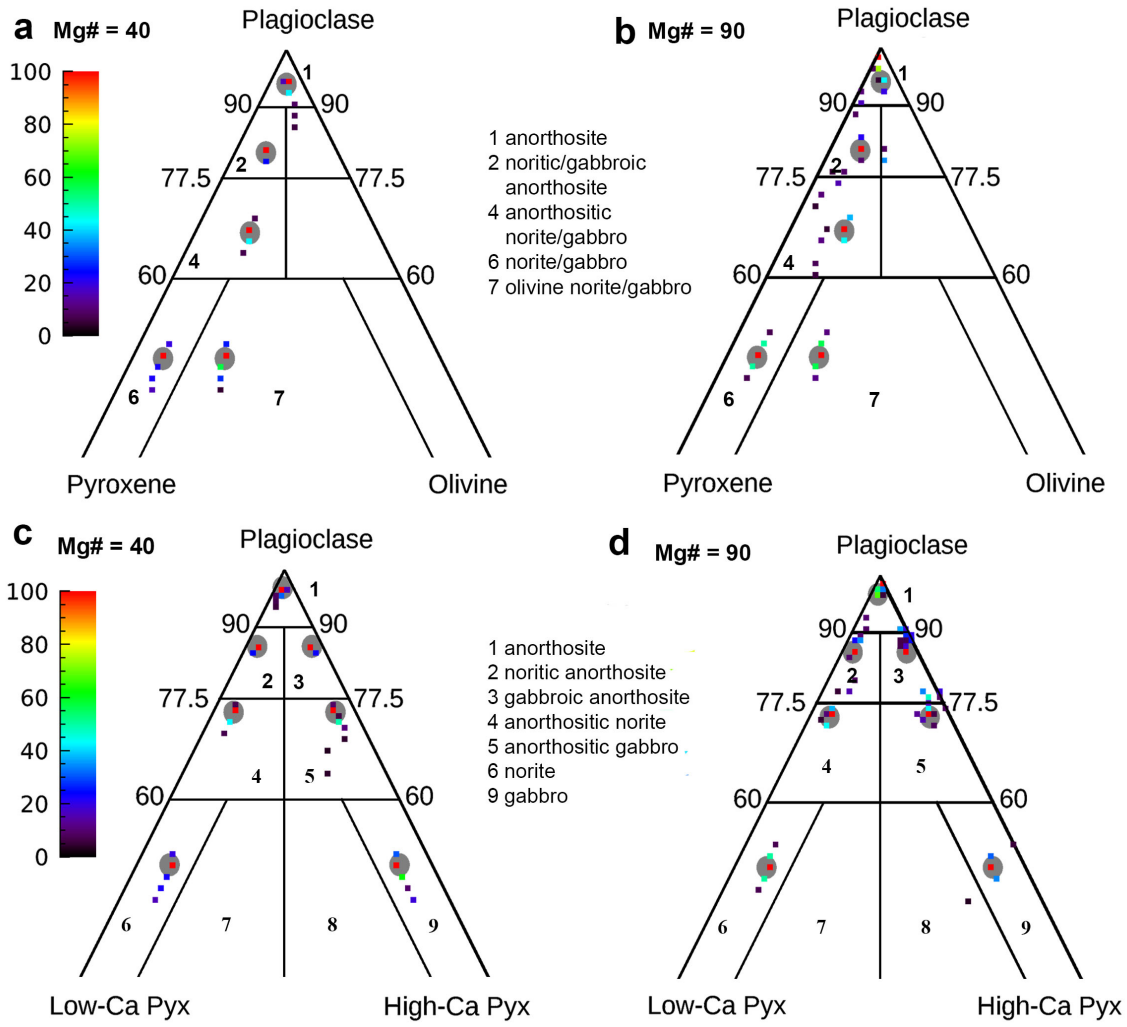

Figure 3.21: Normalized histogram of noisy mineral abundances overplotted on the mineralogical classification diagram (Stöffler et al., 1980). The gray dots are the input mineral modes for each class. The left column shows results for Mg# = 40, and right column shows results for Mg# = 90. Most of the peak concentrations of the noisy minerals are consistent with the input ones.

Table 3.8: Mineral modes (in vol%) of nine compositional classes for noise test. Clean mineral abundances are the values before adding noise, peak mineral abundances are from the statistical results of mineral modes and Mg# derived from noisy spectra, and the standard deviation of the noisy minerals are listed in the σ column.

	Olivine			LCP			HCP			Plagioclase			Mg#		
	clean	peak	σ	clean	peak	σ	clean	peak	σ	clean	peak	σ	clean	peak	σ
class name	Mg# = 40														
Anorthosite	3.0	2.8	1.7	1.8	1.2	1.3	1.2	1.0	0.3	94.0	94.0	2.9	40.0	40.0	13.2
Noritic anorthosite	5.4	5.2	0.4	10.8	10.6	1.2	1.8	1.6	0.3	82.0	82.0	1.6	40.0	40.0	3.2
Gabbroic anorthosite	5.4	5.2	2.7	1.8	1.8	2.4	10.8	10.0	4.8	82.0	82.0	8.7	40.0	40.0	12.3
Anorthositic norite	9.6	9.0	0.4	19.2	19.0	1.0	3.2	3.0	0.2	68.0	68.0	1.5	40.0	40.0	3.0
Anorthositic gabbro	9.6	9.0	0.4	3.2	3.0	0.4	19.2	19.0	0.7	68.0	68.0	1.2	40.0	40.0	3.9
Norite	5.4	5.2	0.3	43.2	42.6	2.0	5.4	5.2	0.3	46.0	46.0	2.5	40.0	40.0	2.3
Gabbro	5.4	5.2	0.2	5.4	5.2	0.2	43.2	42.6	1.7	46.0	46.0	2.1	40.0	40.0	3.2
Olivine norite	16.2	15.6	0.6	32.4	32.0	1.2	5.4	5.0	0.2	46.0	46.0	1.9	40.0	40.0	2.4
Olivine gabbro	16.2	15.6	0.4	5.4	5.0	0.3	32.4	32.0	0.9	46.0	46.0	1.4	40.0	40.0	2.2
	Mg# = 90														
Anorthosite	3.0	0.0	1.5	1.8	0.2	0.6	1.2	1.0	0.2	94.0	98.0	2.0	90.0	90.0	15.5
Noritic anorthosite	5.4	5.0	1.9	10.8	10.2	3.7	1.8	1.0	0.3	82.0	82.0	4.6	90.0	90.0	5.7
Gabbroic anorthosite	5.4	5.0	2.2	1.8	1.0	1.4	10.8	10.0	3.7	82.0	82.0	5.4	90.0	90.0	6.8
Anorthositic norite	9.6	9.2	1.8	19.2	19.0	4.8	3.2	3.0	0.7	68.0	68.0	6.0	90.0	90.0	4.5
Anorthositic gabbro	9.6	9.0	3.1	3.2	3.0	1.5	19.2	19.0	4.5	68.0	68.0	7.8	90.0	90.0	12.7
Norite	5.4	5.0	0.6	43.2	42.6	3.4	5.4	5.2	0.3	46.0	46.0	4.3	90.0	90.0	2.8
Gabbro	5.4	5.0	0.8	5.4	5.0	1.8	43.2	43.0	1.9	46.0	46.0	3.1	90.0	90.0	1.8
Olivine norite	16.2	15.6	3.1	32.4	31.8	4.0	5.4	5.0	0.7	46.0	46.0	6.7	90.0	90.0	3.1
Olivine gabbro	16.2	16.0	5.2	5.4	5.0	2.2	32.4	31.6	6.2	46.0	46.0	12.3	90.0	90.0	12.6

3.5.3 Mineral modes and Mg# of LSCC lunar soils

LSCC 10-20 μm sized lunar soils were also used to test the ability of our model in estimating mineral modes and Mg# from spectra. To simulate the spectral reddening and darkening due to space weathering, a series of nano-phased Fe varying from 0.0005 wt.% to 0.007 wt.% were added into all library spectra (Hapke, 2001).

The modeled and measured mineral modes for 19 lunar soils are listed in Table 3.9 and overplotted in Figure 3.22. With the bulk correlation coefficient R = 0.97 and standard deviation of linear regression being 6 vol%, the modeled minerals show a linear correlation with the measured ones. The correlation coefficients between modeled and measured olivine, LCP, HCP and plagioclase are 0.75, 0.85, 0.90 and 0.93, respectively, suggesting a linear correlation is also valid for each single mineral. The standard deviations are <5 vol% for mafics and 6.5 vol% for plagioclase, which is consistent with the error range estimated from the sensitivity test. In addition, the range of mineral content can affect their correlation coefficients and error. Plagioclase has a large range in abundance, which results in a larger range in standard deviation.

Table 3.9 lists measured and modeled Mg# for LSCC soils, where measured Mg# is from the fused bead chemistry of LSCC lunar soils having 10 - 20 μm grain sizes reported by Cahill et al. (2010). Because the range of Mg# (50-70) in the LSCC data is small and comparable to the sensitivity ($\pm$10) of our algorithm, we do not expect to see a strong correlation between our derived Mg# and those measured in LSCC. The RMS between the two results is about 7, which is consistent with the noise test error.

3.5.4 Global Mg# map

To validate our model in estimating Mg#, we present a global Mg# map (Figure 3.23a) produced using the radiative transfer model and M^3 data resampled to one degree latitude and longitude resolution (Li and Milliken, 2016, 2017). From this Mg# map, it can be observed that Mg# in the farside highlands can reach up to 90 and is higher than Mg# of most of the mare. Low Mg# values are concentrated within the mare, especially in the

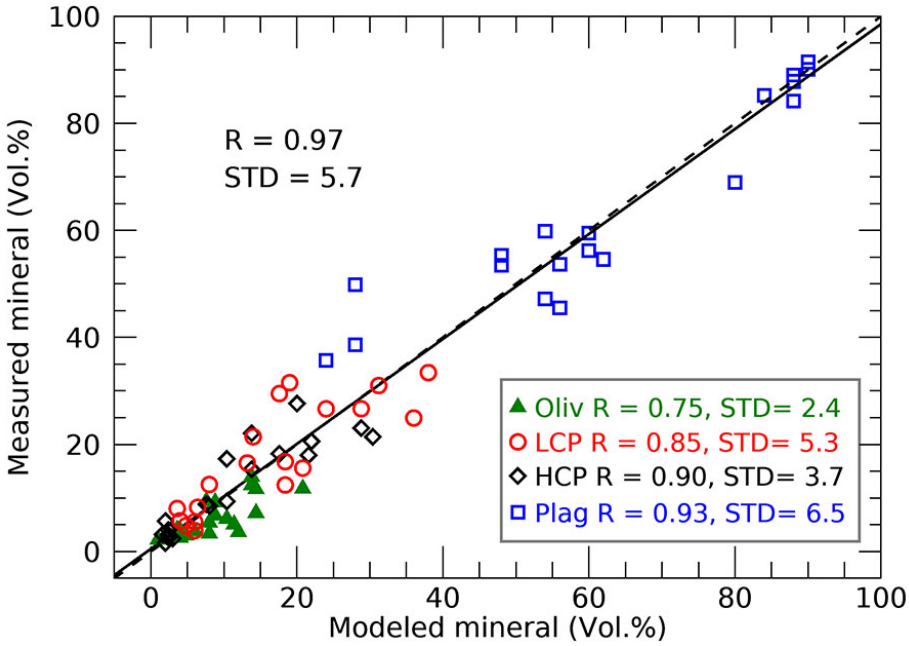

Figure 3.22: Modeled minerals compared with those measured by LSCC for nineteen lunar soils. The dashed line is the 1:1 ratio, and the solid line is the fitting line for all the minerals. The correlation coefficient (R) and standard deviation for all the minerals are 0.97 and 5.7 vol.%. The correlation coefficient and standard deviation for each mineral are also labeled in the plot.

western Oceanus Procellarum and northern Imbrium, which shows high KREEP abundances from the Lunar Prospector gamma-ray spectrometer (LP-GRS) results (Lawrence et al., 1998). Mg# in the South Pole-Aitken is slightly lower than the farside highlands and higher than the mare.

We also compare the values of our Mg# map to those derived using the elemental maps from Lunar Prospector gamma-ray spectrometer (Prettyman et al., 2006). The histograms of the two results are overplotted in Figure 3.23b. Our Mg# map is consistent with the LP-GRS result: the peak Mg# from this work is 70, compared to 68 of LP-GRS; the global averaged Mg# from this work is 65, compared to 68 from LP-GRS. When classifying lunar highlands using FeO $<$ 8wt.% and nearside mare using FeO $>$13 wt.% (Prettyman et al., 2006), the average Mg# is 59.4 for lunar highlands and 50.8 for nearside mare from our Mg# map.

Table 3.9: LSCC measured compared to Hapke modeled mineral mode (vol%) and Mg# of nineteen lunar soils.

	Measured					Modeled				
Soil No.	Olivine	LCP	HCP	Plag	Mg#	Olivine	LCP	HCP	Plag	Mg#
10084-78	3.6	12.5	27.6	56.3	49.4	12.0	8.0	20.0	60.0	55.0
12001-56	11.7	26.7	23.1	38.6	53.1	14.4	28.8	28.8	28.0	60.0
12030-14	9.4	33.4	21.4	35.7	50.8	7.6	38.0	30.4	24.0	55.0
14141-5.7	3.9	21.4	5.7	69.0	63.3	4.0	14.0	2.0	80.0	50.0
14163-57	6.1	31.0	9.4	53.5	63.0	10.4	31.2	10.4	48.0	65.0
14259-85	5.4	26.6	8.5	59.5	63.6	8.0	24.0	8.0	60.0	60.0
14260-72	5.1	31.5	8.8	54.6	63.5	11.4	19.0	7.6	62.0	55.0
15041-94	6.7	29.5	18.3	45.5	57.4	8.8	17.6	17.6	56.0	50.0
15071-52	7.2	24.9	18.0	49.9	56.3	14.4	36.0	21.6	28.0	70.0
61141-56	3.4	8.2	3.2	85.2	70.5	8.0	6.4	1.6	84.0	70.0
61221-9.2	3.0	4.8	3.1	89.1	67.9	4.8	4.8	2.4	88.0	60.0
62231-91	3.8	8.0	4.0	84.2	70.3	6.0	3.6	2.4	88.0	65.0
64801-82	2.6	5.7	1.6	90.1	69.9	4.0	4.0	2.0	90.0	70.0
67461-25	2.2	3.9	2.4	91.5	65.1	1.0	6.0	3.0	90.0	50.0
67481-31	4.1	5.5	2.5	87.8	66.9	3.6	6.0	2.4	88.0	60.0
70181-47	12.4	12.4	15.4	59.8	53.7	13.8	18.4	13.8	54.0	65.0
71061-14	14.0	16.8	22.0	47.2	51.7	13.8	18.4	13.8	54.0	50.0
71501-35	9.2	16.5	20.6	53.7	51.1	8.8	13.2	22.0	56.0	50.0
79221-81	11.8	15.6	17.3	55.4	55.5	20.8	20.8	10.4	48.0	70.0

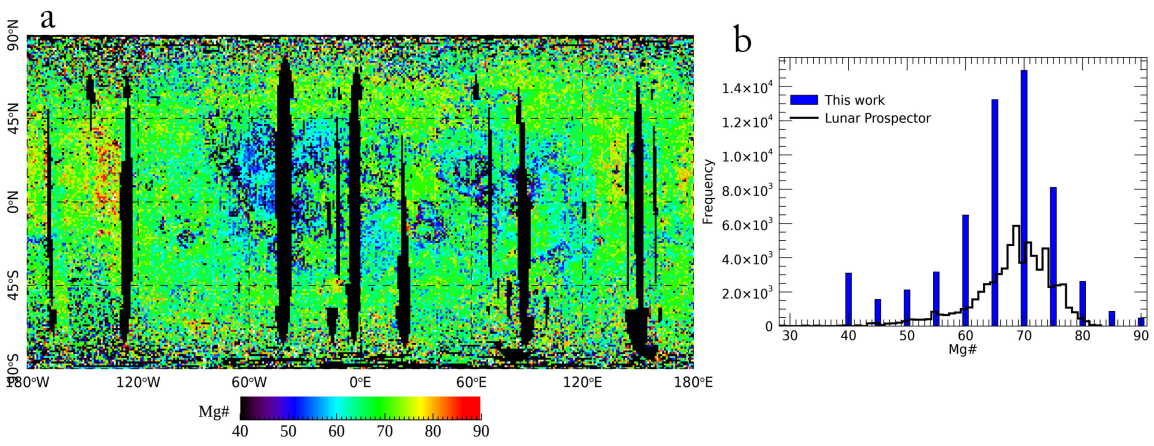

Figure 3.23: (a) Global Mg# map derived from radiative transfer modeling and Moon Mineralogy Mapper images (Li and Milliken, 2016, 2017) (resolution is one degree/pixel). (b) Histograms of Mg# map from this work and Lunar Prospector gamma-ray spectrometer (Prettyman et al., 2006).

3.6 Conclusions

In conclusion, we applied radiative transfer equations that include porosity and opposition effect in replicating the optical behaviors of lunar major minerals. With these equations, we provide a new set of optical constants for olivine, orthopyroxene and clinopyroxene. The forward modeling has shown that these optical constants can reproduce reflectance spectra for both powdered pure minerals and LSCC lunar soils, and the spectral characteristics are consistent with those measured in the laboratory.

For the inverse modeling, we built a spectral mixing library and developed a spectral matching algorithm. We applied a sensitivity test by adding noises comparable to that of Kaguya Multiband Imager data, and the accuracy in estimating mineral abundances is less than 3 vol% for olivine, low-Ca pyroxene and high-Ca pyroxene, and less than 6 vol% for plagioclase; the accuracy in estimating Mg# is less than 10.

Mineral abundances derived from our model are linearly correlated with those measured from LSCC lunar soils in the laboratory. A global Mg# map is presented, and the peak and mean Mg# values are 70 and 65. Mg# is 59.4 for typical lunar highlands and 50.8 for lunar nearside mare. Our Mg# map is consistent with that derived from the Lunar Prospector gamma-ray spectrometer.

Chapter 4

Multispectral Imaging and Hyperspectral Scanning of the First Dissection of Core 73002: Preliminary Results

4.1 Introduction

The double drive tube 73001/2 was sampled at Station 3 during the extravehicular activity (EVA) 2 of Apollo 17 mission, located near the rim of Lara crater, on the Light Mantle southwest of Taurus-Littrow valley (Butler, 1973) (Figure 4.1). The Light Mantle is a landslide from South Massif, and samples collected there show that the major compositional classes range from anorthositic norite to norite, depending on the quantity of valley basalts that are mixed with the landslide (Sun et al., 2018; Taylor et al., 2019).

The double drive tube is 60 cm in length and 4 cm in diameter (Zeigler et al., 2020). Core 73002 is the upper segment, and it sampled 23 cm in depth. X-ray scans show that core 73002 mainly consists of soils, but several clasts can also be observed, and these clasts tend to concentrate at the lower part of the core (Duke and Nagle, 1976; Zeigler et al., 2020). However, this distribution may not reveal the local profile of regolith but instead result from rocks wedging within the core, since nearby trenches show no regolith stratigraphy profile (Duke and Nagle, 1976). This feature suggests core 73002 may be sampling the ejecta of Lara crater (Duke and Nagle, 1976).

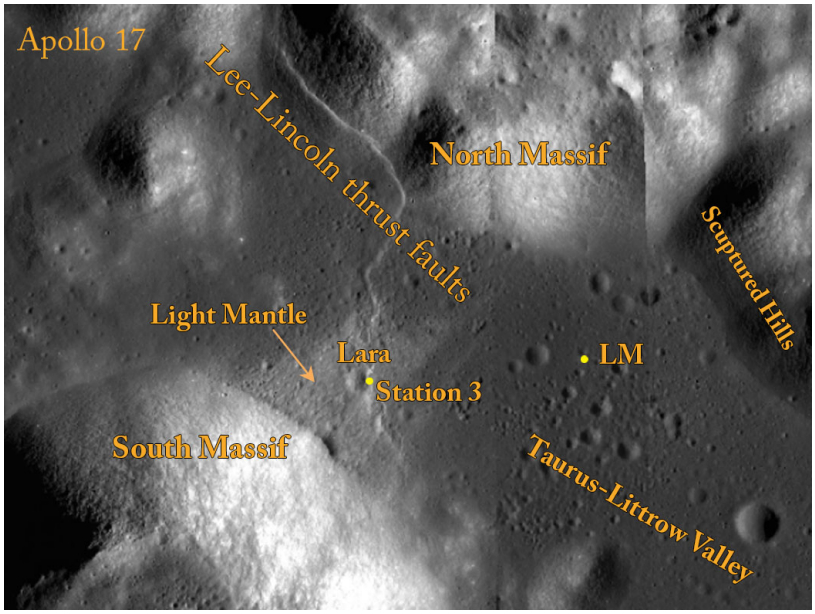

Figure 4.1: Geologic context of the sampling location of the double drive tube 73001/2, which was sampled at Station 3.

In December 2019, the Apollo Next Generation Sample Analysis (ANGSA) team opened core 73002 at the NASA Johnson Space Center, beginning to examine the first of the two pristine core samples. As part of the preliminary examination, spectral imaging and hyperspectral scans of the cores are being carried out by the University of Hawai'i, supported by the CAAAS (Consortium for the Advanced Analysis of Apollo Samples) team of ANGSA and the curatorial facility. In this chapter, I present some preliminary results of multiband imaging and hyperspectral profiles obtained during the first dissection of core 73002.

4.2 Methods

To establish measurement methodologies, we carried out preliminary multiband spectral imaging and hyperspectral measurements during dissection of the first layer of the core using existing instrumentation. The core is in a glass walled glove box purged with dry nitrogen. The top of the glove box is also glass, which allows spectral measurements in the range of 500-2500 nm, the spectral transmission range of borosilicate glass. The schematic diagram

of the spectroscopy system is shown in Figure 4.2. All the instruments are installed on the frame on top of the glove box, and the light source is shared by the multiband imaging system and hyper-spectrometer. Both the multiband images and hyperspectral data were acquired a 15° incidence angle, 10° emission angle, and a 25° phase angle in plane. Spectral data were then calibrated relative to a Teflon standard that is cross calibrated to the spectral reflectance standard Spectralon.

The multiband imaging camera covers six wavelengths: 415 nm, 570 nm, 750 nm, 900 nm, 950 nm, 990 nm (Table 4.1), sharing some of the bands used by the Clementine UVVIS camera, the Lunar Reconnaissance Orbiter wide angle camera and the KAGUYA Multiband Imager (MI). The multiband imaging system images the core at 60 μm/pixel spatial resolution, and the field of view (FOV) is about 47 mm × 36 mm. However, the available spectral illuminator did not cover the entire core width, and the illuminated area was a roughly 30 mm-diameter circle within the image frame (shown in Figure 4.3). The detected FOV of preliminary measured images is 30 mm × 30 mm.

The hyperspectral data is acquired by an Analytical Spectral Devices (ASD-FR) spectrometer, with its wavelengths covering 500-2500 nm at 10 nm spectral resolution, substantially overlapping remote sensing spectral data from M^3 from Chandrayaan-1, the Spectral Profiler (SP) on board Kaguya, and the large lunar soil spectral datasets measured at RELAB. During the preliminary measurement, spectra of 17 spots were measured at 10 mm sampling distance along the center of the core, and ten spectra were collected at each spot. To suppress possible artificial effects and increase the signal to noise ratio, we averaged ten reflectance spectra for each spot and acquired a profile consisting of 17 spectra along the core. The hyperspectral data are not usable beyond 1700 nm due to low signal to noise ratio from a combination of low spectral irradiance from the illuminator and low sensitivity of the spectrometer at longer wavelengths, thus the wavelength range we used for analysis is 500-1700 nm.

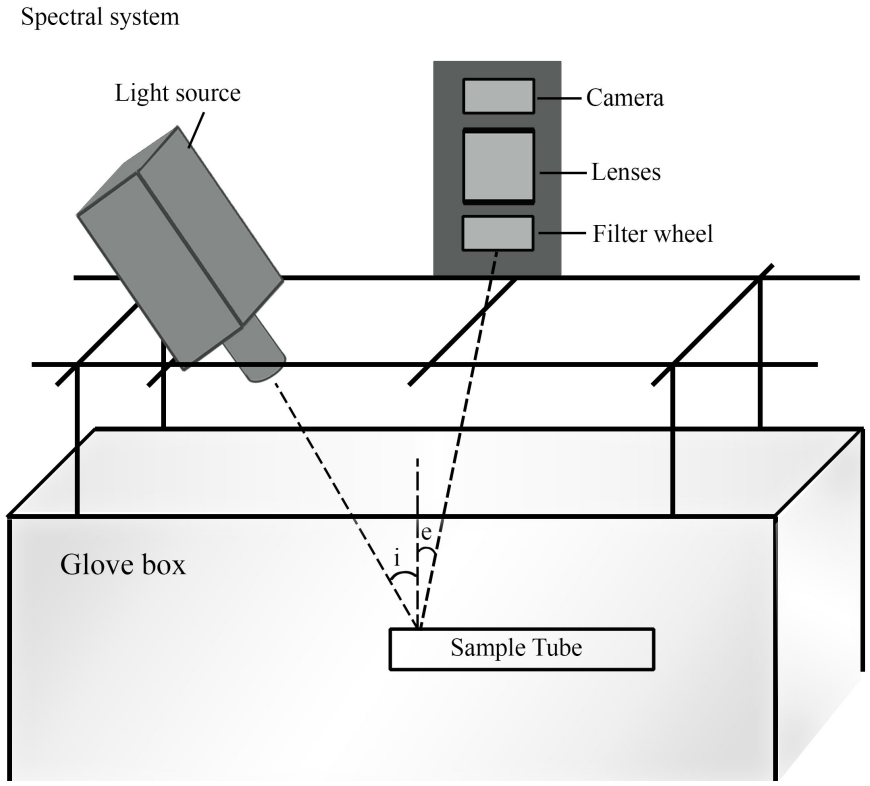

Figure 4.2: Spectral measurement system, consisting of light source and spectrometer, located on a frame above the glove box, size not to scale. The multiband imaging set includes light source, camera, lenses and filter wheel. For the hyperspectral measurements, we replaced the multiband set with an ASD probing fiber.

Table 4.1: Instrumental parameters of the multiband imaging and hyperspectral system during preliminary measurements.

Parameters	Multiband Imaging System	Hyperspectral System
Wavelengths (nm)	415, 570, 750, 900, 950, 990	500 - 1700
Viewing Geometry	i = 15°, e =10°	i = 15°, e =10°
Spectral Resolution	(FWHM) 10 nm	10 nm
Spatial Resolution	60 μm/pixel	10 mm/pixel
FOV/Sampling Intervals	30 mm × 30 mm	10 mm
Coverage	about 3/4 of the core (Figure 4.3)	one profile along center (Figure 4.5a)

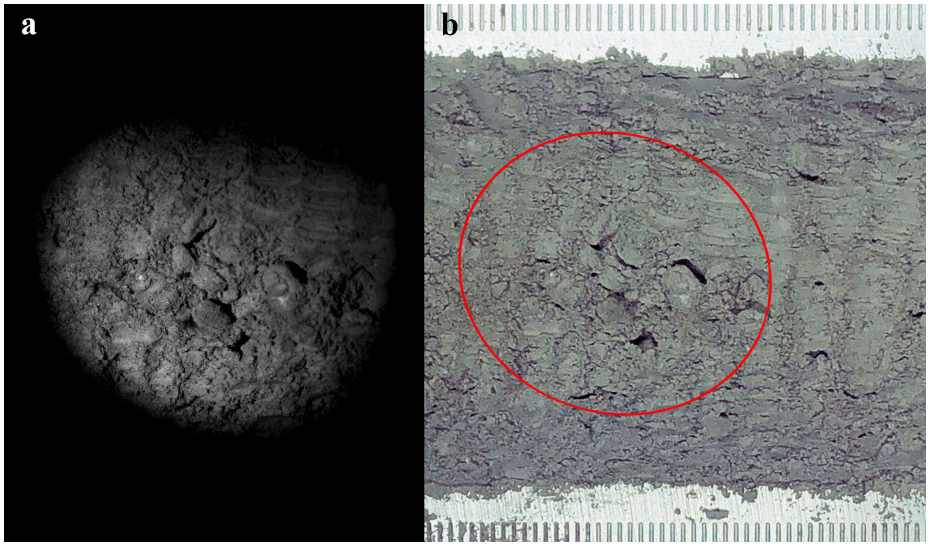

Figure 4.3: (a) One image frame at 570 nm of the multiband imaging scans, with the same area circled in (b), which is a zoom in photograph of the core. More than 75% of the width of the core is illuminated and captured by the multiband imager.

4.3 Results and discussion

4.3.1 Geologic context of Station 3

FeO and OMAT (optical maturity, fresh materials have higher OMAT values) distributions for Taurus-Littrow valley were mapped using Kaguya MI data (Lemelin et al., 2015), shown in Figure 4.4. Station 3 is located on the Light Mantle, and the FeO content is about 8.5 wt.%, which is close to the Light Mantle and South Massif materials. The OMAT at Station 3 is around 0.2, which is slightly higher than surrounding areas since it is situated on the ejecta of a young crater.

Trench soil samples collected from Station 3 include 73211, 73221, 73261 and 73281, which can be used as reference samples for core 73002. The mineralogy, compositions and Is/FeO are listed in Table 4.2. The mineralogy is similar among these soils, with average plagioclase abundance being 68 vol%. Mg# of soils varies within a narrow range (64-70), and the average is around 67. All the soils are moderate in FeO and low in TiO_2 contents; the average abundance for FeO and TiO_2 are 8.8 wt.% and 1.8 wt.%. Is/FeO measured by

Morris (1978b) with FMR suggests most of the Station 3 soils are submature (Is/FeO = 34-45), and 73241 is the only immature soil (Is/FeO = 18).

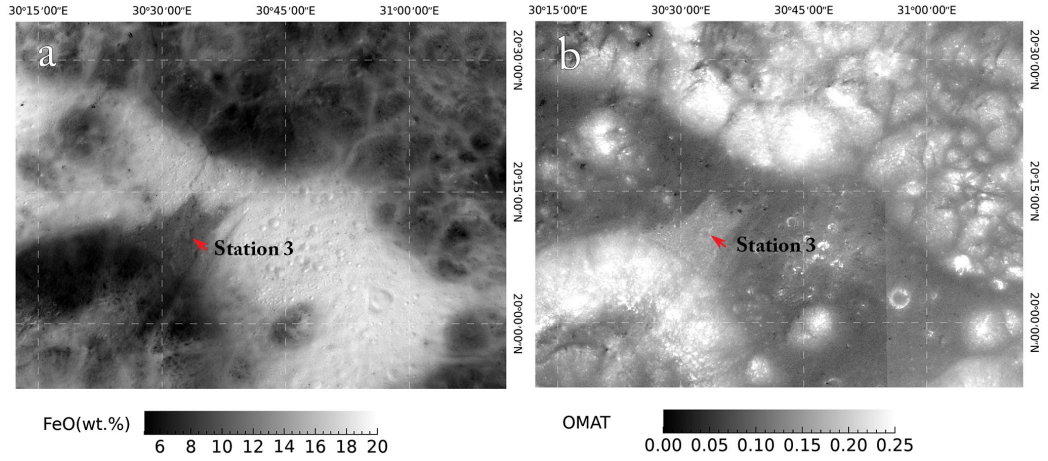

Figure 4.4: (a) FeO and (b) OMAT maps of the Apollo 17 landing area derived from Kaguya Multiband Imager data (Lemelin et al., 2015). Red arrows indicate location of Station 3.

Table 4.2: Compositional information of soils collected at Station 3.

Sample	Oliv[a]	LCP[a]	HCP[a]	Plag[a]	Mg#[b]	FeO[b]	TiO_2[b]	Is/FeO[c]	sample info[d]
73211	12.7	13.3	5.4	68.5	-	8.93[e]	-	39	Soils abraded off rocks
73221	12.1	16.3	5.4	66.2	64.1	8.85	1.86	43	Trench soils, surface
73241	11.6	16.6	5.0	66.8	69.8	8.45	1.73	18	Trench soils, surface
73261	12.3	14.9	6.4	66.4	68.5	8.86	1.9	45	Trench soils, subsurface
73281	12.8	6.9	9.0	71.4	66.5	8.82	1.76	34	Trench soils, subsurface

[a] Mineral mode (in vol%) measured by Taylor et al. (2019) with XRD
[b] FeO and TiO_2 contents (in wt.%) measured by Rose et al. (1974) with microchemical techniques
[c] Is/FeO measured by Morris (1978b)
[d] Sampling information from Butler (1973)
[e] FeO content (in wt.%) measured by Korotev and Kremser (1992) with instrumental neutron activation analysis (INAA)

4.3.2 Multiband imaging scans

The multiband images were measured in December of 2019, during the first dissection of core 73002. The original sampling depth of core 73002 is about 23 cm in length, and it is compressed to $\sim$ 18.5 cm after being extruded from the tube (Zeigler et al., 2020). We

took 72 images along the core in 6 spectral bands, and made a mosaic shown in Figure 4.5. Reflectance at 570 nm show a systematic darkening effect from bottom to top of the core, which we attribute to space weathering (Figure 4.5b). We also produced a false color image (Figure 4.5c) using similar bands to Clementine UVVIS false color images, and the three channels are red=750 nm/415 nm, green=750 nm/950 nm, blue=415 nm/750 nm. The red channel is sensitive to the maturity of soils, green channel is sensitive to the abundance of FeO, and blue channel is sensitive to ilmenite abundances. From Figure 4.5c, a systematic reddening trend from bottom to top can be observed, suggesting an increase in maturity, and the light shade in blue shows low ilmenite content of soils within the core.

We used a 15° incidence angle when acquiring the images, resulting in frequent shadows. To suppress the influence of shadows, we averaged the reflectance across width indicated by the red frame shown in Figure 4.5b, and plotted the ratio of 950 nm and 750 nm versus 750 nm reflectance in Figure 4.6a. On one hand, variation in the FeO direction is small, suggesting a relatively homogeneous composition within the core. On the other hand, an obvious darkening and reddening trend can be observed in the OMAT axis, indicating a gradient in maturity.

To quantify the FeO and OMAT values for the core, a dark and red end member is located at $x_{0Fe} = 0.08$, $y_{0Fe} = 1.15$ in Figure 4.6a, and equation (4.1) is used to calculate the FeO content of the core (Lucey et al., 2000a). The histogram of FeO is shown in Figure 4.7b, and the peak FeO value is 9 wt.%, consistent with those measured from the trench soils (Table 4.2). Standard deviation of FeO distribution is 1.0 wt.%, suggesting a uniform composition within this core, reinforcing the idea that no stratigraphy should exist within the upper 30 cm of local regolith.

$$FeO(wt.\%) = 19 \times [-arctan(\frac{R_{950}/R_{750} - y_{0Fe}}{R_{750} - x_{0Fe}})] \tag{4.1}$$

OMAT is calculated with the Euclidean distance to the end member on the ratio plot (Figure 4.7)(Lucey et al., 2000a). The OMAT values of the core are shown in Figure 4.7a, and OMAT increases from the surface to the bottom of the core, showing a decreasing

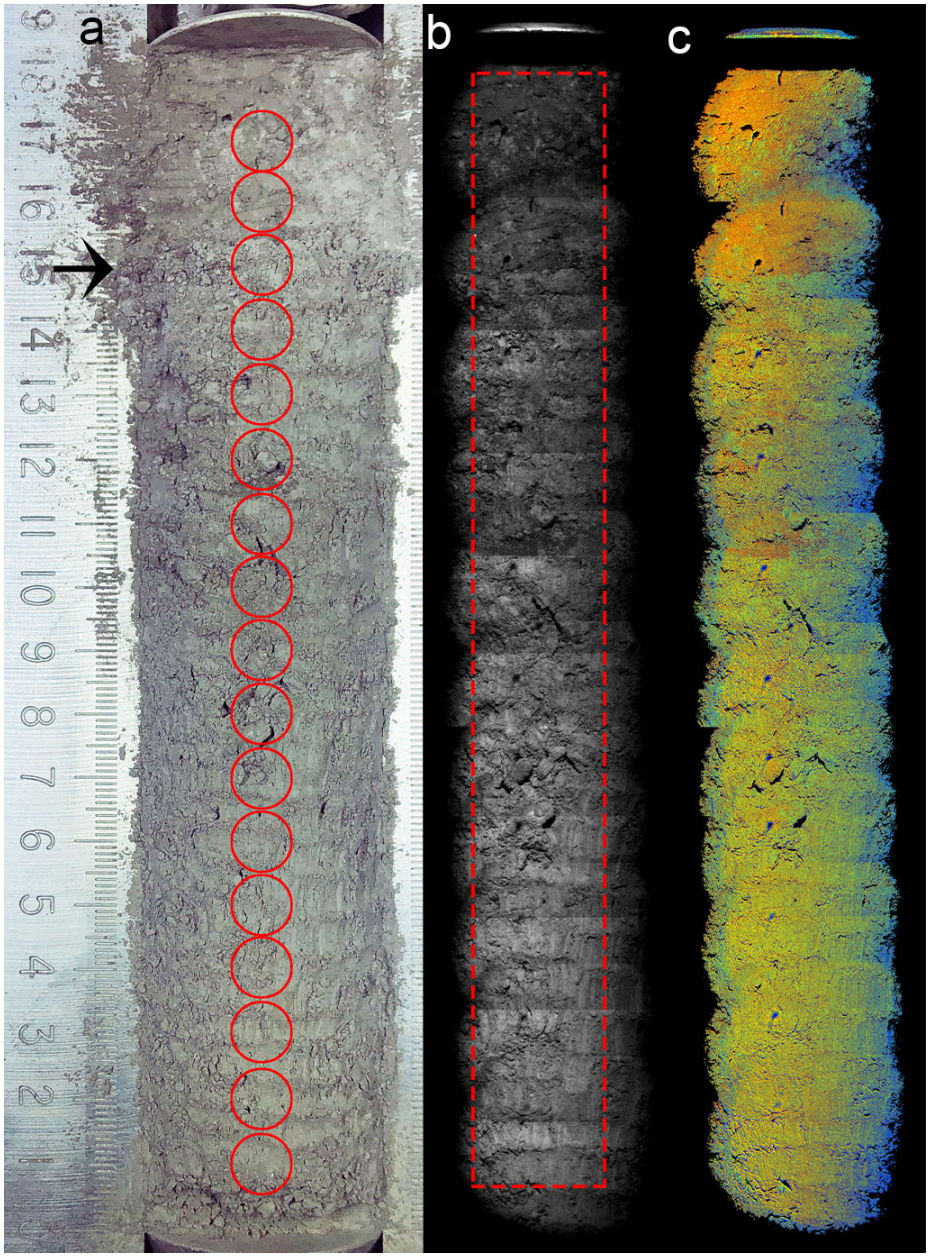

Figure 4.5: Core 73002 images during the first dissection. The upper end is closer to the surface. (a) Photograph of the core taken by Dr. Paul Lucey. The scale is shown on the left, the arrow indicates dissection progress when the images were taken, red circles are hyperspectral profile footprints. (b) Core mosaic in 570 nm reflectance. The red frame shows the area we used to calculate FeO and OMAT in the following text. (c) False colored image of the core mosaic, red=750 nm/415 nm, green=750 nm/950 nm, blue=415 nm/750 nm.

degree of space weathering with depth. The spikes in the OMAT values are the result of illumination and/or topography of the core rather than regolith reworking. Surface soils listed in Table 4.2 are mostly submature based on their Is/FeO values, implying that the maturity of core soils may range from immature (bottom) to submature (surface), corresponding to a 60% increase in OMAT from bottom to top of the core.

To estimate the abundances of TiO_2, we plotted the ratio of 415 nm/750 nm versus the reflectance at 750 nm in Figure 4.6b. We adopted the TiO_2 origin ($x_{0Ti} = 0.0$, $y_{0Ti} = 0.42$) from Lucey et al. (2000a). The used equation (4.2) to estimate the TiO_2 abundances, and the histogram of TiO_2 abundance of the core is shown in Figure 4.7c. The peak value is near 1.8 wt.%, and the standard deviation is $\sim$ 0.5 wt.%.

$$TiO_2(wt.\%) = 3.708 \times [\, arctan(\frac{R_{950}/R_{750} - y_{0Ti}}{R_{750} - x_{0Ti}})]^{5.979} + 1.5 \tag{4.2}$$

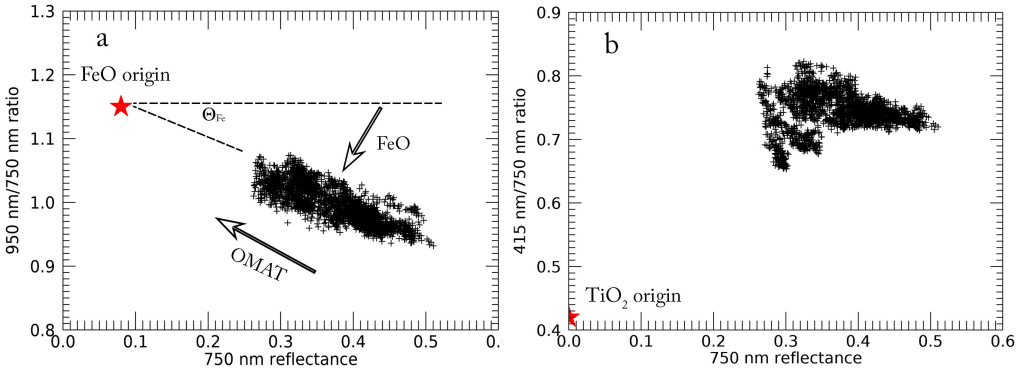

Figure 4.6: (a) 950 nm/750 nm ratio versus 750 nm reflectance along the core, (b) 415 nm/750 nm ratio versus 750 nm reflectance along the core. To avoid the influence of shadows, we averaged reflectance by rows within the frame shown in Figure 4.5b.

To present a comprehensive view of the core, we mapped the distribution of OMAT, FeO and TiO_2 of the first dissection of core 73002 in Figure 4.8. Values near shadows may have larger error; however, an increasing trend of OMAT from surface to bottom of the core is obvious, and FeO and TiO_2 have relatively homogeneous distributions.

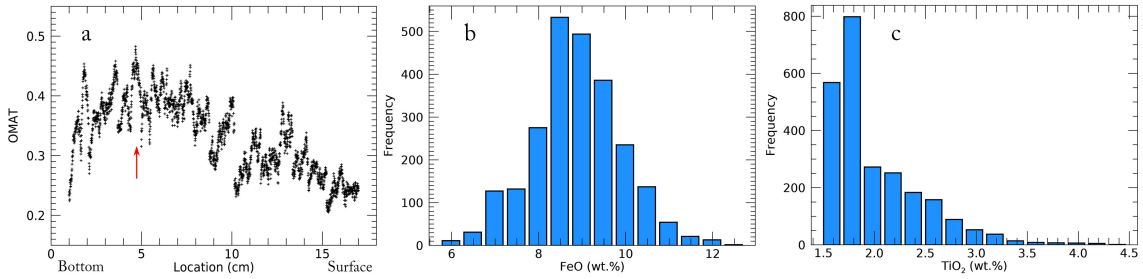

Figure 4.7: (a) OMAT values along the core; the location corresponds to the scale in Figure 4.5. Red arrow points to the regolith reworking depth.(b) Histogram of FeO distribution along the core. (c) Histogram of TiO_2 abundances along the core. All values are calculated with row-averaged reflectance within the frame shown in Figure 4.5b.

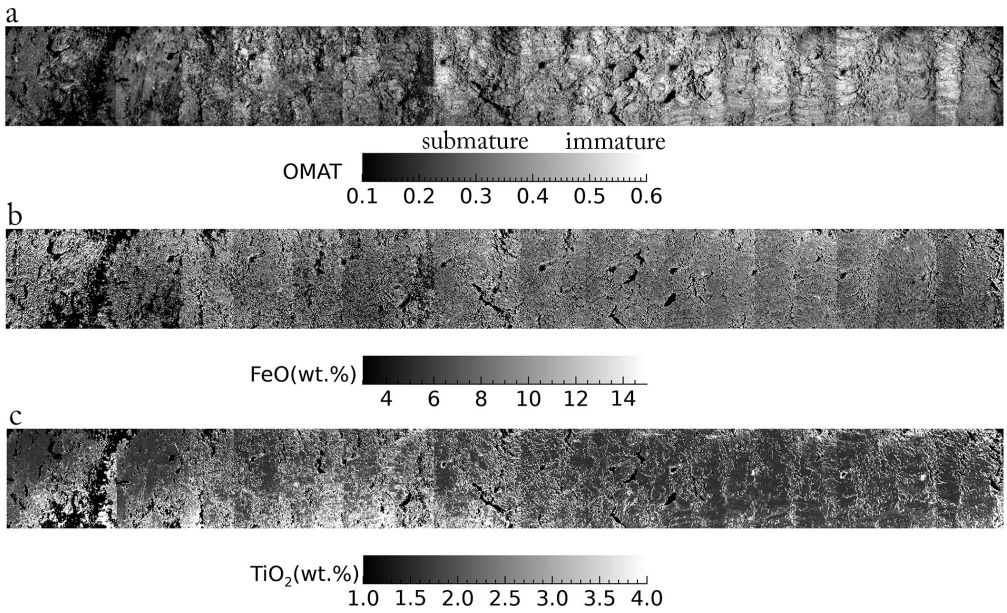

Figure 4.8: (a) OMAT, (b) FeO and (c) TiO_2 maps of core 73002. Mapping area is confined to the red frame in Figure 4.5.

The homogeneous compositional distribution and gradient in OMAT within core 73002 suggest that contamination from lateral mixing is limited. Therefore, vertical exchange of soils dominates the regolith reworking progress. The red arrow in Figure 4.7a refers to the possible regolith reworking depth, which is located at 2/3 depth of the core, whereas the original reworking depth within the core should be around 14 cm.

Morris (1978a) derived the relationship between in situ regolith reworking depth and time by summarizing data from several Apollo cores:

$$D_R = 2.2(t)^{0.45}, \tag{4.3}$$

where D_R is reworking depth in centimeters and t is time in million years. Based on this equation, it takes about 61 million years to produce a 14 cm regolith reworking depth. Phinney et al. (1975) reported the cosmic ray exposure age is 190±20 million years for rock 73235 based on ^{40}Ar-Ca dating, and the exposure age of rock 73275 is 139±5 million years from ^{81}Kr-Kr dating (Arvidson et al., 1976). The regolith reworking time of the core is consistent with the cosmic ray exposure time of rocks collected at the same sampling station, implying the ejecta materials may have experienced similar space weathering time, and none or little significant disturbances from lateral mixing of regolith occurred.

The space weathering time of surface soils is close to the reworking time of the top 14 cm regolith, implying that the surface material may be as fresh as the lower soils within the core when it was exposed by the crater forming impact. Comparing to the fresh materials within the core, the OMAT of surface soils increased about 60% during 61 million years.

4.3.3 Hyperspectral profile

Footprints of hyperspectral profile are shown in Figure 4.5a, and seventeen spots sized at 10 mm diameter were measured. The hyperspectral reflectance is shown in Figure 4.9, and we use colors to show different locations of spectra. Note that these locations refer to the scale next to the core in Figure 4.5a. Reflectance spectra show a systematic darkening from bottom to top of the core (Figure 4.9a), and a systematic reddening in spectral slope is obvious when reflectance spectra are normalized to 750 nm (Figure 4.9b). These observations indicate an increasing maturity from bottom to top of core, which is consistent with the multiband imaging results. There is no obvious weakening of absorption

band depths near one micron; this might due to the high anorthositic composition of the soils or the influence of heterogeneous grain size variation within the core.

Sun et al. (2019) developed a mineral mode and chemistry unmixing model with radiative transfer theory, and by applying this model to the seventeen ASD spectra, we derived the mineral mode of olivine, low-Ca pyroxene (LCP), high-Ca pyroxene (HCP) and plagioclase, as well as Mg# of the core. We plot the mineral modes derived by Sun et al.'s model and those of Station 3 soils measured by XRD (Table 4.2) (Taylor et al., 2019) on the classification diagram (Stöffler et al., 1980) in Figure 4.10. The mineralogical classification results suggests the core soils are dominated by anorthositic norite and noritic anorthosite, which is consistent with the compositional classes of Station 3 trench soils. Sun et al. (2018) summarized the compositional classes for 43 Apollo 17 soils, and their results suggest the major compositional class for South Massif and most of the landslide soils is anorthositic norite, which supports our mineral mode results from the core. The average Mg# of the seventeen spectra is 61, which is consistent with that of the Station 3 trench soils (Mg# = 67).

4.4 Conclusions

We report the preliminary results of the spectral imaging and hyperspectral profile measured during the first dissection of core 73002. Both multiband imaging and hyperspectral data show systematic spectral darkening and reddening due to space weathering, suggesting an increasing maturity degree from bottom to top of the core. We derived the OMAT profile along the core from the band ratio plot, and OMAT increases from surface to bottom, corresponding to decreasing maturity from surface to bottom. We also calculated the FeO and TiO_2 distributions within the core using multiband images. FeO and TiO_2 content are homogeneous from bottom to top of the core, and they are concentrated near 9 wt.% and 2 wt.%, respectively.

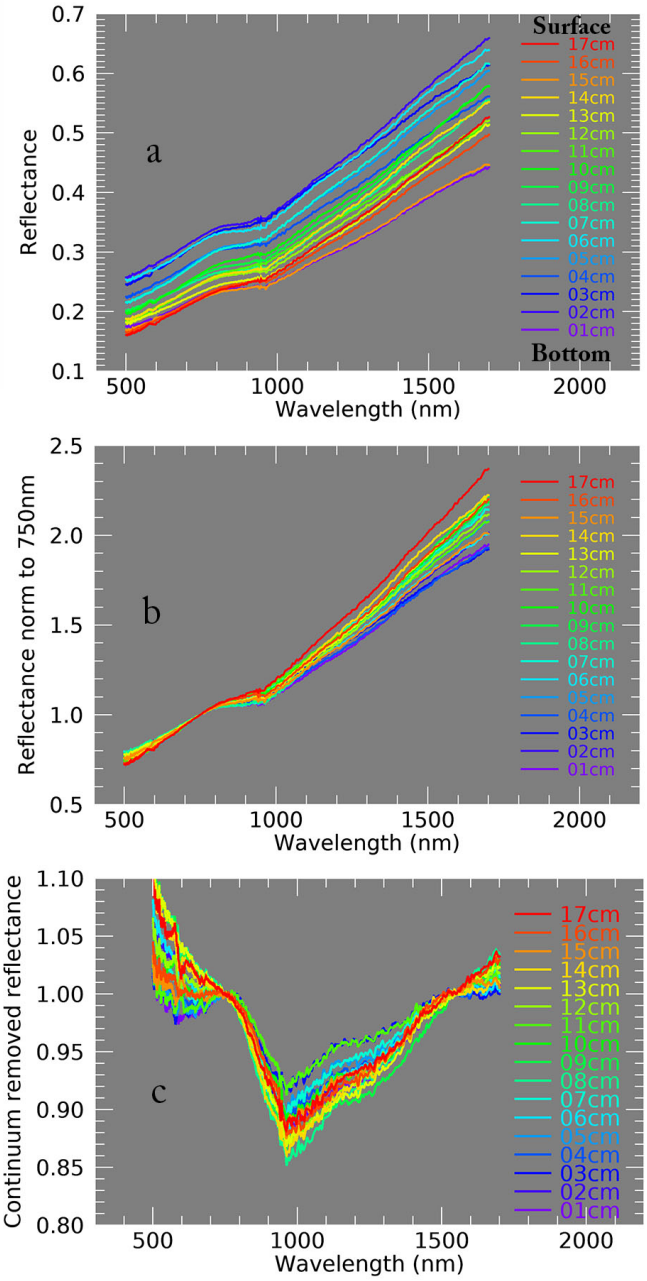

Figure 4.9: (a) Reflectance spectra along the core. Locations indicate the values on the scale in Figure 4.5a, and the reflectance shows a systematic darkening from bottom to top of the core. (b) Reflectance normalized to 750 nm. An increasing reddening trend can be observed from bottom to top of the core. (c) Continuum removed reflectance. Depths at one micron do not vary substantially with location.

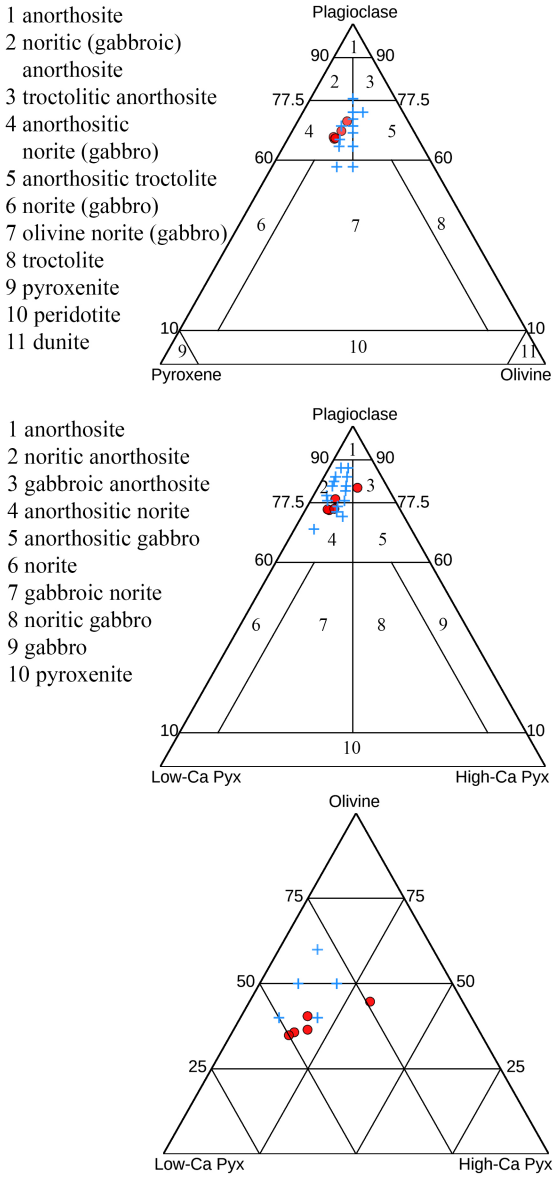

Figure 4.10: Mineral modes of the core derived from the Sun et al. (2018) model (blue crosses) and those of Station 3 soils measured by XRD (Taylor et al., 2019) (red dots) plotted on the classification diagram (Stöffler et al., 1980).

The vertical regolith reworking depth inferred from OMAT profile is about 14 cm, indicating a time range of 61 million years based on the equation of Morris (1978a). OMAT of surface soils increased 60% during 61 million years, and their corresponding maturity changed from immature to submature.

The major compositional classes of the core are anorthositic norite and noritic anorthosite based on radiative transfer modeling, and the average Mg# is around 61, consistent with those of Station 3 soils measured in lab.

This spectral dataset of the core can provide ground truth in both composition/mineral unmixing and space weathering for remote sensing studies.

4.5 Future Work

Preliminary multiband images did not cover the whole core width due to the limitation of light source. We are constructing a custom illuminator that provides illumination over the full width of the core for layer by layer imaging. During the operational measurements, the whole core will be illuminated and captured by the camera. Hyperspectral profiles will be obtained at 1 mm spatial resolution and 5 mm sampling distance during the operational spectral measurement to provide hyperspectral data throughout the whole core volume.

The use of the 15° incident angle and 25° in plane phase angle in the preliminary data resulted in substantial shadowing at the 100 μm scale. Thus the preliminary data spectral imaging data set are confined to spectral ratios lacking pixel level photometric correction. To mitigate this, the operational data will be obtained with a zero degree incidence angle to minimize shadowing, and a viewing angle of 15°. We are also constructing a new illuminator specifically for the hyperspectral data that will allow us to observe at zero phase angle and eliminate any issues with topographic shading.

Currently all the spectrometers observe through the safety glass on top of the glove cabinet at the curatorial facility at NASA Johnson Space Center, which limits the detection range of spectroscopy to visible and near infrared wavelengths. However, when the core dissection reaches the bottom layer, the core will be moved outside of the pristine sample handling cabinet, making it available for inspection at longer wavelengths. We plan to collect hyperspectral data from 0.5 to 14 μm at 10 mm spatial resolution for this final layer of the cores.

Chapter 5

Conclusions

In conclusion, we analyzed the mineralogy and composition of lunar soil and core samples. Using these sample data as ground truth, we mapped the distribution of major compositional class and Mg# on the Moon.

In the second chapter, we used the quantitative XRD analysis of lunar soils as ground truth, and tested the mineral contents derived by radiative transfer model from Multiband Imager images, then analyzed the compositional class for Apollo 15, 16 and 17 landing stations. To determine how representative the Apollo samples are, we searched areas having similar compositional class on both regional and global scales. To further expand the regional study of the sampling sites, we also mapped the compositional class for global lunar nonmare immature surfaces. We found that the Farside Highlands Terrane (FHT) mainly consists of noritic anorthosite, anorthosite and anorthositic norite, while South Pole-Aitken basin mainly consists of anorthositic norite, norite and olivine norite. The enrichment of noritic compositions indicate the presence of abundant low-Ca pyroxene in lunar highlands. We also find that olivine is not abundant in the highlands. Noritic highland and SPA from our study suggest a LCP dominated upper mantle, while the olivine rich basin rings in the nearside trapped an olivine rich mantle. To better explain this quandary, we proposed a "two mantle" hypothesis, which suggests the highlands and SPA exposed a pre-overturn upper mantle that is dominated by LCP, while the basin rings trapped a post-overturn upper mantle that is dominated by olivine. This hypothesis is consistent with current Mg#

studies and the lunar solidification model, and it can be tested by higher spatial resolution Mg# mapping results in the future.

To determine the Mg# distribution on the Moon, we developed a new radiative transfer model in the third chapter. We applied radiative transfer equations that include porosity and opposition effect in replicating the optical behaviors of lunar major minerals. With these equations, we provide a new set of optical constants for olivine, orthopyroxene and clinopyroxene. The forward modeling has shown that these optical constants can reproduce reflectance spectra for both powdered pure minerals and lunar soils characterization consortium (LSCC) lunar soils, and the spectral characteristics are consistent with those measured in the laboratory. For the inverse modeling, we build a spectral mixing library and developed a spectral matching algorithm. We applied a sensitivity test by adding noises comparable to that of Kaguya Multiband Imager data. The the accuracy in estimating mineral abundances is less than 3 vol% for olivine, low-Ca pyroxene and high-Ca pyroxene, and less than 6 vol% for plagioclase; the accuracy in estimating Mg# is less than 10. Mineral abundances derived from our model are linearly correlated with those measured from LSCC lunar soils in the laboratory. A global Mg# map is presented, and the peak and mean Mg# values are 70 and 65. Mg# is 59.4 for typical lunar highlands and 50.8 for lunar nearside mare. Our Mg# map is consistent with that derived from the Lunar Prospector gamma-ray spectrometer.

In the fourth chapter, we report the preliminary results of the spectral imaging and hyperspectral profile measured during the first dissection of core 73002. Both multiband imaging and hyperspectral data show systematic spectral darkening and reddening due to space weathering, suggesting an increasing maturity degree from bottom to top of the core. We derived the OMAT profile along the core from the band ratio plot, and OMAT increases from surface to bottom, corresponding to decreasing maturity from surface to bottom. We also calculated the FeO and TiO_2 distributions within the core using multiband images. FeO and TiO_2 content are homogeneous from bottom to top of the core, and they are concentrated near 9 wt.% and 2 wt.%, respectively. The vertical regolith reworking depth

inferred from OMAT profile is about 14 cm, indicating a time range of 61 million years based on the equation of Morris (1978a). This time scale is consistent with the space exposure time of samples collected at Station 3, suggesting little significant lateral contamination has affected the local regolith. OMAT of surface soils increased 60% during 61 million years, and their corresponding maturity changed from immature to submature. The major compositional classes of the core are anorthositic norite and noritic anorthosite based on the radiative transfer model introduced in chapter 3, and the average Mg# is around 61, consistent with those of Station 3 soils measured in laboratory. This spectral dataset of the core can provide ground truth in both composition/mineral unmixing and space weathering for remote sensing studies.

Appendix A

Supporting Information for "Compositional class mapping of Apollo landing sites and the global Moon"

A.1 Introduction

This supporting information introduces the mapping method of mineral classification and provides the mineral content range that we used to generate the mineralogy classification maps.

A.2 Mapping compositional classes

In order to map areas that have similar mineralogy to the feldspathic landing sites, we listed their maximum and minimum mineral abundances in Table A.1. For each pixel on the Multiband Imager (MI) mineral map (Lemelin et al., 2015), if its plagioclase, olivine, low-Ca pyroxene (LCP) and high-Ca pyroxene (HCP) abundances fall within the range (e.g., ¡maximum and $\geq$ minimum) of a landing site listed in Table A.1, we consider this pixel has similar mineralogy to this landing site.

We used the decision tree in Figure A.1 to determine the mineralogical classification of each pixel on the MI mineral map.

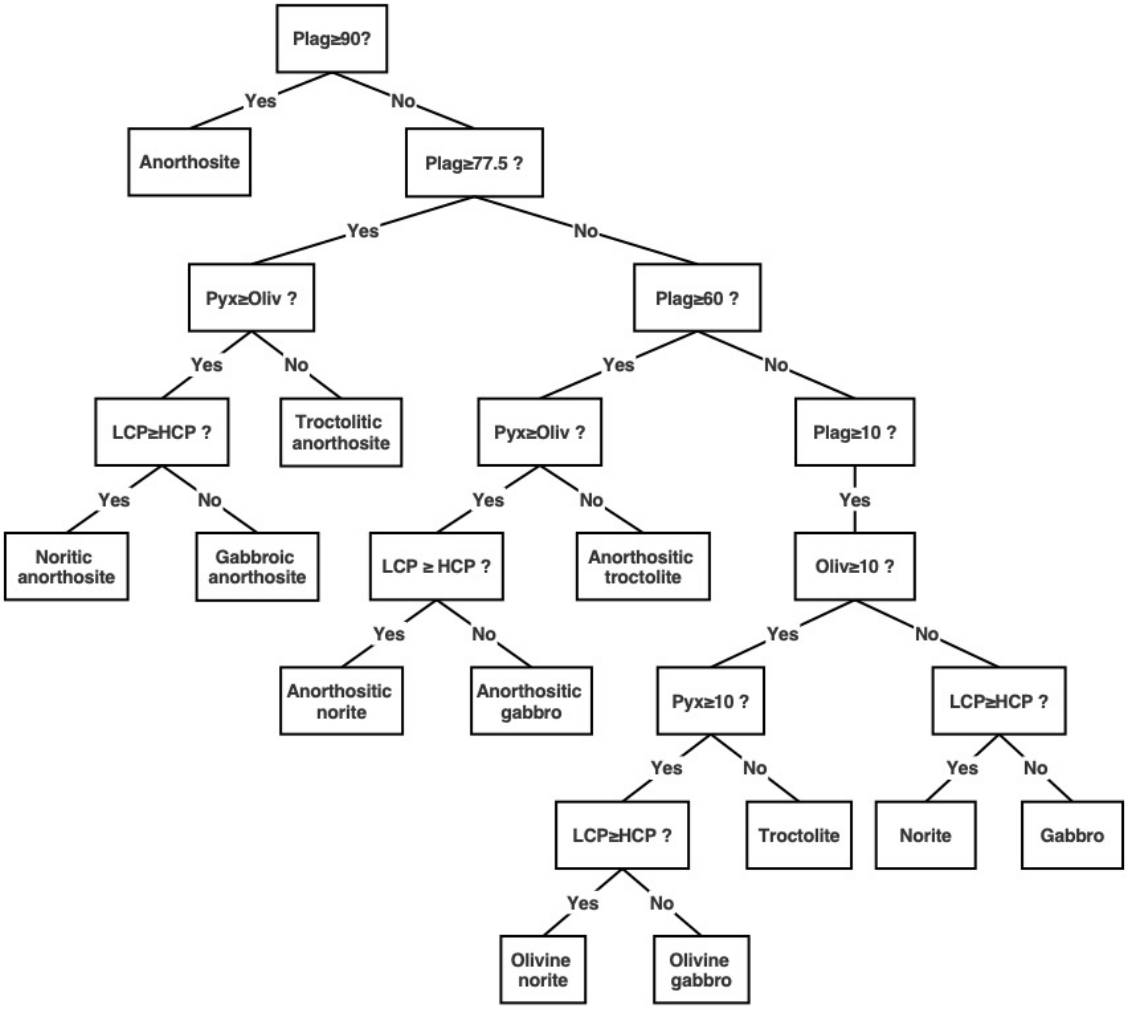

Figure A.1: A decision tree used to determine the mineralogical class using mineral abundances (in vol%) based on the ternary diagram of Stoffler et al. (1980). In this work, we only classify areas having 10-90 vol% plagioclase. The abundance of pyroxene (Pyx) is the total of low-Ca pyroxene and high-Ca pyroxene..

Table A.1: The maximum and minimum value of the abundances of plagioclase, olivine, HCP and LCP for the feldspathic landing sites.

Landing site	Maximum				Minimum			
	Plag	Oliv	HCP	LCP	Plag	Oliv	HCP	LCP
A15-Apennine Front	64.7	10.3	16.0	18.5	61.3	7.8	10.3	11.6
A16-North Ray	94.6	2.0	5.9	4.7	89.0	0.5	0.6	2.9
A16-South Ray	83.4	5.9	3.5	14.1	82.0	3.3	0.6	7.2
A16-Cayley Plains	85.7	4.1	8.7	7.3	83.4	1.3	5.8	4.4
A16-Descartes Mountains	83.9	4.1	7.6	11.2	83.8	2.9	0.9	5.7
A17-South Massif	75.2	3.0	7.7	14.1	75.2	3.0	7.7	14.1
A17-North Massif	63.8	13.4	2.3	27.8	59.6	10.4	0.0	24.7
A17-Sculptured Hills	53.1	14.9	23.4	15.1	51.4	9.3	18.6	14.2

Appendix B

Supporting Information for "Unmixing mineral content and chemistry with radiative transfer modeling: Theory and applications"

B.1 Introduction

This supporting information file contains information about how to calculate the FeO abundances for the spectral mixing library using a stoichiometric method, and an example of estimating the noise level for spectral reflectance data from Kaguya Multiband Imager (MI).

B.2 Estimating FeO abundances with a stoichiometric method

We use FeO as a constraint in spectral matching to the mixing library, and the FeO content for library mineral mixtures can be estimated with a stoichiometric method. FeO content of olivine and pyroxenes can be calculated with their Mg# and atom masses using equations B.1 and B.2. The total FeO content of a mineral mixture can be estimated using the volume average FeO content of each mineral (equation B.3).

$$FeO_{oli} = 100 \cdot 2 \cdot (Fe + O) \cdot (Fa/100) / [\, 2 \cdot Fe \cdot Fa/100 + 2 \cdot Mg \cdot Fo/100 + Si + 4 \cdot O] \quad \text{(B.1)}$$

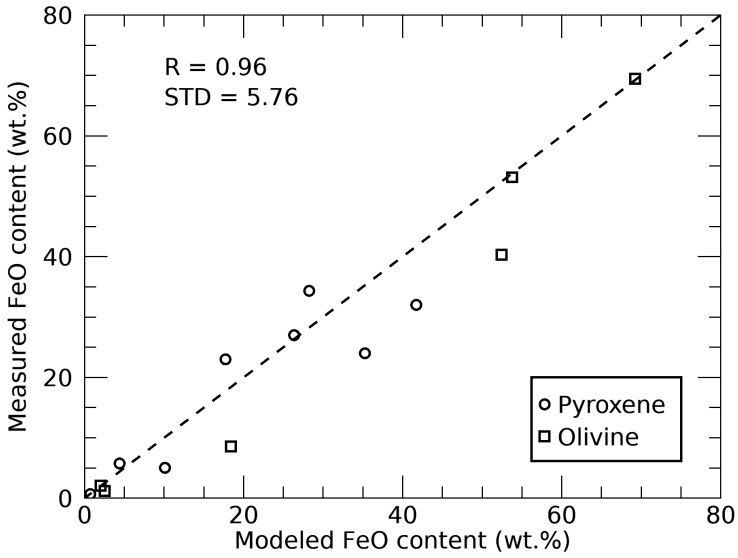

Figure B.1: Measured FeO content compared with those calculated stoichiometrically for olivine and pyroxenes. Dashed line is 1:1 line.

$$FeO_{pyx} = 100 \cdot (Fe+O) \cdot (Fs/100) / [\, Fe \cdot Fs/100 + Mg \cdot En/100 + Ca \cdot Wo/100 + Si + 3 \cdot O] \tag{B.2}$$

$$FeO_{mix} = \sum_i V_i FeO_i / \sum_i V_i \tag{B.3}$$

Deer et al. (2013) listed the FeO content and chemistry of naturally occurring olivine and pyroxenes in their Tables 1 and 17, which allows us to calculate the FeO content with equations B.1 and B.2. Figure B.1 shows that the modeled FeO content is consistent with the measured ones, and the scatter may due to the existence of minor and trace elements.

A.3 Estimating noise for Kaguya Multiband Imager data

We selected a relatively smooth area (center coordinates: 32N, 17E, Figure B.2) located in the northern Serenitatis basin to apply a simple estimation of the noise level of Kaguya Mutliband Imager data. Since the visible and near IR spectra are acquired from two

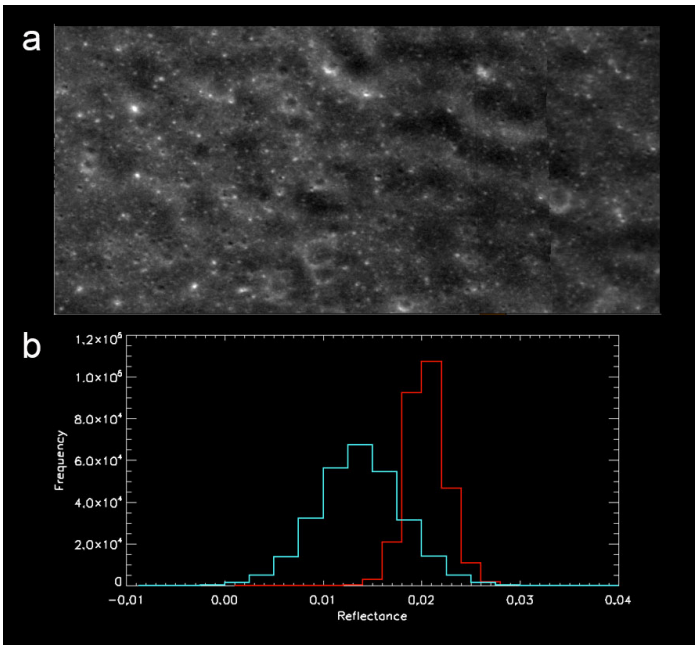

Figure B.2: (a) The area used in estimating noise for Kaguya MI data. (2) Histograms of difference between 0.95 μm and 1.0 μm in visible bands (blue), 1.0 μm and 1.05 μm in near infrared wavelength (red).

spectrometers, their noise are estimated separately. To limit the deviation caused by maturity and composition in this area, we use the difference of two neighboring bands to estimate the noise. We used the difference of 0.95 μm and 1.0 μm for visible bands and the difference of 1.0 μm and 1.05 μm for near IR bands. The histograms of the difference values for visible and near IR bands are shown in Figure B.2. The standard deviation of the difference between two bands can be used as noise, and the noise estimation are 0.0031 for visible bands and 0.0014 for near IR bands.

References

Apollo Lunar Geology Investigation Team (1972). Geologic setting of the apollo 15 samples. *Science*, 175(4020):407–415.

Arvidson, R., Drozd, R., Guinness, E., Hohenberg, C., Morgan, C., Morrison, R., and Oberbeck, V. (1976). Cosmic ray exposure ages of apollo 17 samples and the age of tycho. In *Lunar and Planetary Science Conference Proceedings*, volume 7, pages 2817–2832.

Blewett, D. T., Hawke, B. R., Lucey, P. G., Taylor, G. J., Jaumann, R., and Spudis, P. D. (1995). Remote sensing and geologic studies of the schiller-schickard region of the moon. *Journal of Geophysical Research: Planets*, 100(E8):16959–16977.

Blewett, D. T., Lucey, P. G., Hawke, B. R., and Jolliff, B. L. (1997). Clementine images of the lunar sample-return stations: Refinement of feo and tio2 mapping techniques. *Journal of Geophysical Research: Planets*, 102(E7):16319–16325.

Burns, R. G. (1970). Crystal field spectra and evidence of cation ordering in olivine minerals. *American Mineralogist: Journal of Earth and Planetary Materials*, 55(9-10):1608–1632.

Burns, R. G. and Burns, R. G. (1993). *Mineralogical applications of crystal field theory*, volume 5. Cambridge university press.

Butler, P. (1973). *Lunar Sample Information Catalog, Apollo 17*. Houston, TX.

Cahill, J., Lucey, P., Stockstill-Cahill, K., and Hawke, B. (2010). Radiative transfer modeling of near-infrared reflectance of lunar highland and mare soils. *Journal of Geophysical Research: Planets*, 115(E12).

Cahill, J., Lucey, P., and Wieczorek, M. (2009). Compositional variations of the lunar crust: Results from radiative transfer modeling of central peak spectra. *Journal of Geophysical Research: Planets*, 114(E9).

Cameron, A. and Canup, R. (1998). The giant impact and the formation of the moon. In *Origin of the Earth and Moon*, volume 957, page 3.

Clénet, H., Pinet, P., Daydou, Y., Heuripeau, F., Rosemberg, C., Baratoux, D., and Chevrel, S. (2011). A new systematic approach using the modified gaussian model: Insight for the characterization of chemical composition of olivines, pyroxenes and olivine–pyroxene mixtures. *Icarus*, 213(1):404–422.

Cloutis, E. (2020). Centre for terrestrial and planetary exploration.

Corley, L. M., McGovern, P. J., Kramer, G. Y., Lemelin, M., Trang, D., Gillis-Davis, J. J., Taylor, G. J., Powell, K. E., Kiefer, W. S., Wieczorek, M., et al. (2018). Olivine-bearing lithologies on the moon: Constraints on origins and transport mechanisms from m3 spectroscopy, radiative transfer modeling, and grail crustal thickness. *Icarus*, 300:287–304.

Crites, S. T. and Lucey, P. G. (2015). Revised mineral and mg# maps of the moon from integrating results from the lunar prospector neutron and gamma-ray spectrometers with clementine spectroscopy. *American Mineralogist*, 100(4):973–982.

Deer, W. A., F., Howie, R. A., and Zussman, J. (2013). *An Introduction to the Rock-Forming Minerals*. Mineralogical Society of Great Britain and Ireland.

Denevi, B., Lucey, P., Hochberg, E., and Steutel, D. (2007). Near-infrared optical constants of pyroxene as a function of iron and calcium content. *Journal of Geophysical Research: Planets*, 112(E5).

Duke, M. B. and Nagle, J. (1976). *Lunar core catalog*. Lyndon B. Johnson Space Center.

Elkins-Tanton, L. T., Burgess, S., and Yin, Q.-Z. (2011). The lunar magma ocean: Reconciling the solidification process with lunar petrology and geochronology. *Earth and Planetary Science Letters*, 304(3-4):326–336.

Hapke, B. (1981). Bidirectional reflectance spectroscopy: 1. theory. *Journal of Geophysical Research: Solid Earth*, 86(B4):3039–3054.

Hapke, B. (1986). Bidirectional reflectance spectroscopy: 4. the extinction coefficient and the opposition effect. *Icarus*, 67(2):264–280.

Hapke, B. (2001). Space weathering from mercury to the asteroid belt. *Journal of Geophysical Research: Planets*, 106(E5):10039–10073.

Hapke, B. (2002). Bidirectional reflectance spectroscopy: 5. the coherent backscatter opposition effect and anisotropic scattering. *Icarus*, 157(2):523–534.

Hapke, B. (2008). Bidirectional reflectance spectroscopy: 6. effects of porosity. *Icarus*, 195(2):918–926.

Hapke, B. (2012). *Theory of reflectance and emittance spectroscopy*. Cambridge university press.

Heiken, G. H., Vaniman, D. T., and French, B. M. (1991). *Lunar Sourcebook: A user's guide to the Moon*. Cambridge Univ. Press, New York.

Hodges, C., Muehlberger, W. R., and Ulrich, G. E. (1973). Geologic setting of apollo 16. In *Lunar and Planetary Science Conference Proceedings*, volume 4, page 1.

Hu, X., Ma, P., Yang, Y., Zhu, M.-H., Jiang, T., Lucey, P. G., Sun, L., Zhang, H., Li, C., Xu, R., et al. (2019). Mineral abundances inferred from in-situ reflectance measurements of chang'e-4 landing site in south pole-aitken basin. *Geophysical Research Letters*.

Isaacson, P. J., Klima, R. L., Sunshine, J. M., Cheek, L. C., Pieters, C. M., Hiroi, T., Dyar, M. D., Lane, M., and Bishop, J. (2014). Visible to near-infrared optical properties of pure synthetic olivine across the olivine solid solution. *American Mineralogist*, 99(2-3):467–478.

Jolliff, B. L., Gillis, J. J., Haskin, L. A., Korotev, R. L., and Wieczorek, M. A. (2000). Major lunar crustal terranes: Surface expressions and crust-mantle origins. *Journal of Geophysical Research: Planets*, 105(E2):4197–4216.

Jolliff, B. L., Rockow, K. M., Korotev, R. L., and Haskin, L. A. (1996). Lithologic distribution and geologic history of the apollo 17 site: The record in soils and small rock particles from the highland massifs. *Meteoritics & Planetary Science*, 31(1):116–145.

King, T. V. and Ridley, W. I. (1987). Relation of the spectroscopic reflectance of olivine to mineral chemistry and some remote sensing implications. *Journal of Geophysical Research: Solid Earth*, 92(B11):11457–11469.

Klima, R. L., Dyar, M. D., and Pieters, C. M. (2011). Near-infrared spectra of clinopyroxenes: Effects of calcium content and crystal structure. *Meteoritics & Planetary Science*, 46(3):379–395.

Klima, R. L., Pieters, C. M., and Dyar, M. D. (2007). Spectroscopy of synthetic mg-fe pyroxenes i: Spin-allowed and spin-forbidden crystal field bands in the visible and near-infrared. *Meteoritics & Planetary Science*, 42(2):235–253.

Korotev, R. L. and Kremser, D. T. (1992). Compositional variations in apollo 17 soils and their relationship to the geology of the taurus-littrow site. In *Lunar and Planetary Science Conference Proceedings*, volume 22, pages 275–301.

Lawrence, D., Feldman, W., Barraclough, B., Binder, A., Elphic, R., Maurice, S., and Thomsen, D. (1998). Global elemental maps of the moon: The lunar prospector gamma-ray spectrometer. *Science*, 281(5382):1484–1489.

Lawrence, S. and Lucey, P. (2007). Radiative transfer mixing models of meteoritic assemblages. *Journal of Geophysical Research: Planets*, 112(E7).

Lemelin, M., Lucey, P. G., Miljković, K., Gaddis, L. R., Hare, T., and Ohtake, M. (2019). The compositions of the lunar crust and upper mantle: Spectral analysis of the inner rings of lunar impact basins. *Planetary and Space Science*, 165:230–243.

Lemelin, M., Lucey, P. G., Song, E., and Taylor, G. J. (2015). Lunar central peak mineralogy and iron content using the kaguya multiband imager: Reassessment of the compositional structure of the lunar crust. *Journal of Geophysical Research: Planets*, 120(5):869–887.

Li, C., Liu, D., Liu, B., Ren, X., Liu, J., He, Z., Zuo, W., Zeng, X., Xu, R., Tan, X., et al. (2019). Chang'e-4 initial spectroscopic identification of lunar far-side mantle-derived materials. *Nature*, 569(7756):378.

Li, S. and Milliken, R. E. (2016). An empirical thermal correction model for moon mineralogy mapper data constrained by laboratory spectra and diviner temperatures. *Journal of Geophysical Research: Planets*, 121(10):2081–2107.

Li, S. and Milliken, R. E. (2017). Water on the surface of the moon as seen by the moon mineralogy mapper: Distribution, abundance, and origins. *Science advances*, 3(9):e1701471.

Ling, Z., Jolliff, B. L., Wang, A., Li, C., Liu, J., Zhang, J., Li, B., Sun, L., Chen, J., Xiao, L., et al. (2015). Correlated compositional and mineralogical investigations at the chang'e-3 landing site. *Nature communications*, 6:8880.

Lucchitta, B. K. (1977). Crater clusters and light mantle at the apollo 17 site; a result of secondary impact from tycho. *Icarus*, 30(1):80–96.

Lucey, P. G. (1998). Model near-infrared optical constants of olivine and pyroxene as a function of iron content. *Journal of Geophysical Research: Planets*, 103(E1):1703–1713.

Lucey, P. G. (2004). Mineral maps of the moon. *Geophysical Research Letters*, 31(8).

Lucey, P. G. (2006). Radiative transfer modeling of the effect of mineralogy on some empirical methods for estimating iron concentration from multispectral imaging of the moon. *Journal of Geophysical Research: Planets*, 111(E8).

Lucey, P. G., Blewett, D. T., and Jolliff, B. L. (2000a). Lunar iron and titanium abundance algorithms based on final processing of clementine ultraviolet-visible images. *Journal of Geophysical Research: Planets*, 105(E8):20297–20305.

Lucey, P. G., Blewett, D. T., Taylor, G. J., and Hawke, B. R. (2000b). Imaging of lunar surface maturity. *Journal of Geophysical Research: Planets*, 105(E8):20377–20386.

Lucey, P. G., Norman, J. A., Crites, S. T., Taylor, G. J., Hawke, B. R., Lemelin, M., and Melosh, H. J. (2014). A large spectral survey of small lunar craters: Implications for the composition of the lunar mantle. *American Mineralogist*, 99(11-12):2251–2257.

Lucey, P. G., Taylor, G. J., and Malaret, E. (1995). Abundance and distribution of iron on the moon. *Science*, 268(5214):1150–1153.

Melosh, H., Kendall, J., Horgan, B., Johnson, B., Bowling, T., Lucey, P., and Taylor, G. (2017). South pole–aitken basin ejecta reveal the moon's upper mantle. *Geology*, 45(12):1063–1066.

Meyer, H., Denevi, B., Robinson, M., and Boyd, A. (2020). The global distribution of lunar light plains from the lunar reconnaissance orbiter camera. *Journal of Geophysical Research: Planets*, 125(1):e2019JE006073.

Meyer, H., Robinson, M., Denevi, B., and Boyd, A. (2018). A new global map of light plains from the lunar reconnaissance orbiter camera. In *Lunar and Planetary Science Conference*, volume 49.

Miljković, K., Wieczorek, M. A., Collins, G. S., Solomon, S. C., Smith, D. E., and Zuber, M. T. (2015). Excavation of the lunar mantle by basin-forming impact events on the moon. *Earth and Planetary Science Letters*, 409:243–251.

Moriarty, D. and Pieters, C. (2016). Complexities in pyroxene compositions derived from absorption band centers: Examples from apollo samples, hed meteorites, synthetic pure pyroxenes, and remote sensing data. *Meteoritics & Planetary Science*, 51(2):207–234.

Morris, R. (1978a). In situ reworking/gardening/of the lunar surface-evidence from the apollo cores. In *Lunar and Planetary Science Conference Proceedings*, volume 9, pages 1801–1811.

Morris, R. (1978b). The surface exposure/maturity/of lunar soils-some concepts and is/feo compilation. In *Lunar and Planetary Science Conference Proceedings*, volume 9, pages 2287–2297.

Mustard, J. F. and Pieters, C. M. (1989). Photometric phase functions of common geologic minerals and applications to quantitative analysis of mineral mixture reflectance spectra. *Journal of Geophysical Research: Solid Earth*, 94(B10):13619–13634.

Noble, S. K., Pieters, C. M., Hiroi, T., and Taylor, L. A. (2006). Using the modified gaussian model to extract quantitative data from lunar soils. *Journal of Geophysical Research: Planets*, 111(E11).

Nyquist, L., Shih, C.-Y., Reese, Y., Park, J., Bogard, D., Garrison, D., and Yamaguchi, A. (2010). Lunar crustal history recorded in lunar anorthosites. In *Lunar and Planetary Science Conference*, volume 41, page 1383.

Ohtake, M., Pieters, C. M., Isaacson, P., Besse, S., Yokota, Y., Matsunaga, T., Boardman, J., Yamomoto, S., Haruyama, J., Staid, M., Mall, U., and Green, R. O. (2013). One moon, many measurements 3: Spectral reflectance. *Icarus*, 226(1):364–374.

Ohtake, M., Takeda, H., Matsunaga, T., Yokota, Y., Haruyama, J., Morota, T., Yamamoto, S., Ogawa, Y., Hiroi, T., Karouji, Y., et al. (2012). Asymmetric crustal growth on the moon indicated by primitive farside highland materials. *Nature Geoscience*, 5(6):384.

Papike, J. J., Ryder, G., and Shearer, C. K. (1998). Lunar samples. *Reviews in Mineralogy and Geochemistry*, 36(1):5.1–5.234.

Petro, N. and Pieters, C. (2006). Modeling the provenance of the apollo 16 regolith. *Journal of Geophysical Research: Planets*, 111(E9).

Phinney, D., Kahl, S., and Reynolds, J. (1975). ^{40}Ar–^{39}Ar dating of apollo 16 and 17 rocks. In *Lunar and Planetary Science Conference Proceedings*, volume 6, pages 1593–1608.

Pieters, C., Head, J., Gaddis, L., Jolliff, B., and Duke, M. (2001). Rock types of south pole-aitken basin and extent of basaltic volcanism. *Journal of Geophysical Research: Planets*, 106(E11):28001–28022.

Pieters, C. M., Fischer, E. M., Rode, O., and Basu, A. (1993). Optical effects of space weathering: The role of the finest fraction. *Journal of Geophysical Research: Planets*, 98(E11):20817–20824.

Prettyman, T., Hagerty, J., Elphic, R., Feldman, W., Lawrence, D., McKinney, G., and Vaniman, D. (2006). Elemental composition of the lunar surface: Analysis of gamma ray spectroscopy data from lunar prospector. *Journal of Geophysical Research: Planets*, 111(E12).

Robinson, M. S. and Jolliff, B. L. (2002). Apollo 17 landing site: Topography, photometric corrections, and heterogeneity of the surrounding highland massifs. *Journal of Geophysical Research: Planets*, 107(E11):20–1.

Rose, H. J., Cuttitta, F., Berman, S., Brown, F., Carron, M., Christian, R., Dwornik, E., and Greenland, L. (1974). Chemical composition of rocks and soils at taurus-littrow. In *Lunar and Planetary Science Conference Proceedings*, volume 5, pages 1119–1133.

Ryder, G. (1993). Catalog of apollo 17 rocks. volume 1: Stations 2 and 3 (south massif).

Ryder, G. and Bower, J. F. (1977). Petrology of apollo 15 black-and-white rocks 15445 and 15455-fragments of the imbrium impact melt sheet. In *Lunar and Planetary Science Conference Proceedings*, volume 8, pages 1895–1923.

Ryder, G. and Norman, M. D. (1980). Catalog of apollo 16 rocks: Part i. *NASA JSC# 16904 Publication 52, 349pp.*

Ryder, G. and Norman, M. D. (1985). *Catalog of Apollo 15 rocks*. Citeseer.

Ryder, G. and Wood, J. A. (1977). Serenitatis and imbrium impact melts - implications for large-scale layering in the lunar crust. In *8th Lunar Science Conference*, pages 655–668.

Schmitt, H. H., Petro, N. E., Wells, R. A., Robinson, M. S., Weiss, B. P., and Mercer, C. M. (2017). Revisiting the field geology of taurus–littrow. *Icarus*, 298(Supplement C):2–33.

Snyder, G., Taylor, L., and Neal, C. (1991). The sources of mare basalts: A model involving lunar magma ocean crystallization, plagioclase flotation, and trapped instantaneous residual liquid. In *Mare Volcanism and Basalt Petrogenesis: Astoundi ng Fundamental Concepts*, page 53.

Spudis, P. D. and Pieters, C. (1991). *Global and regional data about the Moon*, pages 595–632. Cambridge Univ. Press, New York.

Spudis, P. D. and Ryder, G. (1985). Geology and petrology of the apollo 15 landing site: Past, present, and future understanding. *Eos, Transactions American Geophysical Union*, 66(43):721–726.

Spudis, P. D., Wilhelms, D. E., and Robinson, M. S. (2011). The sculptured hills of the taurus highlands: Implications for the relative age of serenitatis, basin chronologies and the cratering history of the moon. *Journal of Geophysical Research: Planets*, 116(E12):E00H03.

Steele, I. M. and Smith, J. V. (1971). Mineralogy of apollo 15415 "genesis rock": Source of anorthosite on moon. *Nature*, 234(5325):138.

Stöffler, D., Knöll, H., Marvin, U., Simonds, C., and Warren, P. (1980). Recommended classification and nomenclature of lunar highland rocks-a committee report. In *Lunar Highlands Crust*, pages 51–70.

Sun, L., Lucey, P. G., Ling, Z., Zhang, J., and Chen, J. (2019). Deriving abundances and chemistries of minerals with radiative transfer modeling. In *50th Lunar and Planetary Science Conference*, page 2905, Houston. Lunar and Planetary Institute.

Sun, L., Taylor, G. J., Martel, L. M. V., and Lucey, P. G. (2018). A comprehensive study of mineralogy at apollo 17 landing site. In *49th Lunar and Planetary Science Conference*, page 1693, Houston. Lunar and Planetary Institute.

Sunshine, J. M. and Pieters, C. M. (1998). Determining the composition of olivine from reflectance spectroscopy. *Journal of Geophysical Research: Planets*, 103(E6):13675–13688.

Sunshine, J. M., Pieters, C. M., and Pratt, S. F. (1990). Deconvolution of mineral absorption bands: An improved approach. *Journal of Geophysical Research: Solid Earth*, 95(B5):6955–6966.

Taylor, G. J., Martel, L. M., Lucey, P. G., Gillis-Davis, J. J., Blake, D. F., and Sarrazin, P. (2019). Modal analyses of lunar soils by quantitative x-ray diffraction analysis. *Geochimica et Cosmochimica Acta*, 266:17–28.

Taylor, G. J., MARTEL, L. M., and Spudis, P. D. (2012). The hadley-apennine kreep basalt igneous province. *Meteoritics & Planetary Science*, 47(5):861–879.

Taylor, L., Cahill, J., Patchen, A., Pieters, C., Morris, R., Keller, L., and McKay, D. (2001). Mineralogical and chemical characterization of lunar highland regolith: Lessons learned from mare soils. In *Lunar and Planetary Science Conference*, volume 32.

Taylor, L., Patchen, A., Taylor, D., Chambers, J., and McKay, D. (1996). X-ray digital imaging and petrography of lunar mare soils: Data input for remote sensing calibrations. *Icarus*, 124:500–512.

Trang, D., Lucey, P. G., Gillis-Davis, J. J., Cahill, J. T., Klima, R. L., and Isaacson, P. J. (2013). Near-infrared optical constants of naturally occurring olivine and synthetic pyroxene as a function of mineral composition. *Journal of Geophysical Research: Planets*, 118(4):708–732.

Vaughan, W. M., Head, J. W., Wilson, L., and Hess, P. C. (2013). Geology and petrology of enormous volumes of impact melt on the moon: A case study of the orientale basin impact melt sea. *Icarus*, 223(2):749–765.

Warren, P. H. (1985). The magma ocean concept and lunar evolution. *Annual Review of Earth and Planetary Sciences*, 13(1):201–240.

Whitten, J. L. and Head, J. W. (2015). Lunar cryptomaria: Physical characteristics, distribution, and implications for ancient volcanism. *Icarus*, 247:150–171.

Wieczorek, M. A., Jolliff, B. L., Khan, A., Pritchard, M. E., Weiss, B. P., Williams, J. G., Hood, L. L., Righter, K., Neal, C. R., Shearer, C. K., et al. (2006). The constitution and structure of the lunar interior. *Reviews in mineralogy and geochemistry*, 60(1):221–364.

Wilhelms, D. E., John, F., and Trask, N. J. (1987). The geologic history of the moon. Report 2330-7102, Washington.

Wilshire, H. G., Schaber, G. G., Silver, L. T., Phinney, W. C., and Jackson, E. D. (1972). Geologic setting and petrology of apollo 15 anorthosite (15415). *Geological Society of America Bulletin*, 83(4):1083–1092.

Wood, J. A., Dickey Jr, J. S., Marvin, U. B., and Powell, B. (1970). Lunar anorthosites and a geophysical model of the moon. *Geochimica et Cosmochimica Acta Supplement*, 1:965.

Yamamoto, S., Nakamura, R., Matsunaga, T., Ogawa, Y., Ishihara, Y., Morota, T., Hirata, N., Ohtake, M., Hiroi, T., Yokota, Y., et al. (2010). Possible mantle origin of olivine around lunar impact basins detected by selene. *Nature Geoscience*, 3(8):533.

Zeigler, R., Hanna, R., Edey, D., Eckley, S., Ketcham, R., Gross, J., and McCubbin, F. (2020). Using x-ray computed tomography to image apollo drive tube 73002. In *Lunar and Planetary Science Conference*, page 3023.